GRAPHITE-GRAPHENE SEMICONDUCTOR JUNCTIONS AND MAGNETO-DIELECTRIC COUPLING IN SCHOTTKY DIODES

By

SEFAATTIN TONGAY

A DISSERTATION PRESENTED TO THE GRADUATE SCHOOL
OF THE UNIVERSITY OF FLORIDA IN PARTIAL FULFILLMENT
OF THE REQUIREMENTS FOR THE DEGREE OF
DOCTOR OF PHILOSOPHY

UNIVERSITY OF FLORIDA

2010

© 2010 Sefaattin Tongay

To my family and Noone

ACKNOWLEDGMENTS

First of all, it is a pleasure to thank those who made this dissertation possible. I have used many laboratories, collaborated with a lot of groups and more than hundreds people passed their experience to me by giving their valuable time. I am almost sure that I will unintentionally forget couple names, I like to be upfront about it and apologize already.

Foremost, I like to express my gratitude to my advisor Prof. Dr. A. F. Hebard (Art) for everything he has done for me in and out of the department. He has not only been an amazing advisor but also a father figure, a friend, a collaborator. I feel incredibly lucky to touch his life and be part of it during my stay here in University of Florida. It is not practical to list all the things that I am thankful about here in this paragraph. And also it would be rather limited and unfair to concise. Instead, I like to thank him for accepting me as his doctorate student since it is when all this started happening at the first place.

I also like to thank my supervisor committee members Dr. D. Maslov, Dr. S. Pearton, Dr. A. Biswas and Dr. A. Rinzler for their time, mentoring and all their input in this work. It is also pleasure to thank to all of my collaborators, Dr. D. Maslov (Physics), Dr. B. Gila (Mat. Sci. Eng.), Dr. D. Tanner (Physics), Dr.E. Lambers (Mat. Sci. Eng.), Dr. V. Cracuin (Mat. Sci. Eng.), Dr. J. Jones (Mat. Sci. Eng.), Dr. C. Abernathy (Mat. Sci. Eng.), Dr. Xu Du (U. Rutgers), Dr. B. Appleton (Mat. Sci. Eng. and NIMET), Dr. Y. Hikita (Univ. of Tokyo), Dr. H. Hwang (Univ. of Tokyo), Dr. C. Martin (Chemistry), Dr. A. Rinzler (Physics), Dr. A. Biswas (Physics), Dr. H. P. Chang (Quan. Theo. Proj.), Dr. D. Norton (Mat. Sci. Eng.), Dr. C. Stanton (Physics), Dr. I. Kravchenko (OakRidge National lab.), Dr. E. Durgun (MIT), Dr. T. Yildirim (NIST), Dr. V. Basov (UCSD), Dr. N. Newman (Univ. Arizona), S. Trickley (Physics).

I am indebted to my many of my colleagues and doctorate friends to support me and work with me on various projects; Hridis Pal, R. Das, P. Mickel, S. Ghoshsi, G. B. Singh, L. Kemper, T. Dhakal, H. H. Jeen, S. Selcuk, R. Misra, M. Lemaitre but especially

to my students T. Schumann, X. Miao, K. Berke and A. Donius for being amazing students, collaborator and friends. I also like to thank to all former, present and future members of the Hebard's laboratory but especially to Dr. S. Selcuk. I like to thank to all physics faculty, graduate students, undergraduate students, all my friends from past to future, my office neighbor C. Stambaugh, Szolt Marcet for talking through our office wall and thinning it down last 4 years to hear each other clearly.

In experimental science most of the magic happens behind the closed doors and far beyond the fancy 'working' machines but in the technical details. I like to thank to entire machine shop staff (especially to Bill, Mark and John), cryogenics staff John and Greg, entire electronics shop staff, Jay Horton for his technical input in my experiments, Tim Noland for his technical help, all HPC computing center staff, IT specialist David, all clean room staff (B. Lewis, A. Ogden)

Lastly, I would like to thank to Noone for everything. I like to thank to my family; beloved daughter, Elise, my mom, dad, and all my siblings. I am thanksful to everyone who has touched my life anyhow, anytime and anywhere.

TABLE OF CONTENTS

page

ACKNOWLEDGMENTS 4

LIST OF TABLES 9

LIST OF FIGURES 10

ABSTRACT 13

CHAPTER

1 SEMICONDUCTOR THEORY AND SCHOTTKY BARRIER PHYSICS 15

1.1 Charge Carriers in Intrinsic and Extrinsic Semiconductors 15
1.2 Intrinsic and Extrinsic Semiconductors 17
1.3 The Schottky Barrier (Metal-Semiconductor) Contacts 18
1.3.1 Origin of the Schottky Barrier Formation at the M-S Interface . . . 19
1.3.2 Depletion Capacitance at the M-S Interface and C-V Relationship . 21
1.3.3 Transport Across the M-S Interface: Thermionic Emission 23
1.3.4 Non-Ideal Effects at the M-S Interfaces 25
1.3.4.1 Image force lowering or schottky effect 25
1.3.4.2 Thermionic field emission 26
1.3.4.3 Direct tunneling 27
1.3.5 Measurement of Schottky Barrier Height 27
1.3.5.1 Current-voltage characteristics 27
1.3.5.2 Capacitance-voltage characteristics 30
1.3.5.3 Internal photoemission technique 31
1.4 Ohmic Contacts to Semiconductors 32

2 MAGNETODIELECTRIC COUPLING IN NON-MAGNETIC AU / GAAS : SI SCHOTTKY DIODES 34

2.1 Introduction 34
2.2 Experimental Methods 35
2.2.1 Sample Preperation 35
2.2.2 Current-Voltage Measurements 36
2.2.3 Capacitance-Voltage Measurements 37
2.2.4 Internal Photoemission Technique 37
2.3 Experimental Results 38
2.3.1 Observation of Magnetocapacitance and Magnetic Field Dependence of $C-V$ Curves 38
2.3.2 Physical Processes in the Depletion Width 39
2.3.3 Effect of Magnetic Field on the Current-Voltage Characteristics . . 42
2.4 Modification of the Abrupt Junction Approximation (AJA) 43
2.5 Discussion 45

2.6 Summary . . . 47

3 MULTI-LAYER-GRAPHENE (MLG) BASED SCHOTTKY DIODES FORMED ON SI, GAAS, 4H-SIC AND GAN SUBSTRATES . . . 56

3.1 Introduction . . . 56
3.2 Experimental Details . . . 59
3.3 Formation of Schottky Diodes at the Multi-Layer-Graphene / Si Interface . . . 60
3.4 Formation of Schottky Diodes at the Multi-Layer-Graphene/GaAs Interface 63
3.5 Formation of Schottky Diodes at the Multi-Layer-Graphene/4H-SiC . . . 65
3.5.1 Schottky Barrier Characteristics of Multi-Layer-Graphene / 4H-SiC Schottky Diodes from 250 K up to 330 K . . . 66
3.5.2 Schottky Barrier Characteristics of Multi-Layer-Graphene / 4H-SiC Schottky Diodes from 300 K upto 1100 K . . . 67
3.6 Formation of Schottky Diodes at the Multi-Layer-Graphene/GaN Interfaces 71
3.7 Discussion . . . 73
3.7.1 Comparison of Φ^{I-V} to Φ^{C-V} and Determination of $\phi_{graphite}$ . . . 73
3.7.2 Bond Polarization Theory and Multi-Layer-Graphene to Graphene Limit . . . 75
3.8 Conclusion . . . 77

4 TUNING SCHOTTKY BARRIER HEIGHT AT THE MULTI-LAYER-GRAPHENE / SEMICONDUCTOR INTERFACE BY DOPING . . . 92

4.1 Introduction . . . 92
4.2 Experimental Procedure . . . 93
4.3 Results and Discussion . . . 95
4.3.1 Effect of Bromine Doping on the MLG / Semiconductor Schottky Barrier Diode $I-V$ Characteristics . . . 95
4.3.2 Effect of Bromine Doping at the MLG / Semiconductor Interface: Possible Mechanisms . . . 96
4.3.3 Characterization of Br Intercalated Graphite: XRD, AES and XPS Measurements . . . 97
4.3.4 Modification of the Band Structure at the Interface and $C-V$ Measurements . . . 101
4.3.5 Results on MLG / SiC Junctions and Sensing Applications . . . 103
4.4 Overview . . . 105

5 BAND STRUCTURE OF GRAPHITE . . . 115

5.1 Introduction . . . 115
5.1.1 Crystal Structure of Graphite and Graphene . . . 116
5.1.2 Band Structure:Energy Spectrum of Electrons / Holes in Graphite . 119

6 TRANSPORT PROPERTIES OF HIGHLY ORIENTED PYROLYTIC GRAPHITE (HOPG) FROM 3K UPTO 1500K . . . 126

6.1 Introduction . . . 126
6.2 In-Plane Transport (ρ_{ab}) from 1.7 K up to 900 K . . . 127
6.2.1 Experimental Details . . . 127
6.2.2 In-Plane Transport from 1.7 K up to 300 K: Drude Formula . . . 128
6.2.3 In-Plane Transport from 300 K up to 900 K . . . 130
6.3 Out of Plane Transport (ρ_c) Properties from 3K up to 1500K . . . 135
6.3.1 Breakdown in the Classical Model . . . 135
6.3.2 Proposed Mechanisms and Discussion . . . 136

7 SUPERMETALLIC CONDUCTIVITY IN BROMINE INTERCALATED GRAPHITE 150

7.1 Introduction . . . 150
7.2 Experimental . . . 152
7.2.1 Sample Preparation and Characterization . . . 152
7.2.2 Electrical Measurements . . . 154
7.2.3 Optical Measurements . . . 158
7.2.4 Magnetization Measurements . . . 160
7.2.5 Discussion . . . 160

8 GRAPHENE AND GRAPHITE GROWTH ON SIC BY THERMAL ANNEALING 172

8.1 Introduction . . . 172
8.2 Experimental Details . . . 173
8.3 Material Characterization . . . 173

REFERENCES . . . 180

BIOGRAPHICAL SKETCH . . . 188

LIST OF TABLES

Table page

3-1 Extracted SBHs, doping densities, and corresponding graphite work function values on various multi-layer-graphene/semiconductor junctions 77

5-1 Values and description of the parameters used in SWMc model 121

LIST OF FIGURES

Figure page

1-1 Energy diagram of metal/semiconductor junction diode 33

2-1 I-V characteristics from room temperature down to 20 K and 0 to 70 kOe. . . . 49

2-2 Magnetocapacitance effect from 300 K down to 20 K. 50

2-3 Extraction of built-in potential values. $1/C^2$ vs V_R plots at different magnetic field and temperatures. 51

2-4 Frequency dependence of V_{bi} and N_D at H=0 and 70 kOe. 52

2-5 Capacitance and loss versus frequency data at different T and H. 53

2-6 The dependence of activation energy, E_a, on the applied magnetic field H. . . . 54

2-7 Internal Photo-emission experiments on the Schottky diodes. 55

3-1 Room temperature current density J with respect to applied bias V on n type multi-layer-graphene/Si:P junctions. 78

3-2 Richardson activation plots as a function of T^{-1} from 250 K up to 330 K on multi-layer-graphene/Si:P. 79

3-3 Inverse square of capacitance per unit area measured at 1 kHz as a function of reverse bias at room temperature: multi-layer-graphene/Si:P. 79

3-4 Room temperature current density J with respect to applied bias V on n type multi-layer-graphene/GaAs:Si junctions. 80

3-5 Richardson activation plots as a function of T^{-1} from 250 K up to 330 K on multi-layer-graphene/GaAs:Si junctions. 81

3-6 Inverse square of capacitance per unit area measured at 1 kHz as a function of reverse bias at room temperature: multi-layer-graphene/GaAs:Si 82

3-7 Room temperature current density, J, with respect to applied bias V on n-type 4H-SiC/multi-layer-graphene junctions. 83

3-8 Inverse square of capacitance per unit area measured at 1 kHz as a function of reverse bias at room temperature on multi-layer-graphene/4H-SiC. 84

3-9 I-V characteristics of multi-layer-graphene/4H-SiC Schottky barriers from 300 K up to 900 K. 85

3-10 I-V characteristics of multi-layer-graphene/4H-SiC Schottky barriers from 300 K up to 800 K in the semilogarithic form. 86

3-11 I-V characteristics of multi-layer-graphene/4H-SiC Schottky barriers from 300 K up to 800 K in the semilogarithic form in the forward bias. 87

3-12 Semilogarithmic J-V characteristics of multi-layer-graphene/GaN:Si Schottky barriers from 5 K up to 330 K. 88

3-13 Semilogarithmic J-V characteristics of multi-layer-graphene/GaN:Si Schottky barriers from 5 K up to 330 K in the forward bias direction. 89

3-14 Richardson activation plots as a function of T^{-1} from 250 K up to 330 K on multi-layer-graphene/GaN:Si. 90

3-15 Bond polarization theory Schematics 91

4-1 Schematics of multi-layer-graphene / *n*-Si($1E^{16}$cm^{-3}). 106

4-2 Current density - voltage characteristics measured on MLG / *n*-Si before (red squares) and after the bromination (blue triangles). 107

4-3 X-ray diffraction pattern taken on HOPG and bromine doped HOPG at different doping times. 108

4-4 Auger electron spectroscopy data taken on brominated HOPG. 109

4-5 X-ray photoelectron spectroscopy data taken on the brominated HOPG sample. 110

4-6 Changes in the bandstructure at the metal-semiconductor interface before and after the chemical doping. 111

4-7 C^{-2} vs. V_R plots of MLG / *n*-Si. 112

4-8 Room temperature current density, J, with respect to applied bias, V, on MLG / *n* - 4H-SiC before (red squares) and after the bromination. 113

4-9 Plot of forward current at fixed voltage (1.85 V) with respect to the time. Bromine is turned on/off at specified times at the top of the graph. 114

5-1 One unit cell of graphene with translational vactors a_1 and a_2 121

5-2 Crystal structure of graphite showing consecutive layers with A B and A' B' atoms. 122

5-3 One unit cell of graphite with translational vactors a_1 and a_2 and c 123

5-4 The first brillouin zone of graphite and explanation of the bandstructure of the graphite. 124

5-5 The band structure of graphite near the high symmetry points H-K (or H'-K') as calculated from SWMc model. 125

6-1 X-ray photoelectron spectroscopy data taken on HOPG before and after the annealing. . . . 142

6-2 Temperature dependence of in-plane resistivity (ρ_{ab}) in HOPG from 1.7 K up to 900 K. . . . 143

6-3 Temperature dependence of the scattering rate, mobility and carrier density of graphite from 300 K down to 5 K. . . . 144

6-4 Temperature dependence of the in-plane resistivity from 1.7 K upp to 900 K. . . . 145

6-5 Temperature dependence of out-of-plane resistivity, ρ_c, in HOPG from 3K up to 300K. . . . 146

6-6 Temperature dependence of out-of-plane resistivity, ρ_c, in HOPG from 3K up to 1500K. . . . 147

6-7 Out-of-plane conductivity, σ_c, versus T^2 in the 300 K to 1500 K range and theoretical fit to the experimental data. . . . 148

6-8 Out-of-plane conductivity, σ_c, versus T^2 in the 300 K to 1500 K range. . . . 149

7-1 Plots of room temperature in-plane resistivity, ρ_{ab}, and carrier density, N (b), as a function of bromine intercalation time. . . . 165

7-2 Tranverse resistivity, ρ_{xy}, as a function of perpendicular magnetic field B at different intercalation times. . . . 166

7-3 Temperature dependence of ρ_{ab} and ρ_c at the indicated intercalation times. . . . 167

7-4 Infrared reflectance and optical conductivity, $\sigma_1(\omega)$, at different intercalation times. . . . 168

7-5 Optical conductivity of graphite and Br-doped graphite in the region of the 1588 cm^{-1}. . . . 169

7-6 Temperature dependence of magnetic susceptibility χ_c at the indicated intercalation times. . . . 170

7-7 Plot of $1/\tau$ determined from optical (blue triangles) and transport (red triangles) measurements. . . . 171

8-1 Raman spectrum taken on pristine and annealed 4H-SiC samples. . . . 176

8-2 Observation of D, G and 2D peaks after substraction of Raman spectrum taken on pristine and annealed 4H-SiC samples. . . . 177

8-3 Temperature dependence of in-plane resistivity of graphite grown on SiC . . . 178

8-4 AFM image taken on graphite SiC surface . . . 179

Abstract of Dissertation Presented to the Graduate School
of the University of Florida in Partial Fulfillment of the
Requirements for the Degree of Doctor of Philosophy

GRAPHITE-GRAPHENE SEMICONDUCTOR JUNCTIONS AND
MAGNETO-DIELECTRIC COUPLING IN SCHOTTKY DIODES

By

Sefaattin Tongay

December 2010

Chair: Arthur F. Hebard
Major: Physics

The goal of this dissertation is to incorporate graphite and graphene into today's semiconductor technology as a Schottky barrier diodes (metal/semiconductor junctions) that are widely used in metal semiconductor field effect transistors (MESFETs), high electron mobility transistors (HEMTs), high temperature and frequency devices, solar cells and sensors/detectors. The first part of the dissertation aims to give the reader a general idea about the physics at the metal-semiconductor junctions and essential theory background.

The second chapter of the dissertation questions effects of temperature and magnetic field on the diode characteristics of Schottky junctions. In this chapter, we present observation of negative magnetocapacitance on GaAs:Si/Au junctions and fully equipped with the theory, we present a phenomenological explanation for the observed effect.

In the third chapter, we for the first time introduce multi-layer-graphene as a metal (semimetal) electrode to form Schottky barriers on various technologically significant semiconductors such as Si, GaAs, SiC and GaN. Multi-layer-graphene/ semiconductor junctions not only display good current-voltage ($I - V$) and capacitance-voltage ($C - V$) characteristics but also are significant since the Schottky barrier height and characteristics are mainly governed by the interaction and bond formation at few layers

on the metal and semiconductor interface. This automatically implies that the presented results also hold for graphene/semiconductor junctions.

Chapter 4, takes the Schottky formation at the multi-layer-graphene(graphene)/ semiconductor junction to another level and aims to change the Fermi level of the metal electrode by intercalation with Bromine and tune the barrier height. Observed results are significant in MESFET technology since different barrier height are desired depending on the application.

The remainder of the dissertation, focuses on the properties of graphite and graphene to have more understanding about the content presented in the previous chapters. Chapter 5, gives a brief theory background about graphite and graphene while Chapter 6 and Chapter 7 discuss electrical properties of graphite at high temperatures where it starts to decouple from each graphene layer and acts as bi-layer graphene and with bromine intercation where there is c-axis lattice constant expansion and each graphene plane becomes more isolated. Chapter 8, gives a detailed description about epitaxial graphene growth in SiC by joule annealing technique, and we end the chapter with future directions.

CHAPTER 1
SEMICONDUCTOR THEORY AND SCHOTTKY BARRIER PHYSICS

1.1 Charge Carriers in Intrinsic and Extrinsic Semiconductors

The room temperature transport properties in a semiconductor are largely determined by the number of majority carriers, electrons in the conduction band and the holes in the valence band. Therefore, the density of these carriers plays a crucial role in the physical properties of the semiconductors used in today's semiconductor technology. This section aims to give an introductory background on the carrier statistics in the semiconductors which will be used frequently throughout the following chapters.

The density of the electrons in the conduction band can be written as product of the the the Fermi-Dirac function and the density of quantum states in the conduction band

$$n(E) = g_c(E)f(E), \tag{1–1}$$

and accordingly the density of holes in the valance band is,

$$p(E) = g_v(E)\left[1 - f(E)\right], \tag{1–2}$$

where $f(E)$ is the the Fermi-Dirac function and, $g_c(E)$ and $g_v(E)$ are respectively the density of quantum states in the conduction and valence bands. Integrating Eq. 1–1 (Eq. 1–2) over the conduction band (valance band) energy, the number of electrons (holes) can be written as

$$n_0 = \int g_c(E)f(E)dE, \tag{1–3}$$

and

$$p_0 = \int g_v(E)\left[1 - f(E)\right]dE, \tag{1–4}$$

In this dissertation, all the semiconductor wafers used, such as Si, GaAs, 4H-SiC, 6H-SiC and GaN, were *n*-doped, and therefore, the thermal equilibrium electron concentration in the conduction band will be derived in detail. However, similar steps can be done for the thermal equilibrium hole concentration in the valance band and its derivation is left to the interested reader.

By using the density of states in the conduction band in 3-dimensions and the Fermi-Dirac function, the concentration of electrons in the conduction band becomes

$$n_0 = \int_{E_c}^{\infty} \frac{4\pi \left(2m_n^*\right)^{3/2}}{h^3} \sqrt{E - E_c} exp\left[\frac{-(E - E_F)}{kT}\right], \tag{1–5}$$

In principle, the lower and higher limits of integration in Eq. 1–5 run from the minimum of the conduction band, E_c, up to the allowed states in the conduction band. However, this integral is typically taken to infinity since the the Fermi-Dirac function exponentially decreases with increasing energy. Moreover, the the Fermi-Dirac function is simplified as an exponential function since the Fermi energy is in the band gap and the $(E - E_F)$ term is much larger than the kinetic energy,kT.

Under all these assumptions, the integral of Eq. 1–5 is a Gamma function. The solution to this gives the thermal equilibrium electron concentration in the conduction band and is written as

$$n_0 = N_c exp\left[\frac{-(E_c - E_F)}{kT}\right], \tag{1–6}$$

where N_c is the effective density of states function in the conduction band,

$$N_c = 2\left(\frac{2\pi m_n^* kT}{h^2}\right)^{3/2}, \tag{1–7}$$

Eq. 1–6, 1–7 are generally used to estimate the number of electrons in the conduction band at a specific temperature and for a specific semiconductor with a given effective mass (m_n^*), position of the conduction band minimum and position of the Fermi level.

A similar set of two equations for holes can be expressed as

$$p_0 = N_v exp\left[\frac{-(E_F - E_v)}{kT}\right], \tag{1–8}$$

where N_v is the effective density of states function in the valence band,

$$N_v = 2\left(\frac{2\pi m_p^* kT}{h^2}\right)^{3/2}, \tag{1–9}$$

1.2 Intrinsic and Extrinsic Semiconductors

The equations derived above (Eq. 1–6 and Eq. 1–8) are typically used to calculate the total concentrations of electrons and holes in the conduction band and the valence band in any semiconductor. When there is no doping in the semiconductor, the concentration of electrons is equal to the concentration of holes and is called the *intrinsic carrier density* ($n_0 = n_i = p_0 = p_i$). These semiconductors are called *intrinsic semiconductors* and their Fermi energy becomes the intrinsic Fermi level, E_{Fi}. Using Eq. 1–6 and Eq. 1–8 with the intrinsic Fermi level,

$$n_i = n_0 = N_c exp\left[\frac{-(E_c - E_{Fi})}{kT}\right], \tag{1–10}$$

and,

$$p_i = p_0 = N_v exp\left[\frac{-(E_{Fi} - E_v)}{kT}\right], \tag{1–11}$$

When the intrinsic semiconductor is doped with either electron donating (donor) or hole donating (acceptor) atoms with the controlled amounts, the electric properties of the semiconductor change drastically. The conductivity of doped semiconductors can vary from semi-insulating up to very conducting thus enabling a wide range of use for industrial purposes. In this case, the total concentration of electrons is not equal to the total concentration of holes, the Fermi level of the system changes from intrinsic Fermi level (E_{Fi}) to the extrinsic Fermi level which is denoted as E_F. These

materials are called *extrinsic semiconductors*. ted as E_F. These materials are called *extrinsic semiconductors*.

An introductory idea about the nature of the dopings can be given as follows: In a silicon (Si) crystal, all the Si atoms are covalently bonded to each other. When a phosphorus (P) atom from a group V element having five valence electrons, is substitutionally added to the system, the P atom makes a covalent bonding in the Si matrix and the fifth valance electron acts as a donor electron. This semiconductor is called an n-type semiconductor. On the other hand, when doped with boron (B) atoms, a group III element with three valance electrons, hole dopes the system and the semiconductor is called p-type semiconductor.

For n-type semiconductors, for example phosphorus doped Si, the energy required to activate the donor electron in the P atom into the conduction band is much less than that for the electrons involved in the valance bonding in the Si matrix. An energy required to activate donor electrons from their dopants into the conduction band is referred as the *activation energy* ($E_{activation}$) or the *ionization energy* and the energy level located E_d below the conduction band created by the controlled amounts of dopants is called the *shallow energy level* and is located at E_d.

1.3 The Schottky Barrier (Metal-Semiconductor) Contacts

Metal - Semiconductor (M-S) contacts (*Schottky diodes*) are a very important part of today's semiconductor and optoelectronic devices. Schottky barriers formed at the metal - semiconductor interfaces are very delicate key components of metal - semiconductor field effect transistors (MESFETs) and high electron mobility transistors (HEMTs) which are widely used in high frequency, and high power device applications. The first observation of Schottky barrier formation and rectification across the metal semiconductor interface dates back to the early 1900s. When a metal contact is made on the semiconductor, the applied current is found to pass in one direction, but not the other. A metal - semiconductor interface with this rectifying property is called a *Schottky*

diode. Even though exciting and revolutionary for its time, reliability and reproducibility issues caused Schottky diodes to be replaced by more practical and easy to make $p - n$ junctions in the 1950s. After this point, the progress and development in the material science and engineering, and vacuum science and technology has allowed fabrication of reliable, reproducible, and practical metal - semiconductor contacts. Today, M-S contacts are very important part of semiconducting devices especially for semiconductors such as, such as SiC, GaN, GaAs, where there is no established oxide. In the absence of an oxide layer, field effect gating via thin insulating barrier is not possible and metal-oxide-semiconductor field effect transistors (MOSFET) can not be manufactured. For such semiconductors without a natural oxide, MESFET device configuration is used to induce an electrical field at the semiconductor interface across the depletion width of Schottky diode thereby depleting the interface of mobile carriers.

This section, we will give (1) a simple picture about the formation of the Schottky barrier across the M-S interface (2) explain the capacitive response and current/transport across the junction and deviation from the ideality at the interface, and (3) discuss commonly used Schottky barrier height measurement techniques.

1.3.1 Origin of the Schottky Barrier Formation at the M-S Interface

Metal - semiconductor contacts are ubiquitous in semiconductor technology not only because they are unavoidable, but also because the associated (Schottky) barriers to electronic transport across metal - semiconductor interface can be tuned by judicious choice of materials and processing techniques [1]. The most prominent characteristic of a Schottky barrier is its rectifying characteristic; the barrier acts like a diode with large currents flowing for forward bias and significantly smaller currents flowing for reverse bias [2]. If low resistance and “ohmic” (linear) I-V characteristics are desired, then materials and/or processing techniques are chosen to assure that the Schottky barrier height (SBH) ϕ_B is small compared to temperature ($\phi_B << k_B T$). This will be discussed later in this chapter. However, for typical Schottky diodes, Schottky barrier

heights are much larger compared to room temperature ($\phi_B >> k_B T$) and possess a strong non-linearity; a rectification. A Schottky barrier is formed between a metal and semiconductor interface due to a mismatch of the Fermi levels for the majority carrier on each side of the junction. The top panel of Fig. 1-1 shows the metal - semiconductor junction before thermal equilibrium for the case of a n-type semiconductor. In the figure, ϕ_m and ϕ_s represent the metal and semiconductor work functions respectively while χ is the electron affinity.

After thermal equilibrium is achieved [Fig. 1-1, bottom panel], electrons from the semiconductor flow into the lower lying energy states on the metal side to make the Fermi level (E_F) constant throughout the system, leaving positively charged donor atoms behind. The positively charged donor atoms on the semiconductor side create a space charge region and the associated Schottky barrier. Positively charged donor atoms on the semiconductor side create an electrical field preventing electrons from flowing from the metal to the semiconductor, but allowing electrons to flow from semiconductor to the metal, hence the rectification. After the equilibrium is achieved the Schottky barrier ideally would be given by (Fig. 1-1),

$$\phi_B = (\phi_m - \chi)\,, \tag{1–12}$$

However, deviations from the ideal case might alter the expected Schottky barrier height given in Eq. 1–12 and these additional processes will be discussed in Section 1.3.4.

Since the barrier seen from metal side is different than the barrier seen from the semiconductor side, the potential seen by the electrons on the metal side is referred to as the Schottky barrier while the potential seen by the non-localized electrons on the conduction band of the semiconductor side is referred to as the built-in potential barrier (V_{bi}), where V_{bi} is the energy difference between the conduction band of the

semiconductor and the Fermi energy. The doping dependence of χ makes V_{bi} weakly dependent on the semiconductor doping.

1.3.2 Depletion Capacitance at the M-S Interface and C-V Relationship

After thermal equilibrium is achieved, positively charged donor atoms created in the depletion area [Fig. 1-1 bottom panel] create an electrical field within the depletion width (W). Moreover, at thermal equilibrium, electrons from the semiconductor accumulate a thin layer of electrons on the metal side. All the positively charged donor atoms can be pictured as a layer of positive charges at $x = W$ [Fig. 1-1 bottom panel]. Within the parallel plate capacitor approximation, this gives rise to a capacitance at the interface called the *junction capacitance*. The magnitude of the electrical field, E, in the depletion region of the junction and hence the electrostatic properties of the Schottky junction can be determined solving the Poisson's equation which has the form,

$$\frac{dE}{dx} = \frac{\rho(x)}{\epsilon_s}, \tag{1–13}$$

where the ϵ_s and $\rho(x)$ are defined as permittivity of the semiconductor and the space charge volume density in the depletion area. As discussed in Chapter 1.2, it is much harder to activate the electrons involved in the covalent bonding in between Si-Si atoms, compared to activating donor electrons having activation energies on the order of room temperature of less. It is therefore generally assumed that all the donor atoms in the depletion area are already positively charged and the density of the charged donors is constant. This constant density approximation is typically called as the *abrupt junction approximation* (AJA) and within this approximation the density of positively charged donor atoms equals to the doping density of the semiconductor (N_d). Following Eq. 1–13 and AJA,

$$E = \int \frac{eN_d}{\epsilon_s} dx = \frac{eN_d x}{\epsilon_s} + \alpha, \tag{1–14}$$

where α is a constant of the integration. Since the electric field has to be zero at the edge of the depletion width on the semiconductor side (W away from the metal - semiconductor interface), α can be determined to be

$$\alpha = -\frac{eN_d W}{\epsilon_s}, \tag{1–15}$$

Using Eq. 1–14 and 1–15,

$$E = -\frac{eN_d(W - x)}{\epsilon_s}, \tag{1–16}$$

According to Eq. 1–16, the electric field determined from Poisson's equation and under the AJA approximation varies linearly with the distance from the metal - semiconductor interface. However since the electric field is zero inside the metal contacts, there always exist a negative charge at the interface making the total electric field zero.

$$E_{x=0} = 0, \tag{1–17}$$

and the potential difference from $x = 0$ to $x = W$ (or V_{bi}) can be calculated by integrating the electrical field and using Eq. 1–16. The potential difference reads,

$$\phi(x) = \int E(x)dx = \int -\frac{eN_d(W - x)}{\epsilon_s}dx, \tag{1–18}$$

$$\phi(x) = -\frac{eN_d(Wx - \frac{x^2}{2})}{\epsilon_s} + \beta, \tag{1–19}$$

The potential difference from x=0 to x=W will be equal to the built-in potential value, V_{bi}.

$$V_{bi} = |\phi(x = W)| = \frac{eN_d W^2}{2\epsilon_s}, \tag{1–20}$$

and depletion width reads,

$$W = \left[\frac{2\epsilon_s\left(V_{bi} - V_R\right)}{eN_d}\right]^{1/2}, \tag{1–21}$$

where the V_R is defined as the potential applied in between the metal (positive side) and the semiconductor (negative side).

Once thermal equilibrium is achieved, charges in the depletion width are roughly separated on the metal side (negative charges) and the semiconductor (positive charges) creating a junction capacitance. However upon application of the reverse bias voltage, V_R, across the junction, more positive and negative charges will be accumulated at the semiconductor and metal side respectively. The junction capacitance can therefore be written as,

$$C_{depletion} = \frac{dQ}{dV_R}, \tag{1–22}$$

and using AJA, the charge in the depletion area is

$$dQ = eN_d dx, \tag{1–23}$$

hence,

$$C_{depletion} = eN_d\frac{dx}{dV_R} = \left[\frac{e\epsilon_s N_d}{2\left(V_{bi} + V_R\right)}\right]^{1/2}, \tag{1–24}$$

where the $C_{depletion}$ is the capacitance per unit area.

1.3.3 Transport Across the M-S Interface: Thermionic Emission

After the formation of the Schottky barrier, the current transport across the Schottky barrier is mainly dominated by the majority carriers. When the Schottky barrier height is much larger than kT, the Maxwell-Boltzmann distribution still applies and thermal equilibrium is not affected, and this approximation is called the *thermionic emission process*. In thermionic emission, the total current density across the metal - semiconductor interface has two current components: (1) a current density from metal

into the semiconductor, $J_{m\to s}$, and (2) from semiconductor into the metal $J_{s\to m}$. The total current reads,

$$J_{total} = J_{s\to m} + J_{m\to s}, \tag{1–25}$$

The current density from the semiconductor into the metal ($J_{s\to m}$) is given by the integral of the concentration of electrons with energies large enough to overcome the Schottky barrier for thermionic emission into the metal,

$$J_{s\to m} = e\int_{E_F+e\phi_B}^{\infty} \nu_x dn, \tag{1–26}$$

where ν_x is the velocity in the direction of the electronic transport, ϕ_B is the Schottky barrier height and dn is the electron density given by,

$$dn = g_c(E)f(E)dE, \tag{1–27}$$

In this equation, the $f(E)$ is the Fermi function and the $g_c(E)$ is the density of states in the conduction band. Writing the dn with the similar assumptions and simplification made in the transition from Eq. 1–3 to Eq. 1–5 we arrive at the expression,

$$dn = \frac{4\pi\left(2m_n^*\right)^{3/2}}{h^3}\sqrt{E-E_c}exp\left[\frac{-(E-E_F)}{kT}\right]dE, \tag{1–28}$$

Under the assumption that all the energy of the free electrons in the conduction band is simply the kinetic energy, then we have

$$\frac{1}{2}m_n^*\nu^2 = E - E_c, \tag{1–29}$$

Using equations 1–28, 1–29 in Eq. 1–26,

$$J_{s\to m} = A^* T^2 exp\left(-\frac{e\phi_B}{kT}\right)exp\left(-\frac{eV}{kT}\right), \tag{1–30}$$

where A^* is *the effective Richardson constant* and given as $A^* = \frac{e4\pi m^* k^2}{h^3}$.

Following similar steps for the current density from metal into the semiconductor ($J_{m\to s}$),

$$J_{m\to s} = -A^* T^2 exp\left(-\frac{e\phi_B}{kT}\right), \tag{1–31}$$

and using Eq. 1–30 and Eq. 1–31 in Eq. 1–25, the total current across the metal semiconductor junction reads

$$J_{total} = \left[A^* T^2 exp\left(-\frac{e\phi_B}{kT}\right)\right]\left[exp\left(\frac{eV}{kT} - 1\right)\right], \tag{1–32}$$

where V is the applied potential [2, 3]. Under thermionic emission, the total current density across the junction can be expressed by Eq. 1–32 and is frequently used in the current literature to extract out the Schottky barrier (section 1.3.5.1). However deviations from this ideal case can alter the experimental data and might result in errorous interpretations. The next section will discuss these additional processes.

1.3.4 Non-Ideal Effects at the M-S Interfaces

1.3.4.1 Image force lowering or schottky effect

An electron in a dielectric medium at a distance from the metal will create a positively charge carrier on the metal side at the metal - semiconductor interface. However, this effective charge accumulated at the metal surface can be imagined as an effective charge located in the metal at a distance -x from the interface. In this case, there will be an interaction in between the electron in the dielectric (studied semiconductor) and an effective charge in the metal. This coulomb interaction is called an *image force* and the charge formed on the metal side is known as the *image force charge*. As a result of this image force, electrons on the semiconductor side are attracted to positive image charges in the metal created by those electrons. Thermally activated electrons overcoming the barrier at the metal - semiconductor interface experience this additional coulomb interaction and effectively the electrons

overcome the barrier height easier, leading to an reduction / lowering in the Schottky barrier height. The lowering of the Schottky barrier height as a result of interaction in between the image charge and the electrons is called either *image force lowering* or *Schottky effect* and can be written as [2, 3],

$$\Delta\phi_B = \sqrt{\frac{eE}{4\pi\epsilon_s}}, \tag{1–33}$$

or in terms of built-in potential and doping density N_D [1],

$$\Delta\phi_B = \sqrt{\frac{e^3 V_{bi} N_D}{8\pi^2\epsilon_s^3}}, \tag{1–34}$$

The magnitude of the image force lowering typically varies from 1 meV up to 50 meV depending on the semiconductor, and doping level and most times it constitutes a very small portion of the total Schottky barrier height.

1.3.4.2 Thermionic field emission

Another mechanism giving a correction term to the predicted Schottky barrier height takes place mostly at low temperatures and is called *thermionic field emission* (TFE) [4]. On heavily doped semiconductors, the number of carriers tunneling across the barrier with energies less than the Schottky barrier height might exceed the number of thermally activated carriers over the Schottky barrier. The balance between the sharp increase in tunneling probability across the Schottky barrier (tunneling barrier width is narrower for higher electron energies) and the decrease in carrier density with electron energy, results in tunneling of carriers across the Schottky barrier despite their energies being too small overcome the barrier. This results in an effective decrease of the Schottky barrier height. TFE theory first consider by Padovani [4] along with the WKB approximation, finds that the TFE Schottky barrier height lowering can be calculated as,

$$\Delta\phi_B = \left[\frac{9}{4}E_{00}^2 V_{bi}\right]^{1/3}, \tag{1–35}$$

where E_{00} is

$$E_{00} = \frac{e\hbar}{2}\left[\frac{N_D}{\epsilon_s m^*}\right], \tag{1–36}$$

1.3.4.3 Direct tunneling

The thermionic field emission (TFE) process requires mobile electrons on the semiconductor side to be thermally activated to particular energies less than that of the Schottky barrier height and tunnel across the metal - semiconductor interface. However, as the temperature at which the Schottky diode is measured/operating at is decreased, even though electrons will not have enough energy to go over the Schottky barrier or to be excited to a point where they can tunnel (TFE) but they will naturally tunnel across the Schottky barrier. In such cases, the interpretation of the Schottky barrier is rather difficult and controversial. Direct tunneling typically gives non-ideal $J - V$ characteristics that can not be explained by thermionic emission theory.

1.3.5 Measurement of Schottky Barrier Height

1.3.5.1 Current-voltage characteristics

The current density across the metal - semiconductor interface has been discussed and derived in subsection 1.3.3 and the total current density reads,

$$J_{total} = J_{sat}\left[exp\left(\frac{eV}{kT} - 1\right)\right], \tag{1–37}$$

where J_{sat} is the *reverse saturation current density*

$$J_{sat} = \left[A^* T^2 exp\left(-\frac{e\phi_B}{kT}\right)\right], \tag{1–38}$$

Following from Eq. 1–37, when the applied bias eV is much larger than the thermal energy kT ($eV >> kT$), the numeral -1 inside bracket can be ignored. In this case, when the measured current is plotted semilogarithmically with respect to the applied bias, it is expected to be linear. However, in reality the additional current processes

discussed in section. 1.3.4 display different dependencies on the applied bias, resulting in a deviation from linearity. The deviation from the linearity is typically accounted for by introduction of a parameter, η, inside the exponential and is normalized to $\eta = 1$ (linear) for current completely originating from thermionic emission process and $\eta > 1$ when other non-ideal effects contribute to the measured total current. With the inclusion of this additional parameter, the total current across the M-S interface is written as,

$$J_{total} = J_{sat}\left[exp\left(\frac{eV}{\eta kT} - 1\right)\right], \tag{1–39}$$

Here the parameter η is called the *ideality factor* and written as a inverse slope of the $J - V$ plot.

$$\eta = \frac{1}{kT/e \cdot dln(J_{total})/dV}, \tag{1–40}$$

The ideality factor is a measure of deviation from ideality (thermionic emission process) and reaches to values larger than one when other non-linear current processes contribute to the total measured current.

The $J - V$ measurement provides a to measure of the effective barrier height at the metal - semiconductor interface after thermal equilibrium is achieved. When the total current is measured with respect to different applied bias values, it is expected to pass significantly more current in the forward bias direction. In general the measured $J - V$ is expected to span enough linear range in the semi-log current density and voltage plot such that one can make an extrapolation to the y-axis and determine the saturation current density, J_{sat}. Once J_{sat} is known Schottky barrier height can be determined using Eq. 1–38. although a simple task, extraction of the Schottky barrier's has always been open to questions, doubts and controversies due to the additional current processes to thermionic emission process and deviation from linearity in the ideality factor ($\eta > 1$). Nevertheless, the $J - V$ technique is known to be very standard and powerful technique as a measure of the barrier height.

Even though extraction of Schottky barrier from measured $J-V$ characteristics and use of thermionic emission is a powerful, practical and standard technique, Eq. 1–39 leads to a deviation from the true Schottky barrier height especially at metal - semiconductor interfaces where the value of the metal contact area is not exactly known. In such cases, metal electrodes placed on the semiconductor do not make 100% physical contact at the interface and the true value of the current density can not be determined. Since the value of the current density (J) or the effective current density (J_{sat}) can not be determined, Eq. 1–39 is written in terms of current and saturation current density as follows,

$$I_{total} = I_{sat}\left[exp\left(\frac{eV}{\eta kT} - 1\right)\right], \tag{1–41}$$

and

$$I_{sat} = \left[A \cdot A^{*} \cdot T^{2} \cdot exp\left(-\frac{e\phi_B}{kT}\right)\right], \tag{1–42}$$

here, the saturation current density, I_{sat} can be written as,

$$ln\left(I_{sat}/T^{2}\right) = ln\left(AA^{*}\right) - e/kT \cdot \phi_B, \tag{1–43}$$

In Eq. 1–43, the unknown contact area is only present in the first term of the right hand side of the equation. Therefore if one plots the natural logarithm of the saturation current at specific temperatures divided by square of temperature, $\ln I_{sat}/T^{2}$, with respect to the inverse temperature, T^{-1}, the dependence will be linear and the slope of the $\ln I_{sat}/T^{2}$ versus T_{-1} yields the Schottky barrier height. This method is often refered as an *activation energy measurement* and has an advantage over the conventional $J-V$ method since no assumption of the Schottky diode area is required.

1.3.5.2 Capacitance-voltage characteristics

The presence of V_{bi} in the depletion capacitance expression (Eq. 1–24) derived in section 1.3.2 allows one to calculate the magnitude of the depletion capacitance at the M-S interface once depletion capacitance is measured experimentally and the dielectric constant and the doping level of the semiconductor is known. Typically the depletion capaticance in Eq. 1–24 is written as,

$$\frac{1}{C^2} = \frac{2\,(V_{bi} + V_R)}{e\epsilon_s N_D}, \tag{1–44}$$

According to Eq. 1–44, when the measured capacitance is plotted as $1/C^2$ versus V_R a linear dependence should be observed. An intersection of the line with the abscissa gives the built-in potential value V_{bi} while the slope of the plot is $2/(e\epsilon_s N_d)$. This technique is commonly referred to as the *C-V measurement technique* in the literature for determining the value of the built-in potential (V_{bi}). Once the built-in potential known, one can determine the Schottky barrier height as follows (Fig. 1-1 bottom),

$$\phi_B = V_{bi} + \frac{E_c - E_F}{e} = V_{bi} + \frac{kT}{e} \cdot ln\left(\frac{N_c}{N_d}\right), \tag{1–45}$$

where N_c, N_d and V_{bi} are respectively the effective density of states function in the conduction band (Eq. 1–7), the doping density of the semiconductor and the built-in potential determined from the $C-V$ measurement method.

Eventhough, both $J-V$ and $C-V$ measurements both aim to determine the Schottky barrier height, these two methods fundamentally differ from each other in the following ways. (1) $J-V$ method directly measures ϕ_B while the $C-V$ method only measures V_{bi} (2) While the $J-V$ method mimics the transport across the barrier, the $C-V$ method probes the depletion width rather than strictly the Schottky barrier height and M-S interface. (3) Since the $J-V$ method measures the current across the barrier height, measured current often passes through the lowest Schottky barrier patches. On

the other hand, $C-V$ measures the depletion capacitance at the interface and gives an average value for the built-in potential. In the literature, these two methods are often considered complementary and $C-V$ method gives slightly higher values comparing to extractions from the $J-V$ methods.

1.3.5.3 Internal photoemission technique

Another method to measure the Schottky barrier height is known as the internal photoemission technique. In this technique, monochromatic light at different photo energies is directed at the metal side. Generally metal electrodes are selected to be thin enough to insure that light penetrates into the semiconductor with enough intensity to reach the M-S interface and excites the electrons from the Fermi level of the metal. When the photo energy is high enough, those excited electrons are activated over the Schottky barrier and a current is measured flowing through the metal - semiconductor interface. This current is called *the photoelectric current* and is described by the Fowler equation [5],

$$I_{photoemission} = (h\nu - \phi_B)^2 , \tag{1–46}$$

where ν is the frequency of the photon. When the photoelectric current is plotted as $I_{photoemission}^{1/2}$ against the photon energy, extrapolation of the linear dependence to an intercept with the photon energy axis gives the Schottky barrier height. The light source used in this technique must be in the range of the Schottky barrier height and the band gap.

In this method, the photoelectric current created by illimunation of the Schottky barrier is expected to be very small and therefore leakage and noise can be an issue. This technique is generally performed in a ac mode with a chopped light source and synchronome detection of the photocurrent with a lock-in amplifier.

1.4 Ohmic Contacts to Semiconductors

One of the most important parts of the any device is the contact made from the produced device to the outside world. These contacts are expected to display very low resistance at the junction area and linear dependence of the current across the contact with respect to the applied bias, meaning, it should pass current from metal into the semiconductor and semiconductor into the metal. These type of junctions (contacts) are called *ohmic contacts* and display very small, zero and negative barrier height at the metal - semiconductor interface. Typically, these contacts can be made to various types of semiconductor by specially tailored methods for each semiconductor.

The first method is known as the traditional ohmic contact. When the Fermi level of the metal and the semiconductor is equal or if the metal Fermi level is slightly higher, an ohmic contact forms at the interface. However, in principle it is rather difficult to align or find a proper material with appropriate Fermi level values to induce ohmic contacts on the samples.

The second method utilizes tunnel barriers. In this method a metal contact with a positive barrier at the M-S interface is formed in such a way that there is high enough doping in the semiconductor so that there is only a thin barrier separating the metal from the semiconductor. If the width of the depletion region at the metal - semiconductor interface is very thin, on the order of 3 nm or less, carriers can readily tunnel across such barrier.

And the last and the most used method utilizes rapid thermal annealing (RTA). In this method, the relative positions of the Fermi level at each side of the contact is not considered. Instead, this method relies on the fact the barrier formed at the metal - semiconductor interface can be significantly lowered by annealing. The fabrication of these ohmic contacts generally involves a high temperature rapid thermal annealing such that the unintentional barrier at the interface is lowered by thermally-induced

diffusion of metal and a semiconductor at the interface, creating a uniform transition from metal into the semiconductor through the new alloy formed at the interface.

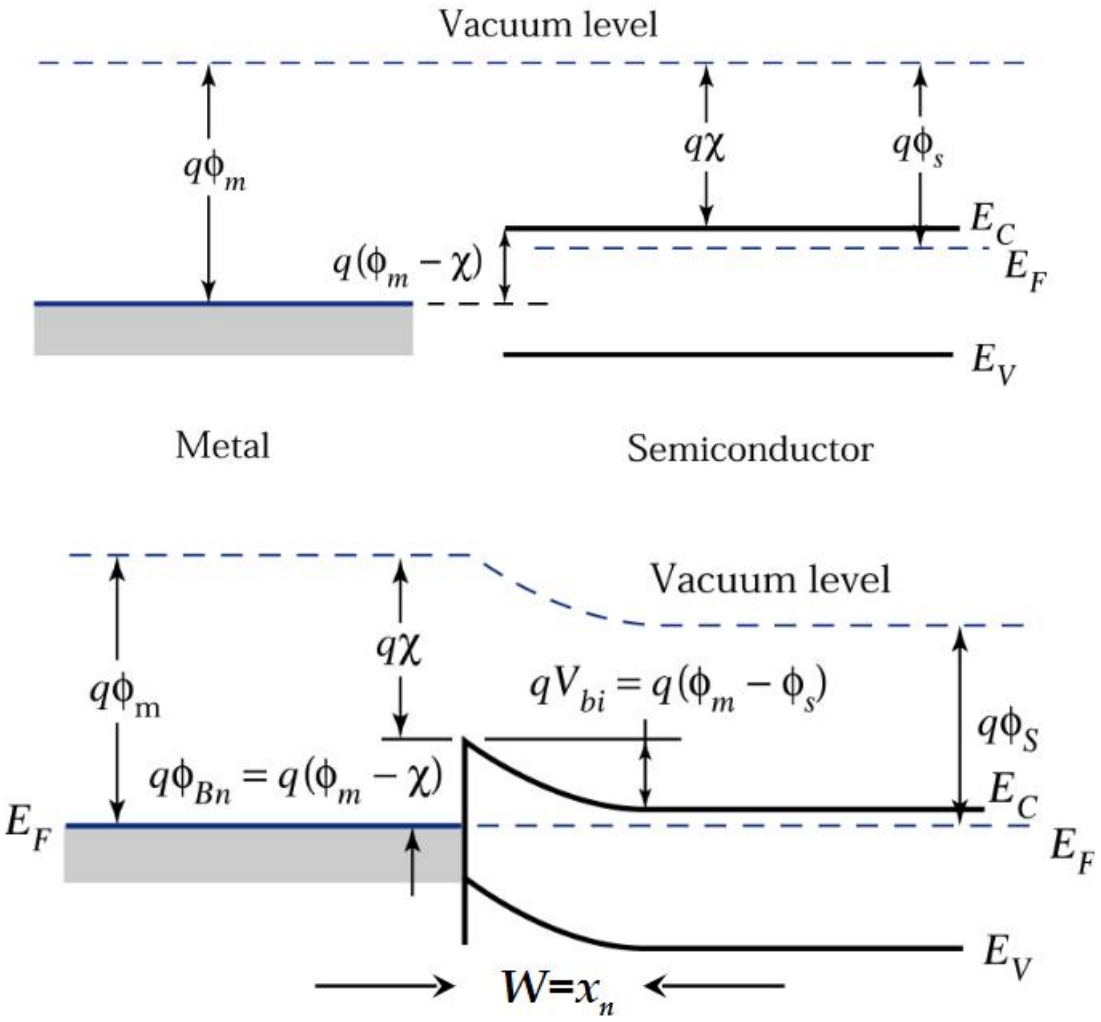

Figure 1-1. Energy diagram of metal/semiconductor junction diode

CHAPTER 2
MAGNETODIELECTRIC COUPLING IN NON-MAGNETIC AU / GAAS : SI SCHOTTKY DIODES

2.1 Introduction

Electronic transport across metal-semiconductor interfaces, which are ubiquitous in semiconductor technology, is mediated by the formation of Schottky barriers and associated depletion capacitance. Numerous studies have established the relationship between the Schottky barrier height and materials properties and have at the same time fully characterized the dependence of electronic transport across metal-semiconductor interfaces on temperature, frequency and voltage bias/polarity [1, 2, 6–11]. Despite decades of investigations and the use of concepts such as metal induced gap state models [6, 7] and bond polarization theory [1, 8] a consensus understanding of Schottky barriers has not been reached. Schottky contacts on the semiconductor GaAs are particularly interesting due to considerations such as a long spin life time in GaAs [12], the demonstration of spin polarized current injection from a metal into GaAs [13] and spin extraction from GaAs into a metal [14]. An additional gap in knowledge however becomes apparent with the realization that there are relatively few studies of the effect of externally applied magnetic fields H on the electrical properties of Schottky barriers.

We address this deficiency by reporting on a surprisingly large negative magneto capacitance (MC$>$20%) associated with Au/GaAs(Si) Schottky barrier samples fabricated and characterized by standard techniques as described below. The MC is independent of field direction and is unexpected because (1) there are no magnetic impurities in the Au/GaAs(Si) system and (2) the GaAs(Si) is homogeneous and thus not a candidate for magnetocapacitance in nonmagnetic composite media [15]. Clearly, such large MC effects in non-magnetic semiconductor systems must be explained before the behavior of metal-semiconductor interfaces involving spin-polarized metals and/or dilute magnetic semiconductors (DMS) for spintronics applications [16] can

be understood. Using a combination of current-voltage, capacitance (C) and internal photoemission (IPE) studies, we show that the MC can be attributed to a novel magneto dielectric coupling in which a H-induced increase in the binding energy of the Si donor impurities strongly affects the density of ionized impurities (N_d) within the depletion width of the Schottky barrier, and hence the polarization. We identify the ionization and capture transitions between the shallow impurity E_{sh} and conduction E_c bands (schematic of Fig. 2-2 inset) and show that the apparent large H-induced increase of the built-in potential V_{bi} deduced from linear $1/C^2$ versus reverse-voltage bias V_R plots is not due to a change in the Schottky barrier height (SBH), but rather to a field induced increase in the binding energy, E_a=$E_c - E_{sh}$, of the Si donor impurities. The increase in E_a with respect to H (carrier freeze out) has been previously studied as a bulk effect both theoretically [17] and experimentally using optical [18, 19] and Hall measurements [20, 21]. Magnetic field tunability of the Schottky capacitance due to field-induced carrier freezeout is an interface effect that offers a new degree of freedom in the design and application of magneto electronic devices.

2.2 Experimental Methods

2.2.1 Sample Preperation

Commercially available (Sumitomo Electric Europe Ltd.) GaAs wafers with a nominal Si dopant density of $3 \cdot 10^{16} cm^{-3}$ were used. Ohmic contacts were made based on multilayer recipes existing in the literature [22–24]. Rapid thermal anneals in nitrogen gas at temperatures in the range 400C - 460C assured good ohmic contact with low parasitic resistance down to temperatures as low as 10 K. Prior to evaporating the front-side Au Schottky contact, the samples were thoroughly cleaned in $3:1:50 HNO_3:HF:H_2O$ for 3-4 minutes to remove any native oxide. Schottky contacts ranging in diameter from 100μm to 1000μm were formed by thermal evaporation of Au at a base pressure of 10^{-7} Torr. Nine separate samples prepared with different contacts were studied, all giving similar results. At room temperature, the experimental values

for N_d determined from $1/C^2$ vs V measurements (section 1.3.5.2 and Eq. 1–44) were found to be in the $1-2\cdot10^{16}$ cm^{-3} range consistent with the Hall data results.

2.2.2 Current-Voltage Measurements

The current voltage ($I-V$) characteristics of a high quality Schottky diode should exhibit pronounced asymmetry with respect to the sign of the bias voltage and also be well described in forward bias by thermionic emission [1–3] (Eq. 1–39). These attributes are satisfied for our samples as shown in Fig. 2-1a by the forward and reverse bias I-V characteristics, measured at 300 K and 20 K, of the same Au/GaAs : Si Schottky sample on which ac impedance measurements are performed. When measured current is plotted as ln$I$ versus V, in the forward bias current increases rapidly as the voltage is applied and in the reverse bias diodes acts more resistive and gives commonly known as *leaf plots* in top panel of Fig. 2-1. At 300 K the Schottky barrier height, ϕ_{SBH}, and the ideality factor, η, are extracted for a total of nine different samples using thermionic emission theory [1–3] (Eq. 1–39 and 1–40) and found to be respectively in the ranges 0.82V$<\Phi_{SBH}<$0.92V and 1.05$<\eta<$1.15. These values are in good agreement with the current literature [1, 2] and with our IPE data discussed below. At low temperature (20 K) the $I-V$ characteristics of the same sample (Fig. 2-1b, blue diamonds) show similar rectifying behavior; reliable barrier parameters however cannot be extracted using thermionic emission theory because of competing processes such as generation-recombination, quantum tunneling and thermionic-field emission [1, 4] taking place at low temperatures as discussed in subsection 1.3.4. Measured current across the M-S interface displayed a magnetic field dependence at various biases as shown in bottom panel of Fig. 2-1. However, the ideality factor at 20 K is measured to be much larger than the ideal thermionic case ($\eta >> 1$). This implies that the total measured current is governed by many other transport processes as discussed in subsection 1.3.4. and extraction of Schottky barrier height at different applied magnetic fields becomes problematic.

2.2.3 Capacitance-Voltage Measurements

Complex impedance measurements over a frequency range 20 Hz-1 MHz were made using an Agilent HP4284 capacitance bridge. The output of the bridge can be interpreted by one of two different models each having two unknowns : a resistance R_s in series with a capacitance C_s (series model) or a resistance R_p in parallel with a capacitance C_p (parallel model). The simplest model for a Schottky diode however involves at least three unknowns : R_Σ in series with a two-component complex capacitance C^* which comprises the capacitance C=$Re\{C^*\}$ of the depletion region in parallel with a loss term that represents dc transport (tunneling) and ac loss due to changes in polarization. It is straightforward to show that C is bounded by C_s and C_p ($C_s > \mathrm{C} > C_p$) and that if C_s is found to be close to C_p, then R_Σ is small and can be ignored [11]. For the measurements reported here we find at most C_s=1.07C_p, thus implying the narrow constraint 1.07$C_p > \mathrm{C} > C_p$, and hence the assurance that the measured C_p of the parallel model accurately represents the depletion capacitance C_{dep}. Since R_Σ is negligible, then any field dependence of R_Σ is also negligible, and we can conclude that the measured MC is associated with the Schottky depletion capacitance rather than magnetoresistance in the contacts or bulk masquerading as magnetocapacitance [25]. At temperatures lower than the 20 K, a rapid increase in R_Σ manifests itself as a large difference in C_p and C_s ($C_s >> C_p$), and C_p is no longer an accurate measure of the depletion capacitance [11]

2.2.4 Internal Photoemission Technique

Another direct measure of Φ_{SBH} is internal photoemission technique. In this method, the sample is mounted in a cryostat and illuminated by ac modulated light emerging from an optical fiber [26]. The internal photocurrent through the sample is synchronously demodulated and the square root of the photoyield defined as the photocurrent per incident photon, is plotted against photon energy. A linear extrapolation to zero gives the

minimum energy (Eq. 1–46), Φ_{SBH}, necessary to excite electrons from the Fermi energy of the metal over the barrier. The results will be discussed later in this chapter.

2.3 Experimental Results

2.3.1 Observation of Magnetocapacitance and Magnetic Field Dependence of $C-V$ Curves

In Fig. 2-2 we show as our main result the effect of magnetic field on capacitance. The magnitude of the relative change in capacitance $\Delta C_{dep}/C_{dep}$ measured at frequency f=1 MHz and over a field range of 0-70 kOe is observed to increase as the temperature T is lowered from 300 K to 20 K. Near freeze-out temperatures [27] the MC grows rapidly, reaching -21% at H=70 kOe and T=20 K. To understand these data, we generalize the Mott-Schottky (M-S) picture1 [2] by explicitly including the independent variables, f, T and H, and re-writing Eq. 1–44 as,

$$\frac{1}{C_{dep}(f,H,T)^2} = \frac{2\left(V_{bi}(f,H,T)+V_R\right)}{e\epsilon_s N_D(f,H,T)}, \tag{2–1}$$

$$W(f,H,T)^2 = \left[\frac{2\epsilon_s\left(V_{bi}(f,H,T)+V_R\right)}{eN_D(f,H,T)}\right]^{1/2}, \tag{2–2}$$

where ϵ_s is the dielectric constant of the semiconductor, V_R is the magnitude of the applied reverse bias voltage (metal electrode is negative), and $N_d(f,T,H)$ is the density of ionized Si impurities within the depletion width $W(f,T,H)$. In the M-S picture a term equal to k_BT, is subtracted from V_{bi} in the numerator [1]. However this term is typically much smaller than the measured V_{bi} and often neglected [2] as it is in our case, since our measured values of V_{bi} near 1eV assure the inequality $V_{bi}>>k_BT$ at room temperature and below. In agreement with Eq. 2–1, a linear dependence of $1/C_{dep}^2$ with respect to V_R is found at f=1 MHz for different H (Fig. 2-3, top panel) and at H=0 for different f (Fig. 2-3, bottom panel). For each data set there are two extracted parameters: the slope, from which $N_d(f,T,H)$ can be calculated (Eq. 2–1), and the intercept $V_{bi}(f,T,H)$, the built-in potential. At room temperature almost all the donor

electrons are excited into the conduction band leaving the donor atoms fully ionized with a density $N_d^0(T = 300\ K) \approx N_d$. However, temperature and magnetic field freeze-out take place at lower temperatures, and $N_d(f, T, H)$ becomes a function of H at fixed T as shown in Fig. 2-4. The related changes of $V_{bi}(f, T, H)$ are also shown in the same figure. We note that $N_d(f, T, H)$ and $V_{bi}(f, T, H)$ extracted from the linear plots of Fig. 2-3 can be used in Eq. 2–1 to calculate the MC (squares in Fig.2 for T=20 K) and are found to be in good self-consistent agreement for all measured f, T and H. The remainder of this chapter will focus on elucidating the magnetodielectric coupling that gives rise to the pronounced f, T and H dependence of the extracted M-S parameters of Eq. 2–1 and the associated MC shown in Fig. 2-2.

2.3.2 Physical Processes in the Depletion Width

The underlying physical processes are revealed in the frequency-dependent capacitance and loss plots of Fig. 2-5. There are two prominent loss peak regions: the first low-frequency region extends over the frequency range 100 Hz to 10 kHz and the second high-frequency region, with more pronounced loss, extends from 10 kHz to greater than the 1 MHz limit of our capacitance bridge. With decreasing T and/or increasing H, the lossy regions move to lower frequency as shown in the successive panels of Fig. 2-5. In principle if the electrical field is slowly varying in the depletion width region, one might expect to see only one loss peak. However, when there is more than one dielectric relaxation process contributing to the measured capacitance, multiple loss peaks centered at different frequencies, each adhering to a Debye response, can be observed providing there is sufficient resolution.

We find that each loss curve is well described by the imaginary part of the ubiquitous Cole-Cole expression [28] for the generalized dielectric constant,

$$\epsilon = \epsilon_\infty + \frac{\epsilon_0 - \epsilon_\infty}{1 + (i\omega\tau)^{(1-\beta)}}, \tag{2–3}$$

where ϵ_∞ and ϵ_0 are the dielectric constants in the high and low frequency limits, β is a constant smaller than one, τ is a relaxation time and ω the angular frequency. The analysis of the low-frequency peaks is straightforward, since the frequency range is broad enough to include the full peak, thereby enabling us to determine in a straightforward manner the peak frequency f_p=$1/\tau$ and a corresponding relaxation time τ at which the loss for a particular T and H peaks at a maximum. For constant H the relaxation rate τ^{-1} adheres to a thermally-activated Arrhenius dependence, τ^{-1}= $\tau_0^{-1} exp(-E_a/k_B T)$, where E_a is an activation energy and τ_0^{-1} a prefactor. The semilogarithmic plot of τ^{-1} versus $1/T$ for the low-frequency peak shown in the inset of Fig. 2-6 (H = 70 kOe) manifests typical activated response. The field-dependent activation energies $E_a(H)$ are extracted from the slopes of these lines and plotted in the main panel of Fig. 2-6 against field (red squares) for the low-frequency loss peaks.

Since the amplitude and shape of the low-frequency loss peaks remain constant and are shifted only laterally with temperature/field (Fig. 2-5), we can extract similar activation energies for the high-frequency peaks by monitoring the temperature dependence of an arbitrary point (half amplitude) rather than the peak. By making the reasonable assumption that the high-frequency peaks also have an invariant amplitude and shape, we extract the activation energies shown as blue circles in Fig. 2-6. The error bars on these data are larger because the high frequency portions of these peaks are greater than 1 MHz, and there is consequently greater uncertainty in the parameters of the Cole-Cole fits.

The loss peaks of Fig. 2-5 correspond to two relaxation processes, each having similar activation energies which increase with magnetic field (Fig. 2-6). At H=0, E_a=6.05$\pm$0.20 meV and 5.73$\pm$0.13 meV for the low and high peaks respectively, very close to the reported values of 5.8 meV [2, 21] for Si impurities in GaAs. We therefore attribute the two observed loss peaks to ionization from E_{sh} to E_c of the dopant valence electrons and capture from E_c back to E_{sh}. The separate relaxation frequencies imply

that the rate for ionization,$\gamma_{sh\to c}$, is different than the rate for capture,$\gamma_{c\to sh}$. Using detailed balance [29], $\gamma_{sh\to c} n_{sh} = \gamma_{c\to sh} n_c$, where n_{sh} and n_c represent respectively the density of carriers in E_{sh} and E_c, we can infer $\gamma_{c\to sh} > \gamma_{sh\to c}$, since $n_{sh} > n_c$ near freeze out where the MC is dominant. This argument allows us to identify the low frequency loss peak with ionization $\gamma_{sh\to c}$ and the high frequency peak with capture, $\gamma_{c\to sh}$. Intraband transitions such as hopping are not seen because our measurement temperatures are too high.

In the GaAs host, the Bohr radii of the hydrogen-like donor electrons are renormalized upwards by the small effective mass, m_{GaAs} = 0.065 m_e, and the large relative permittivity, ϵ_{GaAs} = 13.5. The resulting magnetic freeze-out brings electrons closer to the donor atoms, thus increasing the Coulomb energy and E_a. The renormalization by the host lattice sharply reduces the fields well below the levels required to see an observable effect for hydrogen atoms in vacuum. Our observed change in E_a with H is in good qualitative agreement in functional form [20] and magnitude [21] with previous experiments on Si-doped GaAs.

The above interpretation suggests that at low T electrons can be frozen out from the conduction band E_c to the impurity band donors as H increases. This capture process explains the H-induced decrease in $N_d(f, T, H)$ at fixed f and T shown in the lower panel of Fig. 2-4. It does not explain however the H-dependence of $V_{bi}(f, T, H)$. Usually, V_{bi} extracted from a M-S analysis is used to calculate Φ_{SBH} from the relation [2], Φ_{SBH}=V_{bi}+$(E_c E_F)/e$. An increase in V_{bi} corresponds by Eq. 2–1 to an increase in W and a corresponding decrease in C_{dep}. Since $E_c - E_F$, which is calculated to be ≈10 meV, is a small correction with negligible H dependence, the measured shift in V_{bi} of 300 meV for a 7T change in H (Fig. 2-3 top panel) implies that there is a comparable shift in Φ_{SBH}. Such a dependence of Φ_{SBH} on H extracted from C measurements is unphysical since, as shown by the schematic in the inset of Fig. 2-2, the capacitance, C_{bond}, arising from bond polarization and the associated dipole layer giving rise to ΦSBH at the

metal-semiconductor interface is in series with the much smaller C_{dep} and hence can be ignored. The expected H independence was checked using IPE measurements [5, 26] on similar samples at various temperatures and fields up to 70 kOe. The intercepts of the linearly extrapolated photocurrent yield on the abscissa of the inset to the top panel of Fig. 2-7 show a small T dependence but no H dependence. Thus the H-induced V_{bi} shift has another origin and the M-S equations must be modified.

2.3.3 Effect of Magnetic Field on the Current-Voltage Characteristics

The above conclusion also applies to the magnetic field dependence of the forward-biased threshold observed in the $I-V$ characteristics. In Fig. 2-1b we show the $I-V$ characteristics at the four indicated temperatures for two values of field, H=0 Oe (solid symbols) and H=70 kOe (open symbols). We note that while the magnetic field has negligible effect on the forward bias threshold at high temperatures (300 K), there is a systematic increase in the field-dependent increment of the forward bias threshold as T is lowered to 20 K. At 20 K the ideality factor is significantly larger than unity, thus indicating that accurate estimates of Φ_{SBH} cannot be obtained due to the presence of additional processes such as generation-recombination, quantum tunneling and thermionic-field emission (subsection 1.3.4). The observed field-induced changes in the low temperature forward biased thresholds are thus more likely attributed to corrections to Φ_{SBH} derived from image-lowering and thermal field emission. The Schottky barrier lowering due to the image forces (section 1.3.4) is given by,

$$\Delta\phi_B = \sqrt{\frac{e^3 V_{bi}(f,T,H) N_D(f,T,H)}{8\pi^2\epsilon_s^3}}, \tag{2–4}$$

and similarly the change in the Schottky barrier height due to the thermionic field emission is,

$$\Delta\phi_B = \left[\frac{9}{4}E_{00}(f,H,T)^2 V_{bi}(f,H,T)\right]^{1/3}, \tag{2–5}$$

where E_{00} is

$$E_{00} = \frac{e\hbar}{2}\left[\frac{N_D(f, H, T)}{\epsilon_s m^*}\right], \tag{2–6}$$

These two processes become important at temperatures much lower than the apparent barrier height and give a correction that decreases when $N_D(f, H, T)$ decreases [1, 30]. Thus with increasing H, the concomitant decrease in $N_D(f, H, T)$ leads to an increase in the *effective* Φ_{SBH} and the forward bias threshold as seen in Fig. 2-1b. However, our calculations show that these corrections are only responsible for ∼10-20 meV increase in barrier height and thus do not explain the large shift in built-in potential seen in Fig. 2-3. We conclude that the interpretation of low temperature $I - V$ curves using traditional thermionic emission theory, which remains an open problem in the literature [1], is unreliable. For these reasons we focus on ac impedance measurements, which identify the frequency magnetic field dependent processes occurring within the depletion region, and the internal photoemission (IPE) measurements, which directly determine Φ_{SBH}.

2.4 Modification of the Abrupt Junction Approximation (AJA)

The M-S relations for C_{dep} are usually derived using the abrupt junction approximation (AJA), phenomenological description, which assumes a constant density N_d of ionized impurities within the depletion region in which $N_d(f, T, H)$=$N_d^0(T)$ is constant for all x within the depletion width (0=x=W) and zero elsewhere. Although the AJA is overly simplistic, it has the well-known advantage that when combined with Poissons equation the relationship between $1/C_{dep}^2$ and reverse bias voltage V_R is linear. This linearity of the Mott-Schottky (M-S) plots is seen in many experiments [1] including ours (Fig. 2-3). The failure of the AJA to include frequency (and field) dependence is an obvious deficiency. Thus, if C_{dep} is frequency (magnetic field) dependent as it is in our experiment (Fig. 2-3), the extracted slopes and intercepts are by necessity also frequency (magnetic field) dependent (Fig. 2-3) and cannot be simply related to the high temperature (fully ionized) values of the built-in potential V_{bi}^0 and ionized impurity density

N_d^0. Our solution to this deficiency, a deficiency which has been recognized in previous work [10, 31, 32] is the introduction of a modification of the AJA as discussed below. As T is lowered, electrons from the conduction band are captured and $N_d^0(T)$ decreases. To incorporate the effects of f and H, we modify the AJA with the expression,

$$N_d(x, f, T, H) = N_d^0 + N_{cap}(f, T, H)\left[\Theta(y-x)\, exp(-x/L) + \alpha\right] + N_{ion}(f, T, H)\, exp(-x/W), \tag{2–7}$$

where N_{cap} and N_{ion} are frequency dependent parameters representing respectively the additional charge (and hence polarization) of the high-frequency capture and low-frequency ionization processes, Θ is the unit step function, L is a characteristic length and y, which obeys the constraint $0 < y < W$, is a cutoff beyond which the exponential contribution to $N_{cap}$is zero. The constant α assures that capture processes can occur for all x while the characteristic length L determines a scale length for the exponential decay of N_{cap} away from the interface. Our modified version of the AJA as expressed by Eq. 2–7, is valid only for x in the range, $0 < x < W$, and thus allows Poissons equation to be solved for the charge distribution and associated capacitance. Overall, Eq. 2–7 represents a phenomenological modification to the charge distribution which includes frequency dependence embedded in the parameters N_{cap} and N_{ion}. Following Bauza [10], who offers a similar expression to account for deep level electronic traps of Ti−W/n−Si Schottky diodes, we solve Poissons equation using Eq. 2–7 and find

$$\frac{1}{C_{dep}^2} = \frac{2\left(V_{bi}^0(T) - eN_{cap}(f, T, H)L^2\left(exp(-y/L)\left(1 + y/L\right)\right)/\epsilon_s + V_R\right)}{e\epsilon_s\left(N_d^0(T) + \alpha N_{cap}(f, T, H) + 2N_{ion}(f, T, H)\right)}, \tag{2–8}$$

Although the phenomenology, when compared with the overly simplified M-S model, becomes considerably more complex with the introduction of five additional unknown parameters (N_{cap}, N_{ion}, L, y, α), our formulation has the distinct advantage that frequency dependence is included and the linearity of the M-S plots at different

frequencies, temperatures and fields is preserved. The understanding gained from this reformulation becomes evident in the redefinition of the extracted slopes and intercepts

$$N_d(f, T, H) = \left(N_d^0(T) + \alpha N_{cap}(f, T, H) + 2N_{ion}(f, T, H)\right), \tag{2–9}$$

$$V_{bi}(f, T, H) = \left(V_{bi}^0(T) - eN_{cap}(f, T, H)L^2\left(exp\left(-y/L\right)\left(1 + y/L\right)\right)/\epsilon_s + V_R\right), \tag{2–10}$$

In the high T limit where all impurities are ionized, $N_{cap} \rightarrow 0$ and $N_{ion} \rightarrow 0$, Eq. 2–8 reduces to the conventional f and H-independent M-S relation,$1/C_{dep}^2(T) = 2\left(V_{bi}^0(T) + V_R\right)/e\epsilon_s N_D^0(T)$ and the Schottky-Mott relation is preserved. With decreasing T, $V_{bi}^0(T)$ (and hence Φ_{SBH}) increases due to temperature variations of the bandgap [9], and the decrease in $N_d^0(T)$ (thermal freezeout) is compensated by increases in N_{cap} and N_{ion}, reflecting the dominance of f- and H-dependent processes.

2.5 Discussion

An intuitive physical understanding of the above equations derives from the fact that N_d is exponentially dependent on the ratio -$E_a(H)/k_B T$. Thus as T decreases, or H increases with a corresponding increase in E_a (Fig. 2-6), N_d^0 decreases from its high-temperature (100% ionization) value, and there is a concomitant increase in the number of transitions between the shallow E_{sh} and conduction E_c bands (arrows in the Fig. 2-3 schematic). At fixed f and H the parameters N_{cap} and N_{ion}, which as modifications to the AJA represent the ionized donors participating in the interband transitions, thus increase with decreasing temperature. However, the relative increase of the quantity in Eq. 2–9 with decreasing temperature is not sufficient to compensate for the decrease in N_d^0, thereby giving rise to a net decrease in $N_d(f, T, H)$ consistent with the decreased capacitance with decreasing temperature. At fixed T, the interband transitions associated with N_{cap} and N_{ion} and shown in Fig. 2-5 decrease with increasing H (field freezeout) and increasing f (polarization cannot follow rapid changes), thus

accounting for the observed decrease in N_d described by Eq. 2–9 and shown in Fig. 2-4. As frequency increases, the response of the low-frequency ionization processes diminishes. However, the response of the higher frequency capture processes, which have the same activation energy and are thus coupled to ionization, does not diminish until the frequency comes into this higher frequency range. The largest decreases in N_d and corresponding decreases in polarization (Fig. 2-5) thus occur in separate frequency ranges where the ionization and capture processes dominate.

We emphasize that Eqs. 2–7 and 2–8 represent a useful phenomenological generalization of the original M-S relations which in turn are based on the over-simplified phenomenological AJA. Importantly, for the purposes of this study, we see from Eqs. 2–8 and 2–10 that the observed V_{bi} dependence on H is a function of the unknown parameter y, which in the limit, $y >> L$, describes capture of carriers in close proximity to the metal-semiconductor interface (x=0) where electrons from the metal are readily available and in the opposite limit, $y << L$, describes capture processes occurring uniformly throughout the depletion width.

Similar arguments apply to the observed increases in V_{bi} shown for T=20 K in Fig. 2-4 and described by Eq. 2–10. The apparent large change of V_{bi} with field does not imply a corresponding change in Φ_{SBH} as some might incorrectly conclude. We attribute all of the field dependence describing our observed magnetodielectric coupling to the magnetic field dependent donor impurity binding energy, $E_a(H)$, which in turn imposes field dependence on N_{cap} and N_{ion}. More explicitly, at fixed magnetic field and low temperature (T =20 K) where freeze-out is important and the corrections N_{cap} and N_{ion} to the AJA are significant, the extrapolated intercept $V_{bi}(f, T, H)$ described by Eq. 2–10 increases as the measurement frequency is swept from 100 Hz to 1 MHz (Fig. 2-4). At low frequencies the dominance of capture and ionization processes leads to a correction to $V_{bi}(T)$. In this low-frequency limit, V_{bi} determined by M-S extrapolations agrees with Φ_{SBH} extracted from IPE measurements (Fig. 2-7). Since IPE

measurements directly measure Φ_{SBH} in the dc limit, it is this limit where both relaxation processes occurring within the depletion width have to be included. We have shown that the AJA approximation alone is not sufficient in predicting Φ_{SBH} and one has to take into account the frequency and field-dependent correction terms associated with the capture/ionization processes between the impurity and valence bands. As frequency increases, V_{bi} also increases to significantly higher values due to the decrease in the correctional terms, N_{cap} and N_{ion}, to $V_{bi}(T)$.

At the highest frequencies, beyond the 1 MHz upper bound of our measurements, N_{cap} and N_{ion} both approach zero, and the well-known AJA form of the Mott-Schottky relation (Eq. 2–1) ensues. In this limit V_{bi} is not a physically meaningful measure of Φ_{SBH}, since as shown in this chapter the overly simplistic AJA does not take into account the frequency and field dependent processes revealed so explicitly in Figs. 2-3 and 2-5. This understanding is relevant for higher frequency applications.

2.6 Summary

In summary, in this chapter we have shown that magnetic freezeout [17] of shallow band carriers is responsible for significant changes in polarization within the depletion width of conventional Au/GaAsSi Schottky barriers. Magnetic freezeout is essentially a bulk effect in which the binding energies of all the Si impurity atoms in the GaAs host are simultaneously increased. Accordingly, bulk-sensitive optical [18, 33] and Hall effect measurements [20, 21] clearly reveal the effects of magnetic freezeout. In this chapter, we have demonstrated an interface effect in which the same field-induced changes in the binding energy of the Si donors redefines the charge distribution and the associated electric field, and hence the polarization (capacitance), in the depletion width of a Schottky barrier. The magnetodielectric coupling is an interface effect that arises from the correlation of magnetic freezeout with interfacial polarization and is thus responsible for the observed large negative magnetocapacitance in a system which does not have any magnetic impurities. Our unequivocal determination of an H-independent Schottky

barrier height together with our identification of thermally-activated interband ionization and capture processes justifies our modification of the AJA to preserve the linearity of the $1/C_{dep}^2$ vs V_R plots (as experimentally observed) and at the same time imposes a dependence of N_d and V_{bi} on f, T and H. Finally, the underlying magnetodielectric coupling not only allows a new experimental technique for the tuning of the dopant carrier density at the same interface by magnetic field, but should also be important for engineering the high frequency (microwave) and magnetic field response of diodes and understanding the behavior of related interfacial structures incorporating DMS and spin-polarized metals.

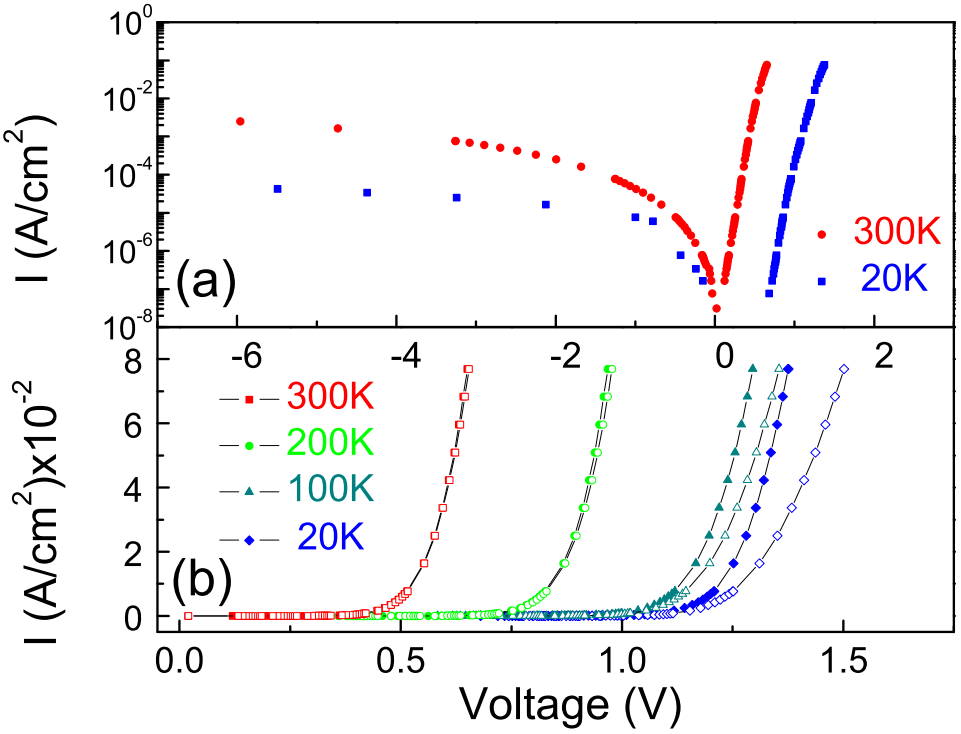

Figure 2-1. Current-voltage characteristics show a temperature and field dependent forward bias threshold. The top panel shows the rectifying (diode) characteristics on a semi logarithmic current-voltage scale for forward (+) and reverse (-) bias voltages at 300 K (red circles) and 20 K (blue squares). The bottom panel shows on a linear current-voltage scale the forward bias onsets of conduction at the indicated temperatures for H = 0 (closed symbols) and H=70 kOe (open symbols)

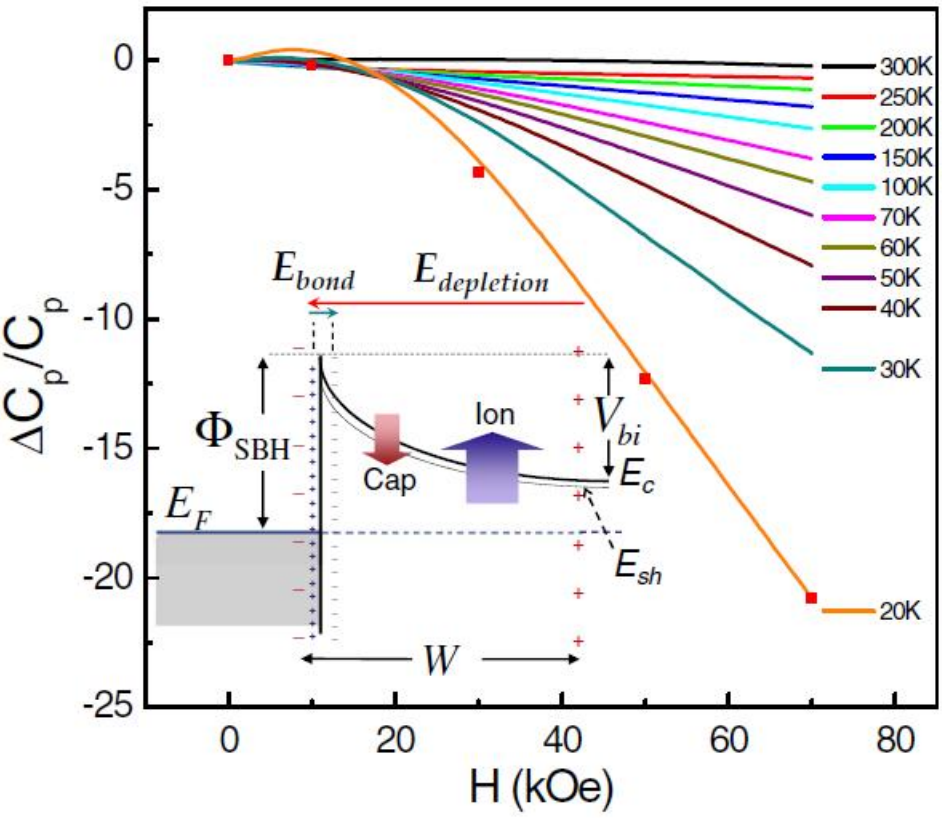

Figure 2-2. Capacitance of a Au/GaAs：Si Schottky junction decreases with increasing applied magnetic field H. The relative change in capacitance $\Delta C_{dep}/C_{dep}$ becomes increasingly more negative with increasing field. The solid curves represent data taken at the decreasing temperatures (top to bottom) indicated in the legend. The solid orange squares associated with the 20 K isotherm are calculated using M-S relation with the M-S parameters extracted from $1/C^2$ versus voltage plots. Inset, Schematic of band bending with parameters defined in the text. Capture processes (red arrow) tend to dominate near the interface whereas ionization processes are distributed over the depletion width W. The large capacitance associated with a high density of polarized bonds at the interface is in series with the much smaller depletion capacitance.

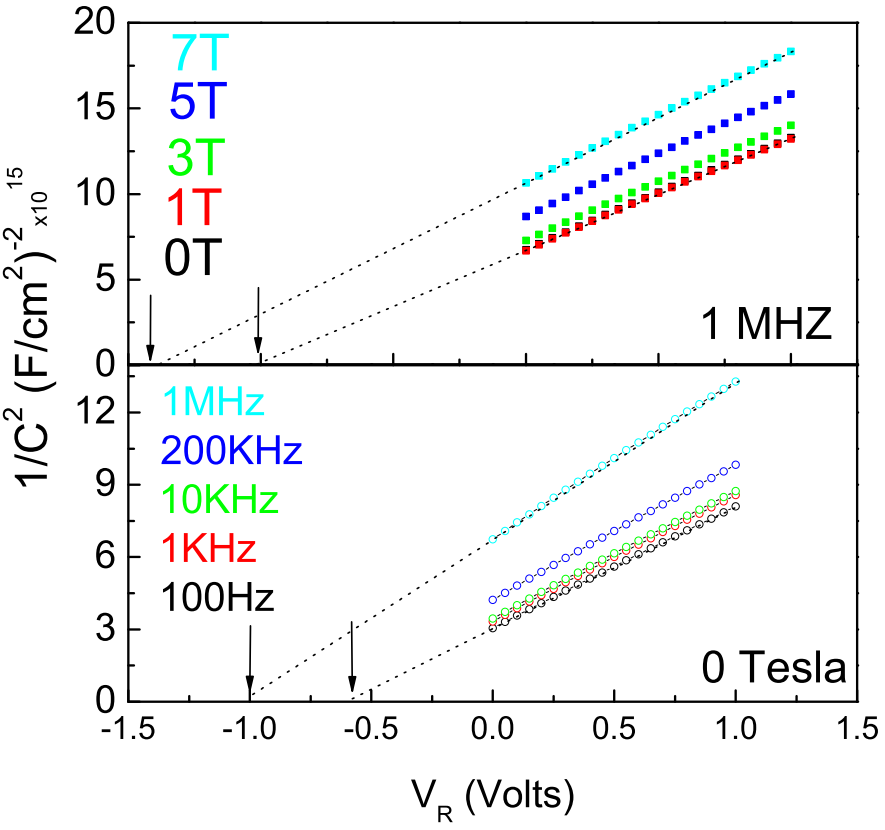

Figure 2-3. Linearity of $1/C^2$ vs V_R plots enable determination of M-S parameters. Data at 20K are shown at 1MHz for the indicated fields H (top panel) and at H=0 for the indicated frequencies f (bottom panel). The vertical arrows mark selected extrapolated intercepts with the abscissa corresponding to the built-in potential $V_{bi}(f, H)$ at 20K.

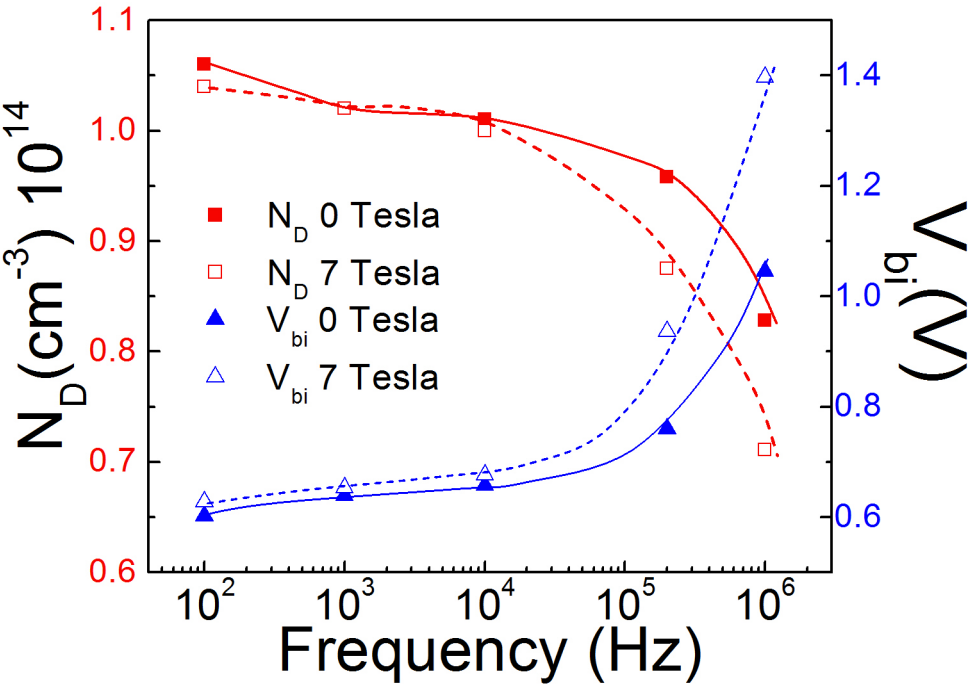

Figure 2-4. The frequency dependence of V_{bi} (right hand axis) for H=0 (70 kOe) for solid (open) triangles and the frequency dependence of N_D (left hand axis, see text) for H = 0 (70 kOe) for solid (open) squares.

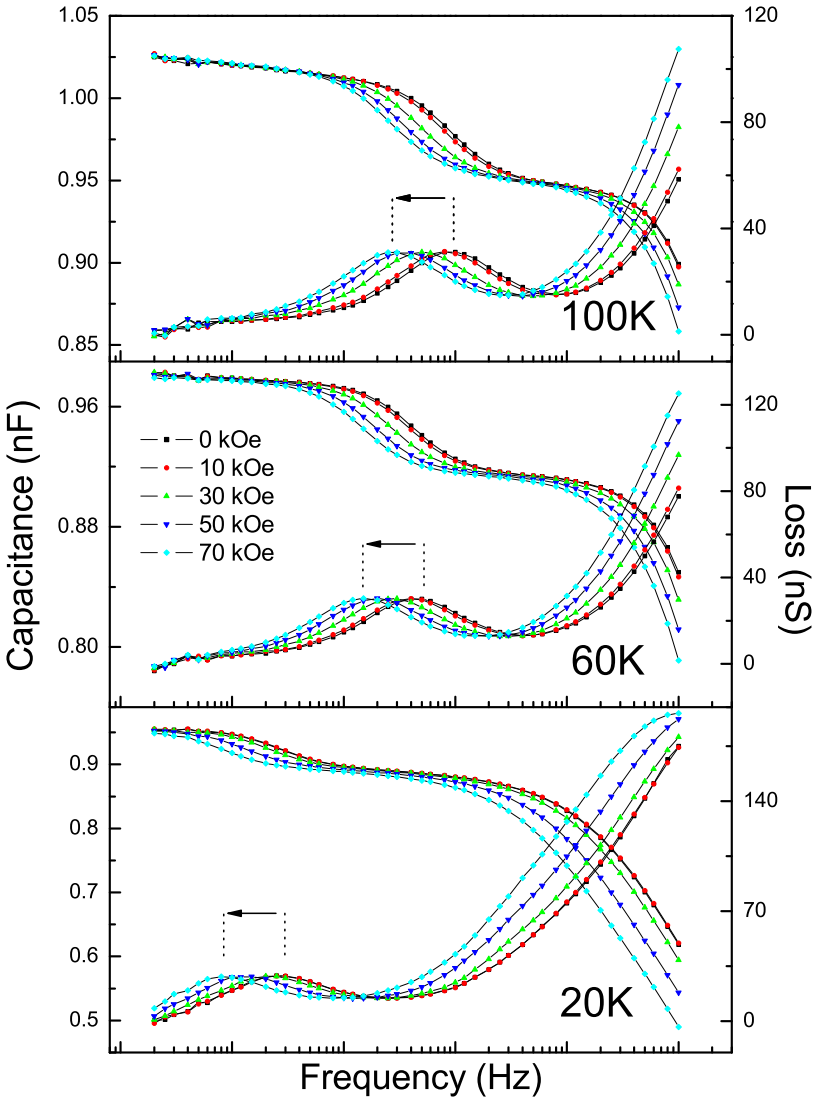

Figure 2-5. Temperature and field dependent frequency dispersion of the capacitance reveals two separate loss processes. In the three panels the frequency-dependent capacitance (left hand axis, top curves) and loss (right hand axis, bottom curves) are shown as a function of frequency for each of the three indicated temperatures. Each group of curves contains data for the five different fields indicated in the legend of the middle panel. For fixed fields the loss peaks shift to lower frequency as the temperature is reduced. The horizontal arrow in each panel marks the isothermal shift to lower frequency of the low-frequency loss peak (ionization) as the field is increased from 0 to 70 kOe.

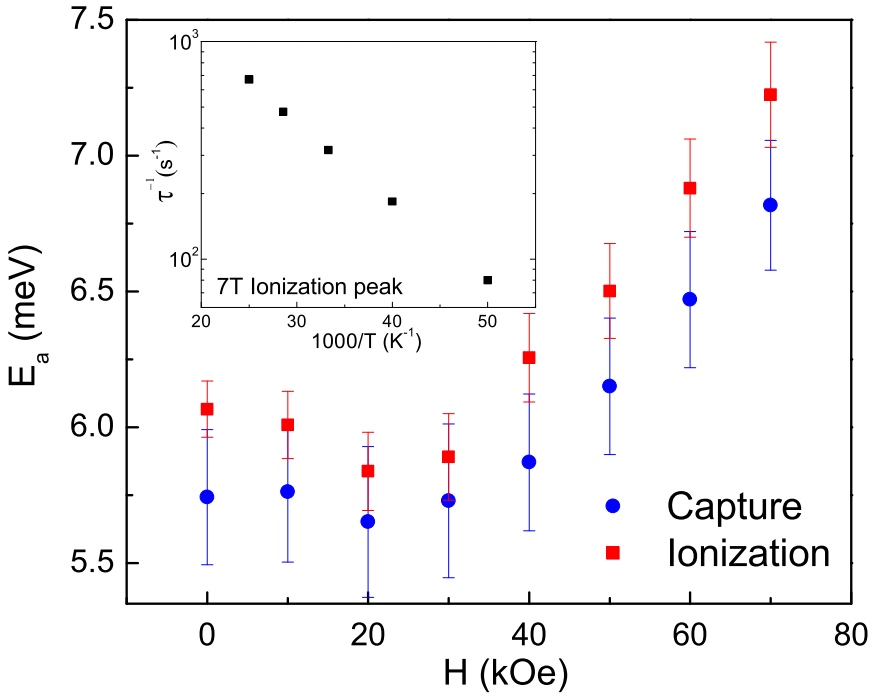

Figure 2-6. Activated binding energy E_a of Si impurity donated electrons increases with increasing field. The dependence of E_a on H is shown for both the low frequency (red squares, ionization) and high frequency (blue circles, capture) loss peaks. Each point is determined by fixing the field and plotting the frequencies of the loss peaks versus $1/T$ on a semilogarithmic plot. The slopes of the resulting linear plots (inset for H = 70 kOe) determine the H-dependent binding energies.

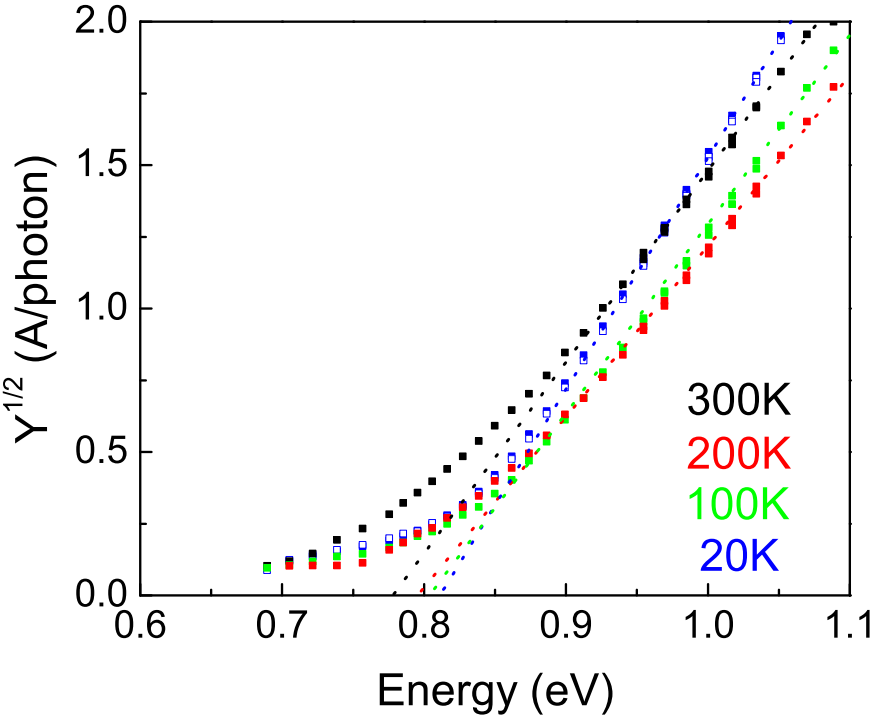

Figure 2-7. IPE data in which H-independent extrapolations (dotted lines) to the abscissa at the indicated temperatures imply that there is no dependence of the Schottky barrier height on *H* up to 70 kOe.

CHAPTER 3
MULTI-LAYER-GRAPHENE (MLG) BASED SCHOTTKY DIODES FORMED ON SI, GAAS, 4H-SIC AND GAN SUBSTRATES

3.1 Introduction

The Schottky barriers formed on various semiconductors are interesting due to their potential technological application as high electron mobility transistors (HEMTs)and metal-semiconductor field effect transistors (MESFETs). In MESFETs, the quality and efficiency of the Schottky diodes play a major role. When reverse or forward bias is applied across the interface, Schottky barrier interface, the depletion width is driven to either depletion or accumulation and the 'on' and 'off' state is achieved. The depletion capacitance at the interface is much smaller comparing to that of $p-n$ junctions and Schottky diodes yield faster response and are typically used in radio frequency (RF) applications. The same effect with slower responses can be achieved in metal-oxide-semiconductor field effect transistor (MOSFET) geometries. The MOSFET device geometry is specifically convenient for semiconductors such as Si where natural oxide (SiOx) exists and the 'on' and 'off' state is achieved by field effect gating across the metal-oxide-semiconductor (MOS) and depleting or accumulating the semiconductor. However, the MOSFET geometry becomes problematic for most semiconductors where there is no established oxide exists (such as GaAs, SiC and GaN). In such cases, Schottky diodes and the MESFET geometry is preferred.

Moreover, Metal-semiconductor contacts are ubiquitous in semiconductor technology not only because they are unavoidable, but also because the associated (Schottky) barriers to electronic transport across the metal-semiconductor interfaces can be tuned by different choice of materials and processing techniques [1]. The characteristic of a Schottky barrier is its rectifying characteristic; the Schottky barrier essentially acts like a diode with large currents flowing for forward bias and significantly smaller currents flowing for reverse bias [2] as displayed for Au/GaAs Schottky junctions in Fig. 2-1 and in Chapter 2. If low resistance and ohmic(linear) $I-V$ characteristics are

desired (section 1.4), then materials and/or processing techniques such as rapid thermal annealing, are chosen to assure that the Schottky barrier height (SBH) ϕ_B is small compared to room temperature ($\phi_B << k_B T$). On the other hand, if good Schottky diodes with barrier heights much higher than room temperature are desired, metals roughly satisfying the Schottky-Mott relation (Eq. 1–12) are placed on different types of semiconductors. Schottky barriers are generally recognized as metal-semiconductor junctions, however semi metal rather than metal electrodes can also be used. Previously, epitaxial ErAs/InAlGaAs diodes fabricated by molecular beam epitaxy (MBE) have barrier heights that can be tuned over a wide range by adjusting composition and doping [34].

Carbon based materials have been the center of attention for more than 5 decades in different forms as 0D fullerenes, 1D carbon nanotubes, 2D graphene and 3D graphite. Even though, integration of carbon into existing conventional devices faces numerous challenges, their unique physical properties make them a good candidate for future electronics applications [35]. Specifically graphene; two dimensional single layer of sp^2 bonded carbon atoms and semi-metal graphite, many layer graphene sheets with Bernal stacking, are of particular interest due to their exotic band-structure, excellent conductivity, high mobility and stability. Other than their fruitful properties, graphite and graphene display very large sensitivity to dopants: Graphite and graphene are clean materials with very low carrier densities with 10^{-4} free electrons per carbon atom(Chapter 5. Therefore, any charge transfer taking place in between the dopant and the carbon host material results in large changes in the number of free electrons per carbon. Due to large charge transfer and the corresponding large increase/decrease in number of free electrons per carbon there is also a large change in the Fermi level of the system. If such barrier are formed in between various semiconductors and graphene or graphite, such devices can be used as potential gas detectors and the Schottky barrier formed across the M-S interface can be tuned (for MESFET applications - Chapter 4)

by selectively doping the carbon based material. These advantages of graphite and graphene together with their thermal stability make graphite-graphene/ semiconductor junctions particularly interesting.

This chapter addresses the use of multi- layer- graphene (MLG) exfoliated from highly oriented pyrolytic graphite (HOPG) and natural graphite as the semi metal in semi metal/semiconductor Schottky barriers. We demonstrate unexpectedly high-quality rectifying characteristics on four different n-type semiconductors each of which is uniquely suited to specific applications: namely Si, with its robust oxide, to field gated transistors, GaAs, with its direct band gap, to spintronic and optical applications and SiC and GaN, with its high thermal conductivity and breakdown strength, to high power/frequency devices. Advantageously the multi- layer- graphene contact are robustly impervious to diffusion of impurity atoms [36] and can be placed on the semiconductor at room temperature. The relatively weak bonding associated with the Van der Waals interaction, causes minimal disturbance at the semiconductor surface. Since the Schottky barrier height, ϕ_B, is related to an interfacial dipole layer associated with bond polarization [1], we infer that barrier properties are determined primarily by the outermost layer of the multi- layer- graphene contact which is a single layer graphene (SLG) sheet. Accordingly, our results anticipate similar phenomenology using two-dimensional (2D) graphene rather than multi- layer- graphene. Other examples demonstrating SLG-like properties in graphite include ARPES evidence for the precursor influence of K-point Dirac fermions [37] and a pronounced temperature-dependent upturn in the temperature range, 300 K $< T <$ 900 K, in the in-plane resistivity (ρ_{ab}) of HOPG due to intervalley scattering of carriers by SLG-like optical phonons and thus describable as a stack of graphene bilayers in which next-to-nearest neighbor couplings can be ignored [38]. The associated pronounced temperature-dependent upturn in the in-plane resistivity (ρ_{ab}) in the 300 K $< T <$ 900 K temperature range where the

next-to-nearest neighbor couplings can be ignored confirms this picture that at these high temperatures graphite can be described as a stack of graphene bilayers [38].

3.2 Experimental Details

We have used commercially available *n*-type Si and GaAs with 1×10^{15} cm^{-3} phosphorus (P) and 3×10^{16} cm^{-3} silicon (Si) doping densities respectively. The 4H-SiC wafers are layered, comprising a 5 μm-thick layer of doped epilayer (1×10^{16}cm^{-3}) deposited onto an insulating 4H-SiC substrate. GaN samples were grown on sapphire substrates in molecular beam epitaxy system and were doped by Si doping densities of (1×10^{16}cm^{-3}). The Si:P (GaAs:Si) substrates are thoroughly cleaned to remove any native oxide and/or contaminants.

Ohmic contacts are made on the Si:P, GaAs:Si, 4H-SiC:N and GaN:Si substrates using existing ohmic contact recipes [3, 39–41]. These ohmic recipes assure low resistance linear I-V's over the temperature ranges measured. The I-V and C-V measurements are performed respectively using dc current-source/voltage-measure instruments (Keithley 220/182) and an Agilent 4284A capacitance bridge. The Schottky barrier height across the multi- layer- graphene / semiconductor junctions is measured by the methods discussed in subsections 1.3.5.1 and 1.3.5.2/

The multi- layer- graphene contacts are deposited to the semiconductors using three related techniques. In the first method, multi- layer- graphene contacts are mechanically exfoliated from natural graphite or HOPG samples using thermal release tape. In this method, Nitto Denko Revalpha thermal release tape (Part Number 3193-MS) was placed on graphite with 3N/mm^2 pressure for 5 minutes in a chamber kept under 10^{-3} torr. Pressure applied on the thermal release tape/graphite stacking allows us to increase the bonding and eliminates the air pockets at the tape-graphite interface. The efficiency of the thermal release tape increases if the pressure is applied under mediocre vacuum conditions. After this step, the thermal release tape is exfoliated from graphite, leaving multi- layer- graphene / thermal release tape stacking. Desired

multi- layer- graphene thickness can be achieved by consecutive thermal release tape exfoliation. In the last step, multi- layer- graphene / thermal release tape stacking placed on top of various semiconductors by applying similar pressures under the vacuum. Semiconductor / multi- layer- graphene / thermal release tape stacking is annealed to 125C, at this temperature thermal release tape loses its adhesion to multi- layer- graphene contact drastically, leaving multi- layer- graphene deposited on semiconductor substrate. This method can be tailored for specific contact sizes, thicknesses. In the second method (cleavage technique), either HOPG powder/flakes are collected by cutting 0.5° FWHM bulk HOPG using a diamond impregranated wire and allowing the flakes to fall onto the semiconductor substrate or by mechanical exfoliation method [42]. Cleaved HOPG flakes made a contact to semiconductor surface by Van der Waals adherence and occasionally, relatively large area ($\sim$ 0.5 mm^2 multi- layer- graphene flakes flatten out with strong adherence to the substrate due to Van der Waals attraction. In the last method (HOPG paint method), graphite powder/flakes are sonicated in residue-free 2-butoxyethyl acetate and octyl acetate and the painted contacts allowed to air dry. All of these *soft-landing* techniques give similar results when the applied currents are normalized with respect to contact area. Physical characteristics measured at the multi- layer- graphene / semiconductor junctions are also tested by using a relatively large ($\sim$1 mm^2) HOPG or pristine natural graphite piece and gently pressing onto the substrate (spring loaded graphite method).

3.3 Formation of Schottky Diodes at the Multi-Layer-Graphene / Si Interface

Fig. 3-1 shows the typical measured current density vs. voltage (J-V) room - temperature characteristics of HOPG paint and multi- layer- graphene contacts on n-type Si substrates placed by the methods discussed in the previous section. These data represent a subset of more than 10 different samples, all giving similar results independent of the method of application of the multi- layer- graphene electrode. As seen from Fig. 3-1, multi- layer- graphene based junctions show good rectification at

room temperature. For all of the junctions the rectification is preserved down to 20K, below which the quality of the ohmic contacts becomes problematic.

When electron transport across the metal-semiconductor interface is dominated by thermionic emission, the semilogarithmic J-V curves usually display a linear portion in the forward bias region from which reliable estimates of the barrier height ϕ_B and the ideality constant, η, can be extracted. The extraction of those parameters is based on the Richardson equation as discussed in subsection 1.3.5.1,

$$I = I_s(T)[\exp(qV/\eta k_B T) - 1], \tag{3–1}$$

where $I_s = AA^* T^2 \exp(-q\phi_B/k_B T)$ is the saturation current, $q\phi_B$ is the SBH, A^* is Richardson constant, T is the absolute temperature, and V is the voltage across the ohmic and multi- layer- graphene contacts. At room temperature the exponential in Eq. 3–1 dominates at forward voltages greater than $3k_B T/q \sim 0.1$ V. As shown in Fig 3-1b, the multi- layer- graphene/Si junctions displayed 2-3 decades of linearity in the semilogarithmic J-V curve. Linearity in a wide voltage range implies that the dominant transport process is thermionic emission in accord with Eq. 3–1. At low and the high applied voltages, $J - V$ plots strongly deviate from linearity. The deviation from linearity can be attributed to the existence non-ideal effects discussed in section 1.3.4 such as such as space-charge limited emission at low voltages and series resistance effects at higher voltages.

Extraction of an accurate value for ϕ_B from Eq. 3–1 requires the electrically active area A. However, randomly distributed multi- layer- graphene pieces/flakes make contact at some portions of the semiconducting substrate while they are not in physical contact with the other portions. Therefore, the contact area determined under the microscope does not necessarily correspond to the *effective active area* and the electrical active area,A, remains unknown. When semilogarithmic isothermal I-V curves are plotted, rather than the J-V curves shown in Fig. 3-1, extrapolation from the linear regions to

$V = 0$ to allows one to determine the saturation current values at specific temperature ($I_s(T)$). Analysis is facilitated by writing the equation for $I_s(T)$ in the form (Eq. 1–43),

$$\ln(I_s(T)/T^2) = \ln(AA^*) - (q\Phi_{SBH}/k_B T), \tag{3–2}$$

where the unknowns A and Φ_{SBH} now appear in separate terms.

Typical Richardson activation energy plots of $\ln(I_s(T)/T^2)$ versus T^{-1} for multi- layer- graphene/Si junctions are shown in Fig. 3-1 over the temperature range 250-330K. The effective SBHs for Si are calculated from the slopes around 0.40(1) eV (Table 3-1) with ideality factors (η) spanning from 1.1 to 2.0 for all samples. Values of η greater than unity are generally attributed to bias dependent SBHs, generation - recombination, thermally assisted tunneling, and image force lowering [1]. The large η values of the Schottky diodes and their effects on the measurement of barrier height from $J-V$ characteristics have been addressed in the literature [43] and will be analyzed in section 3.7.

Another method to measure the Schottky barrier height is known as $C - V$ measurement technique as discussed in sec. 1.3.5.2. As shown in Fig. 3-3, capacitance at the metal-semiconductor junction (depletion width) is measured using the capacitance bridge and capacitance(1 kHz)-voltage (C-V) measurements plotted in the form $1/C^2$ vs. V_R. Here, V_R stands for the reverse bias voltage. The observed linearity in the $C - V$ measurements suggests that gap states are absent and that the surface density of states is small. Linear extrapolation (dotted lines) to the intercept with the absiccsa identifies the built-in potential, V_{bi}, which is related to Φ_{SBH} via the expression, $\phi_B = V_{bi} + (E_c - E_F)$, where E_c is the conduction band edge and E_F the Fermi energy. After the built-in potential is extracted out, the dopant densities of each semiconductor can be calculated from the slopes as identified in Eq. 1–44. The values for Φ_{SBH} and N_D extracted from the linear dependences shown in Fig. 3-3 are listed in Table 3-1. The extracted values for N_D are in good agreement with Hall data, while the values for Φ_{SBH}

are observed to be higher than the values extracted from I-V measurements. These discrepancies will be discussed in section 3.7.

3.4 Formation of Schottky Diodes at the Multi-Layer-Graphene/GaAs Interface

GaAs is a III/V compound semiconductor with the band gap value of 1.43eV. Today, GaAs substrates and wafers are mainly used in manufacturing microwave integrated circuits and high power devices, solar cells, laser and infrared light emitting diodes. Its higher mobility ($\sim$8500cm$^2/(V.s)$) comparing to that of Si ($\sim$1500cm$^2/(V.s)$), makes GaAs very suitable for high frequency device applications working at frequencies much higher than 500 GHz. Moreover, GaAs displays four orders of magnitude less intrinsic carrier density (Eq. 1–10) comparing to Si. Due to its small intrinsic carrier density at room temperature, its intrinsic carrier density doesn't exceed the extrinsic carrier density and their electrical properties is still controlled externally (via doping). This property allows GaAs based devices to work at temperatures much higher than the operating temperatures of Si based devices. Another advantage of GaAs over Si is considered to be its breakdown voltage values. GaAs displays breakdown voltage values that are much higher than that of Si and is suitable for radar systems, satellite communication systems. Lastly, its direct band gap allows better light emitting characteristics compared to indirect band gap Si which also has poor emission properties for solar cell applications.

On the other hand, the absence of stable, established dielectric on GaAs is one of the major disadvantage over cheap, easy to process silicon based technology. In such case, the dielectric has to be grown by ebeam or sputtering systems (rather than thermally grown SiOx on Si wafer) and these methods induce surface states at the interface. Therefore, the semiconductor can not be easily driven into the depletion and accumulation by applying an electrical field across the metal-oxide-semiconductor interface and the MOSFET device geometry becomes unpractical. However, the accumulation and depletion at the interface can also be achieved by applying bias to

the Schottky barriers formed on the GaAs substrate in the forward and the reverse directions and for that reason Schottky barrier junctions are crucial for semiconductors without natural oxide and the MOSFET device geometry can be replaced by MESFET (metal-semiconductor field effect transistor).

In Fig. 3-4, current density vs. voltage (J-V) characteristics of HOPG paint and multi- layer- graphene contacts formed on n-type GaAs substrates are plotted at room temperature . Reproducibility of the results has been checked on more than 20 samples with various multi- layer- graphene contact deposition techniques as mentioned above. In Fig. 3-4, multi- layer- graphene based junctions show good rectification at room temperature with breakdown voltage higher than that of Si/ multi- layer- graphene junctions. For all of the junctions the rectification is preserved down to 20 K, below which the quality of the ohmic contacts becomes problematic.

As shown in Fig 3-4b, the multi- layer- graphene/GaAs junctions displayed 4-5 decades of linearity in the semilogarithmic $J - V$ curves. Linearity in a wide voltage range implies that the dominant transport process is thermionic emission and is described by Eq. 3–1. As discussed the in previous section, in principle the Schottky barrier height can be extracted out by using Eq. 3–1 when the active contact area is known. Following similar arguments and procedure (Eq. 3–2), the effective SBHs are calculated from the slopes to be 0.50(1) eV (Table 3-1) with ideality factors (η) spanning from 1.1 to 2.0 for all samples in the 250 K-330 K range.

The SBH values extracted from the activation energy plots agree roughly with the values extracted out from the capacitance measurements as shown in Fig. 3-6. As shown in Fig. 3-6, the capacitance-voltage (C-V) measurements plotted in the form $1/C^2$ vs. V_R at room temperature and 1KHz operating frequencies dislayed linearity in the overall measured voltage range. Linear extrapolation (dotted lines) to the intercept with the absiccsa identifies the built-in potential, V_{bi} as described in Chapter 2. The extracted Schottky barrier height from $C - V$ measurements, $\phi_B = V_{bi} + (E_c - E_F)$, are

typically around 0.76eV (Table 3-1). The discrepancies in between the Schottky barrier heights determined from $I-V$ and $C-V$ measurements will be discussed in section 3.7.

3.5 Formation of Schottky Diodes at the Multi-Layer-Graphene/4H-SiC

Silicon carbide (SiC) is a indirect band-gap semiconductor with band band values ranging from 2.3 eV up to 3.2 eV depending on the crystal structure. SiC is rarely found in the nature and therefore is mostly grown under laboratory conditions. SiC crystals exist in more than 250 crystallite forms but the most commonly known ones are in the cubic form (3C-SiC), hexagonal form (4H-SiC and 6H-SiC) with band gap values of 2.3 eV, 3.2 eV and 3.00 eV respectively. SiC crystals are generally n-doped either with phosphorus or nitrogen. Wide band gap SiC displays very small intrinsic carrier densities in the order of 10^{-6} cm^{-3} which is almost 14-16 decades smaller comparing to that of Si. The small intrinsic carrier density in SiC, is especially advantageous at temperatures exceeding 500 K where the silicon intrinsic carriers density exceed the typical extrinsic carrier concentration. At those elevated tempetures, the intrinsic carrier density of the material increases (Eq. 1–10) rapidly with temperature and might exceed the extrinsic doping density (as in silicon). At temperatures where the intrinsic carrier density is higher or comparable to extrinsic doping density, the device can no longer operate controllably and thus materials with lower intrinsic carrier density are desired. The low intrinsic carrier density of SiC extends the temperature range where the intrinsic carrier density is significantly less than the extrinsic carrier density and this makes SiC desired material for high temperature and high power applications.

Another advantage of SiC is high breakdown voltages. SiC possess breakdown voltage that is significantly higher than the breakdown voltage of Si and GaAs. On the other hand, at high fields SiC starts to breakdown associated to existence of stacking faults and formation of micropipes in the crystal and hence and has less breakdown voltage comparing to GaN. Lastly, even though it's impressive light emitting diode (LED) history, indirect band gap SiC emits more than decade less intense light comparing to

that of direct band gap GaN but is considered to be much more efficient comparing to the Si based LEDs. Overall, SiC stands somewhere in between Si, GaAs and GaN as far as breakdown voltage and the potential LED applications goes.

Overall, SiC is used for Schottky diodes, MESFET devices, ultrafast device components and high temperature bistable switches, thyristors, but the MOSFET geometry is not preferred due to lack of natural oxide formed on SiC substrates.

3.5.1 Schottky Barrier Characteristics of Multi-Layer-Graphene / 4H-SiC Schottky Diodes from 250 K up to 330 K

In Fig. 3-7, room temperature current density versus voltage (J-V) characteristics measured of the multi- layer- graphene contacts on the n-type 4H-SiC substrates are displayed. The data shown in Fig. 3-7 has been reproduced on more than 10 different samples made by different techniques such as spring loaded HOPG, HOPG paint and micromechanical exfoliation. Schottky diodes formed on the 4H-SiC shows good forward and reverse bias characteristics with superior reverse breakdown characteristics on the order of $\sim$80-100 V (Fig. 3-7). The measured J-V characteristics showed high rectification down to 20-30 K where the ohmic contacts start to fail and/or series resistance becomes too high and begins to compromise the rectifying behavior. At higher temperatures, $T>$200 K, the multi- layer- graphene/4H-SiC junctions displayed 4-5 decades of linearity in the semilogarithmic J-V curves (Fig 3-7b).

When there is a wide range of linearity in the measured $J-V$ characteristics, the Schottky barrier height can be extracted out by using Eq. 3–1 on the condition that the active contact area is known. When the active contact area is not precisely known, the activation energy procedure given by Eq. 3–2 can be followed. However, activation plots did not yield a linear dependence and the Schottky barrier height and the ideality factors would not be determined from this approach. Under the assumption that the contact area is known for SiC, and use of the conventional thermionic emission theory (Eqs. 1–39 and 1–40) we find that the Schottky barrier height formed at the multi- layer-

graphene/semiconductor (SiC) interface is around 1.14 eV and the ideality ranges from 1.1 to 2.0 in the 250 K-330 K range for all samples measured in this chapter.

Even though the SBH extracted from $J-V$ measurements is around 1.15 eV, the Schottky barrier height extracted from $C-V$ measurements is measured around 1.80 eV (Fig. 3-8). These values differ by upto 50% and and results and discrepancies will be discussed in section 3.7.

3.5.2 Schottky Barrier Characteristics of Multi-Layer-Graphene / 4H-SiC Schottky Diodes from 300 K upto 1100 K

SiC substrates are generally used for high temperature electronic devices, due to its thermal stability, high thermal conductivity, and the low intrinsic carrier concentration, which is almost 14 decades less that than in silicon and moreover the absence of conventional dielectric (insulator) on SiC forces one to tune the 'on' and 'off' state by inducing electric field at the metal-semiconductor interface. Therefore, high temperature physical properties of the Schottky barriers formed on SiC and ohmic contact formation are scientifically and technologically interesting. Current research in the literature focuses on the use of different metals such as Ni, Al, Ti as metal electrode [44]. However, those metals are known to diffuse in the SiC material and therefore lead to a significant reduction in the Schottky barrier height upon annealing. However, individual layers of graphite, graphene, consists of sp^2 hybritized carbon atoms that are tightly bonded with coupling parameter which is order of $\sim$3.0 eV and is resistant to heat and is not expected to diffuse inside the material. The stability of graphene and multi-layer- graphene and the absence of diffusion inside the SiC is very suitable for high temperature applications.

In the previous section, the Schottky barrier formation at the multi- layer- graphene and 4H-SiC interface as been displayed by $C-V$ and $J-V$ measurement techniques. In this section, we will focus on the Schottky barrier characteristics of multi -layer -graphene / 4H-SiC junctions at temperatures from 300 K up to 1100K. Using multi-

layer- graphene as a metal is specifically interesting because: (1) the carbon atoms in the multi- layer- graphene crystal are tightly bonded to each other via planar sp^2 hybridization and are not expected to easily diffuse into SiC crystal and form ohmic contact. Most of the ohmic contact recipes on SiC involves use of metal electrodes that form different alloys with the SiC when annealed up to higher temperatures [44]. However, carbon atoms in the graphite or graphene are very tightly bonded to each other and known to be one of the strongest material. Due to intraplanar bonding structure, carbon atoms are not expected to diffuse into the SiC crystal. Graphite displays interesting graphene like properties at temperatures much higher than 300 K [38] (Chapter 6) and offer an interesting system. At those elevated temperatures, the coupling in between the adjacent graphene layers becomes negligible comparing to the nearest neighbor coupling parameter γ_0 as well as γ_1 and graphite starts responding as bi-layer graphene. In this limit, the multi- layer- graphene contact serves as bi-layer graphene deposited on SiC substrate.

All the measurements presented in this section are performed in a homemade high vacuum transport measurement system with 4 terminal contact measurement capabilities from room temperature upto 1500 K, under any gas ambient or under high vacuum from 10^{-4} - 10^{-7} Torr. The temperature of the device is measured independently by an integrated oven thermocouple and K-type thermocouple placed as close as 1 mm proximity to the sample. Each data point is taken after reaching the thermal equilibrium and waiting for an additional 10 minutes. Macroscopic contacts to the samples have been made by using a high temperature silver (or graphite paint contacts) and a platinum wire. $I - V$ measurements are performed by a Keithley 2400 current-voltage source meter.

Electric transport across the multi- layer- graphene/4H-SiC samples is plotted in linear (Fig. 3-9), semilogarithmic (Fig. 3-10) and in the forward bias direction in the semilogarithmic form (Fig. 3-11). Actual measurements took place up to 1300 K, but

the data are plotted only up to 900 K for visual purposes. As seen from Fig. 3-9, the Schottky barrier preserves its good rectification up to 700K. At temperatures above 700 K, the reverse bias current (reverse saturation current density) starts to increase rapidly and become leakier. Eventually, around 900 K, the junction starts to irreversibly lose its recfitication properties significantly and displays linear $I - V$ characteristics after 1100 K. The breakdown in the reverse bias characteristics becomes more apperant when the current-voltage is plotted in semilogarithmic form as in Fig. 3-10. The increase in the reverse bias saturation current can be attributed to the leakage current from metal to semiconductor associated with the excitation of electrons over the Schottky barrier height. More specifically, in the absence of image force lowering and other non-ideal effects (section1.3.4), the reverse bias current is expected to be saturated to a value called a saturated current density. This current is expressed as,

$$J_s = A^* T^2 exp\left(\frac{-e\Phi_{SBH}}{kT}\right), \tag{3–3}$$

Following from Eq. 3–3, for increasing temperatures the value of the J_s increases as observed in Fig. 3-10 and eventually becomes conductive.

In the forward bias, studied diodes display good linear portions in their semilogarithmic I-V curves (Fig. 3-11). As the temperature increases, the total current in the forward bias increases and is consistent with the increase in total number of electrons over coming the barrier height due to their increased thermal energies.

As a summary, the multi- layer- graphene/4H-SiC Schottky diodes display good rectification up to 900 K however above 1100 K the I-V characteristics completely become irreversibly ohmic/linear. The linearity in the $I - V$ characteristic is preserved after the system is cooled down to room temperature. Following the annealing procedure, the $I - V$ characteristics are measured over a week period at room temperature and the contacts remained ohmic. The transition from rectification to

ohmic contact formation might be understood by examining a typical ohmic contact formation using Ni as a metal electrode on SiC.

The nickel metal electrodes on SiC have attracted a lot of interest due to their low contact resistivity. On the other hand, the ohmic contact formation at the Ni/SiC interface still remains controversial. Previously in the literature, the ohmic contact formation on Ni/SiC junctions is mostly attributed to the formation of nickel silicides (Ni_2Si) at the Ni and SiC interface. However, nickel silicides form at the Ni and SiC interface as determined from the x-ray diffraction at 600 C. At these temperatures, Ni metal contacts are leaky and non-ohmic and the temperature is not enough to form ohmic contacts on SiC. Traditionally, Ni contacts form an ohmic contact when the temperature is ramped up to 900 C with nitrogen flowing gas, which is much higher than the temperature required to form nickel silicides. This implies that the nickel silicides might not be the determining factor to form an ohmic contact at the interface [44]. More recently, a full detailed surface depth profiling analysis has been conducted on Ni/SiC at different annealing temperatures and it has been found that [44] nickel atoms do not diffuse inside the SiC but instead Si atoms diffuse out to form nickel silicides at 600 C at which the contact is still non-ohmic. Upon further annealing, the carbon atoms start to diffuse out through the nickel and nickel silicide layers and accumulate at the surface creating a graphitic layer at the surface and carbon vacancy buried under the nickel silicide layer. The formation of carbon vacancies is crucial since the carbon vacancy sites act as electron donors and contribute to the transport of electrons across the Ni/SiC junction thus reducing the barrier height [44].

On the other hand, Schottky diode to ohmic contact transition at the multi- layer-graphene /SiC junction takes place around 1100 K (800 C-900 C) relatively close to the ohmic contact formation at the with nickel/SiC junctions. Here the deposited graphite-graphene layer at the interface might act as a seeding layer at the outermost layer of SiC and upon annealing carbon atoms bound to silicon inside the SiC crystal

might be diffusing out to form graphitic layer at the graphene/SiC interface, creating carbon vacancies buried under the multi- layer- graphene. As pointed out in the previous paragraph, carbon vacancies can act as electron donors and therefore reduce the barrier height eventually becoming a junction with barrier height much smaller than the thermal energy of the electrons (an ohmic contact).

3.6 Formation of Schottky Diodes at the Multi-Layer-Graphene/GaN Interfaces

Gallium nitride (GaN) is a binary III/V direct band gap compound semiconductor with 3.4 eV band gap values. It has wurtzite structure and is known to be a very stable material. It's large band gap, stability at high electric fields (high breakdown voltage) and extremely low intrinsic carrier density of electrons make GaN an ideal material for optoelectronic devices, HEMTs, laser diodes, detectors and high temperature, high power devices. Most of those applications require formation of Schottky barriers on GaN substrates and rely on proper metal choice to form Schottky barriers with low forward bias trashhold and high reverse breakdown voltage as well as durability with respect to temperature.

However, in the literature most of the metalizations on GaN require sputter deposition which creates surface states and surface damage. After the sputtering process, the Schottky diode typically displays non-ideal effects as well as reduced response time associated with the large interface capacitance formed at the interface. These issues have been previously addressed in the literature [1]. Interestingly, deposition of gold, Pd and Ni metal contacts at cryogenic temperatures have been shown to increase the quality of the diodes [45].

On the other hand, use of graphite or graphene as a metal electrode on GaN substrates are advantageous, since the deposition of these materials can be as easy as micro mechanical exfoliation of multi- layer- graphene onto GaN substrate, application of graphite paint, a mapping graphite-graphene grown on nickel and/or copper thin foils on GaN. The deposition of multi- layer- graphene (or graphene) takes place at room

temperature and does not require advanced deposition techniques that create surface states at the M-S interface. In this study, the HOPG samples have been supplied by Professor J. R. Fischer (U Penn) and natural graphite samples from Brazil by Professor A. Castro Neto. Multi- layer- graphene contacts have been deposited on GaN by micro mechanical exfoliation on n-type GaN crystals and use of thermal release tape as discussed in this chapter. GaN wafers are doped with silicon and were grown on sapphire wafers in Dr. Abernathy's laboratory.

The current density (J-V) characteristics across a multi- layer- graphene/n-type GaN samples are measured from 5 K up to 330 K and shown in Fig. 3-12. The forward bias characteristics are depicted in Fig. 3-13 from 330 K down to 250 K and at fixed voltage the forward bias current increases as the temperature is increased. The increase in current density with the temperature can be explained using thermionic emission theory, meaning as the temperature is increased the average thermal energy of electrons crossing the M-S increases, thus increasing the possibility of overcoming the Schottky barrier and increasing the total current density. Similarly, the reverse bias saturation current density increases with temperature consistent with the interpretations in the previous section and Eq. 1–38. We note that the $J-V$ characteristics also show a rectifying behavior at temperatures as low as 5 K. Even though, technologically inapplicable, rectification observed at 5 K is very interesting since most of the conventional ohmic contacts are known to be failing at low temperatures and graphite can easily be driven into the ultra-quantum regime at laboratory attainable magnetic fields ($\sim$3 Tesla) and metal in the ultra-quantum regime / semiconductor junctions are physically interesting to study. However, this chapter strictly focuses on the physical properties of multi- layer- graphene/GaN junctions.

When the contact area is unknown, the activation plots are an ideal method to predict the Schottky barrier at the M-S interface. In the forward bias, the current density graphs displayed at least 2 decades of linearity at various temperatures

(Figs. 3-12- 3-13). Linearity in a wide voltage range implies that the dominant transport process is thermionic emission and is described by Eq. 3–1, and in principle the Schottky barrier height can be extracted out by using Eq. 3–1 when the active contact area is known. When the contact area is not accurately known, the Schottky barrier height can be estimated by using Eq. 3–2). In this technique, $I-V$ measurements are taken in a temperature window typically around 250 K up to 330 K and their saturation current values are ploted in $\ln(I_s(T)/T^2)$ versus T^{-1} form. These plots have displayed linear dependence and we have found that the the effective Schottky barrier heights that are calculated from the slopes were around 0.30 eV (Table 3-1) with ideality factors (η) spanning from 1.1 to 2.0 for all samples in the 250 K-330 K temperature range (Fig. 3-14).

3.7 Discussion

3.7.1 Comparison of Φ^{I-V} to Φ^{C-V} and Determination of $\phi_{graphite}$

In the previous sections, the Schottky barriers formed at the multi- layer- graphene and Si, GaAs, 4H-SiC and GaN substrates are studied at various temperatures. All the diodes have displayed a rectifying behavior at room temperature and the Schottky barrier height formed at the metal-semiconductor interface is determined from $J-V$ measurements by use of thermionic emission theory / Richardson equation given by Eq. 3–1, from $C-V$ measurements by using depletion capacitance expression (Eq. 1–44), and $I-V$ measurements using activation method, by plotting $\ln(I_s(T)/T^2)$ with respect to the T^{-1}, given by Eq. 1–43. The extracted Schottky barrier heights using various techniques on different junctions are listed in Table 3-1. In this table, the Schottky barrier height of the GaN/ multi- layer- graphene could not be determined using $C-V$ plots due to the high resistivity of the samples. In such cases, the high series resistance masks the data and further processing, data mining and reinterpretation of the raw data is required (refer [11] and section 2.2.3). On the other hand, multi- layer-graphene-graphene/4H-SiC junctions do not display enough linearity in the activation

energy plots and Schottky barrier height can not be accurately determined. The Schottky barrier at multi- layer- graphene/SiC interface can be estimated using Eq. 1–41 using the measured optical contact area and theoretical value of the Richardson constant by fitting the $J-V$ curves in Fig. 3-7.

The barrier heights extracted from $J-V$ and $C-V$ measurements roughly agree with each other. However in Table 3-1, the barrier heights obtained from the $C-V$ measurements are systematically higher than the barrier heights extracted out from $J-V$ measurements. This discrepancy between the two barrier height values can be attributed to interface impurities or thin oxide layer and to the Schottky barrier inhomogeneities. Existence of a thin oxide layer on the semiconductor surface is expected to form another barrier at the interface. Electrons are expected to tunnel through this thin barrier and in principle current voltage measurements are insensitive to the thin oxide layer. On the other hand, capacitance measurements are more seriously affected since thin oxide layer separating metal electrode from the semiconductor acts as a capacitor (C_{ox}) in series with the depletion capacitance (C_{dep}) and thus masks the voltage dependence of the C_{dep} giving slightly higher Schottky barriers. Another reason for higher values in barrier heights determined by the $C-V$ method related to Schottky barrier inhomogeneties. In reality the metal electrodes form a Schottky diodes on the semiconductors that are laterally inhomoneous. The lateral variation of the Schottky barrier heights has been experimentally displayed on Co/GaAs junctions [46]. When the Schottky barrier height is laterally varying, the $J-V$ and $C-V$ techniques gives different answers: $J-V$ technique probes the low Schottky barrier patches while the $C-V$ method takes an average overall of the surface since it probes the depletion width and the capacitive response rather than resistivity across the M-S interface.

In the literature, effects causing η greater than unity, are quantitatively taken into account in determining the Schottky barrier height by finding the flat band zero-electric-field Schottky barrier height [43], ϕ_{FB}. When the diode is driven in the

flat band mode; surface states, if they exist, are depleted of charge and tunneling and image force lowering effects are not present. For η in the $1.05 \leq \eta \leq 2.2$ range, theoretical arguments supported by experimental data suggest the following relation [43] to calculate ϕ_{FB}:

$$\phi_{BF} = \eta\phi_{I-V} - (\eta - 1)(k_B T/e)\ln(N_C/N_D) \tag{3–4}$$

where N_D and N_C are respectively the doping density and the effective density of states in the conduction band. Using this expression, the calculated ϕ_{FB} values are found to be larger than ϕ_{I-V} and are closer to the SBH values determined by the C-V measurements (Table 3-1).

Next, using the Schottky-Mott relation, $\phi_{FB,I-V} = \phi_m - \chi$, which relates Schottky barrier height, Φ_{SBH}, to the metal work function ϕ_m and the semiconductor electron affinity χ, together with the assumption that the Fermi levels of the semiconductors are not pinned, we calculate the multi- layer- graphene contact work function ($\phi_{graphite}$) to be in the range 4.40 eV-4.60 eV (Table 3-1). Our values of $\phi_{graphite}$ determined separately on Si, GaAs, 4H-SiC and GaN substrates are in good agreement with the theoretically and experimentally determined values (ranging from 4.4 eV to 4.8 eV) reported in the literature [47–49].

3.7.2 Bond Polarization Theory and Multi-Layer-Graphene to Graphene Limit

According to the Schottky-Mott relation, formed Schottky barrier is mostly sensitive to the metal work function and the semiconductor's electron affinity value. The Schottky-Mott relation gives a rough idea about the Schottky barrier height and the formation mechanism of the barriers at the interface. So far Schottky barrier heights deviating from the Schottky-Mott relation have been reported in the literature and different mechanisms have been attributed to explain such deviation [3]. In GaAs, the deviation is mostly attributed to the Fermi-level pinning, while for Si it is non-ideal effects. Due to some deviations from the Schottky-Mott picture, other physical mechanisms have

been proposed: (1) Metal induced gap states (MIGS) model and (2) bond polarization theory. The details of these theories can be found in other review articles [1]. In the literature, it is commonly accepted that MIGS finds better agreement with the experimental values while it makes unrealistic assumptions and physically sound bond polarization theory explains the physical mechanism well but can not estimate the Schottky barrier on some systems.

According to the bond polarization theory, the Schottky barrier height is somewhat related to the metal work function and semiconductor's electron affinity values. However, this theory emphasize on the interaction at the first few layers of the metal-semiconductor interface and formation of the bonds after the metal is kept in contact with the semi conductor. Followed by this bond formation at the interface, a typical interface dipole layer is created. And the electrical field associated with the dipole layer is typically very strong and determines the barrier height seen by the electrons moving across the M-S interface. So far the band polarization theory successfully explained Fermi level pinning effect, observed Schottky barrier inhomogeneity [46], first principles simulations performed at the M-S interface and associated charge transfer [50, 51].

Within the bond polarization theory, the measured results on multi- layer- graphene based Schottky diodes formed on various semiconductors imply that the same rectification would also be expected on graphene Schottky junctions. According to the bond polarization theory, the Schottky barrier properties are determined by the very first few layers of the metal and the semiconductor and since the multi- layer- graphene is made out of graphene in the Bernal stacking, the same effect is also expected to be observed on the graphene based systems.

Another argument for graphene based Schottky diodes on the similar semiconductors comes from the Schottky-Mott model and the dependence of the work function on the number of layers in graphene and multi- layer- graphene. From the density functional theory (DFT) calculations, the Fermi level of the graphene/ graphite/ multi- layer-

graphene is previously shown to be very weakly dependent on the number graphene layers involved in the crystal [48]: For graphene the work function is 4.46 eV and it increases to 4.51 eV for 7 layers of graphene (graphene becomes bulk graphite or multi- layer- graphene like after 4-5 layers). Therefore, within the Schottky-Mott model, graphene is expected to display rectifying behavior since the work function of graphene and graphite is almost identical.

3.8 Conclusion

In conclusion, we have demonstrated the formation of high-quality Schottky contacts using a *soft-landing* multi- layer- graphene contact on *n*-type Si, GaAs, 4H-SiC and GaN semiconducting substrates. Fabrication can be as easy as allowing a dab of HOPG paint to air dry on any one of the investigated semiconductors. Thermionic emission theory describes well the behavior of the multi- layer- graphene/ Si:P and multi- layer- graphene/GaAs:Si junctions from 250 K to 330 K. We attribute the observed non-linearity in the Richardson plots of the multi- layer- graphene/4H-SiC junctions to inhomogeneity at the multi- layer- graphene-semiconductor interface. The extracted values Φ_{SBH} roughly obey the Schottky-Mott relation with inferred graphite work functions agreeing well with literature values. Our results not only provide unexpected insights into the nature of the multi- layer- graphene /semiconductor interface but also anticipate applications where single-layer graphene is directly contacted to a semiconductor substrate rather than isolated by an insulating oxide [42] or grown directly on undoped insulating semiconductors [52].

Table 3-1. Extracted SBHs, doping densities, and corresponding graphite work function values on various multi-layer-graphene/semiconductor junctions

	ϕ_{Bo}	ϕ_{BF}	ϕ_{C-V}	N_D^{C-V}	N_D^{Hall}	ϕ_{HOPG}
junction type	[eV]	[eV]	[eV]	[cm^{-3}]	[cm^{-3}]	[eV]
HOPG/*n*Si	0.40	0.60	0.70	$1.2 \cdot 10^{15}$	$1.0 \cdot 10^{15}$	4.60
HOPG/*n*GaAs	0.60	0.78	0.76	$3.6 \cdot 10^{16}$	$3.0 \cdot 10^{16}$	4.78
HOPG/*n*4H-SiC	1.15	1.60	1.84	$1.2 \cdot 10^{16}$	$1.0 \cdot 10^{16}$	4.80
HOPG/*n*GaN	0.31	0.43	NA	$1.2 \cdot 10^{16}$	NA	4.45

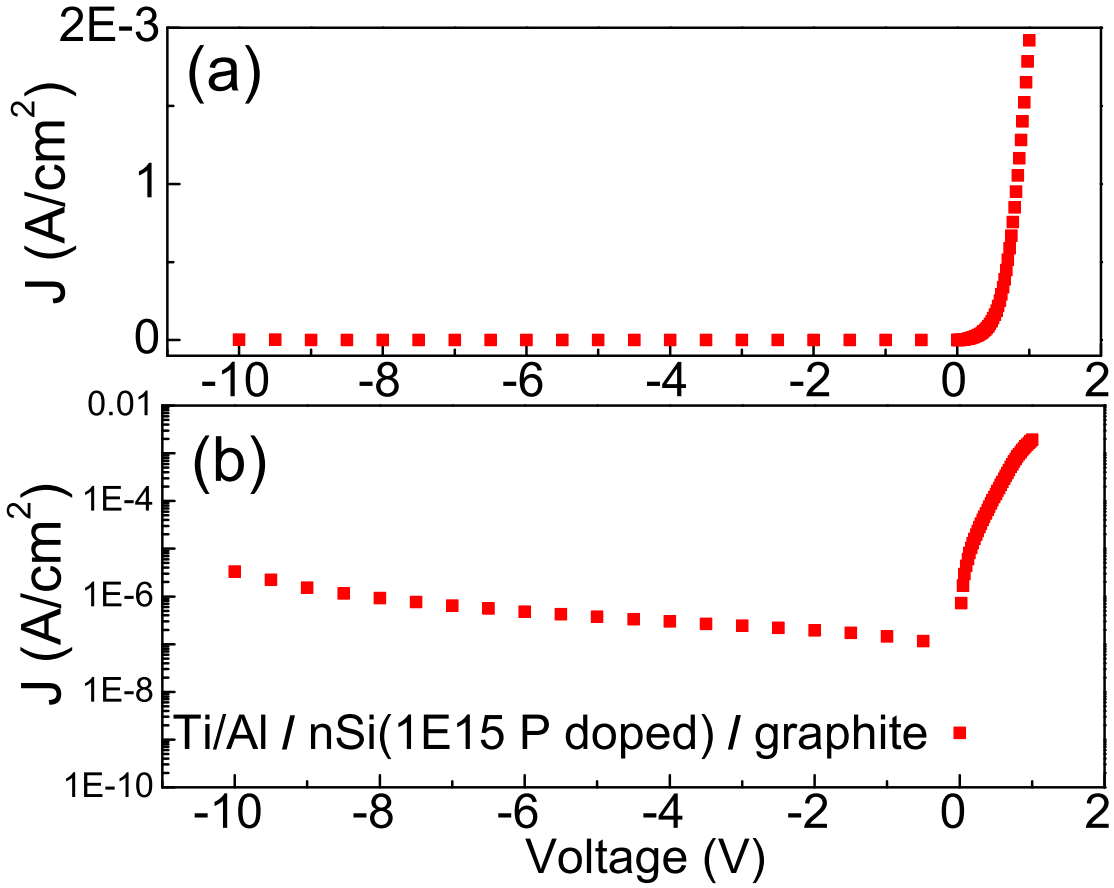

Figure 3-1. Plots of the room temperature current density J with respect to applied bias V on n type multi-layer-graphene/Si:P junctions $J-V$ plots on (a) linear and (b) semilogarithmic axes

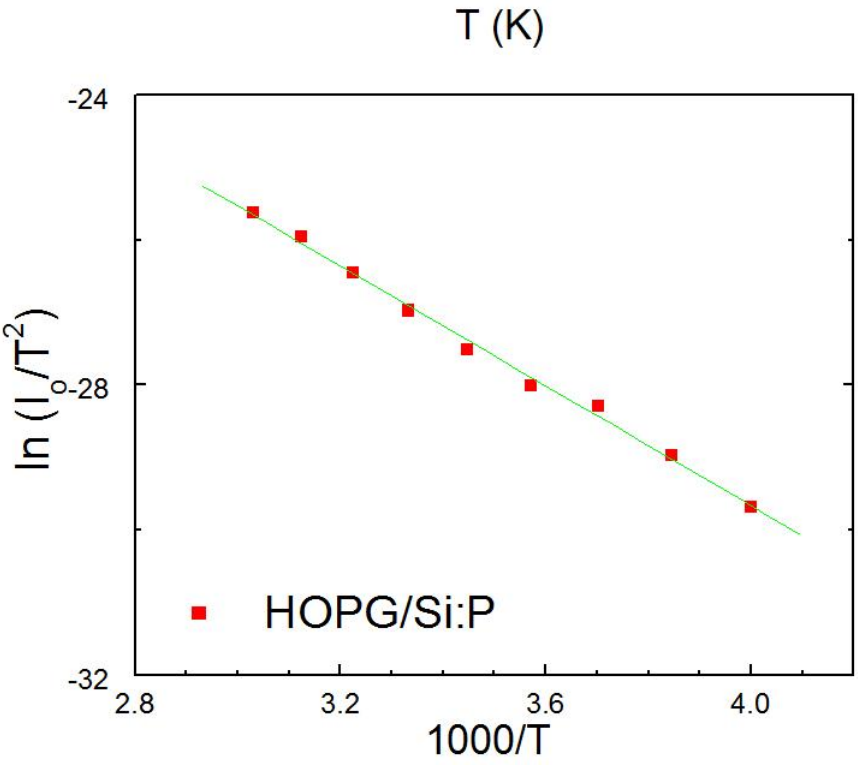

Figure 3-2. Richardson activation plots ($\ln I_s/T^2$) as a function of T^{-1} from 250 K up to 330 K on multi-layer-graphene/Si:P

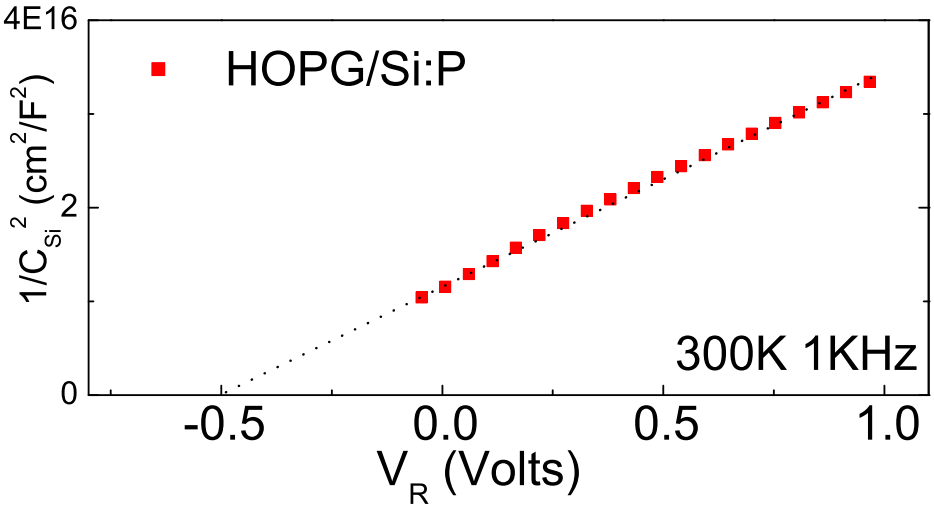

Figure 3-3. Inverse square of capacitance per unit area measured at 1 kHz as a function of reverse bias at room temperature: multi-layer-graphene/Si:P

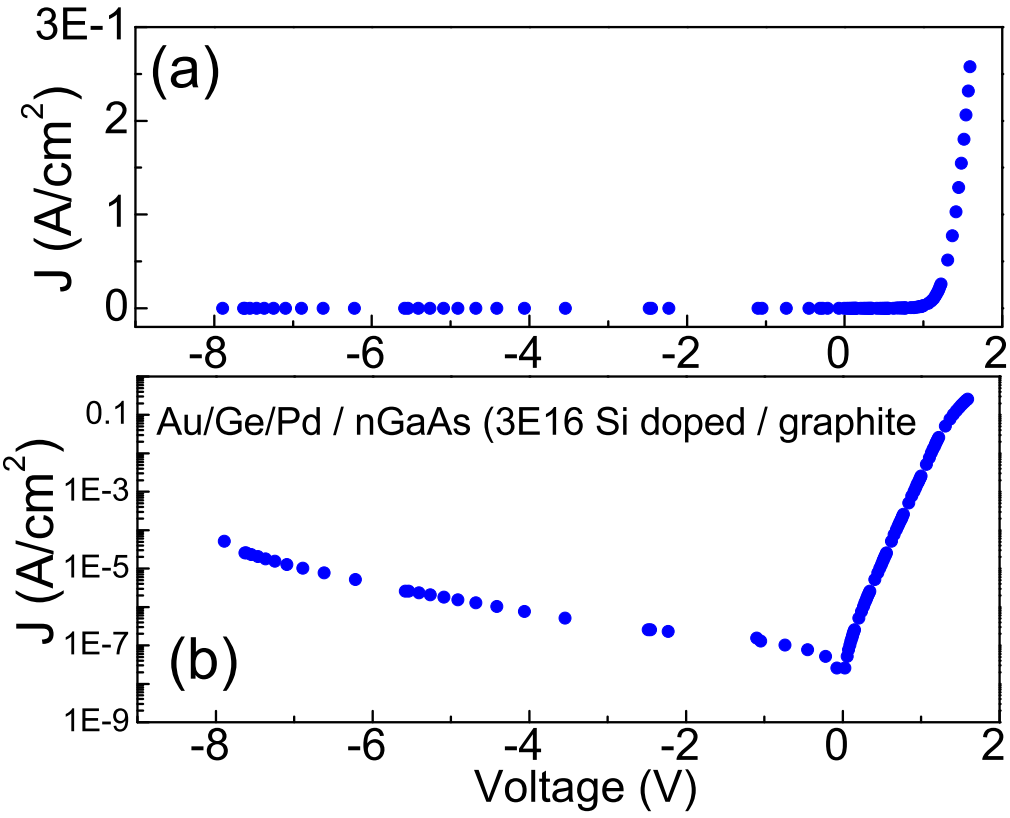

Figure 3-4. Plots of the room temperature current density J with respect to applied bias V on n type multi-layer-graphene/GaAs:Si junctions $J-V$ plots on (a) linear and (b) semilogarithmic axes

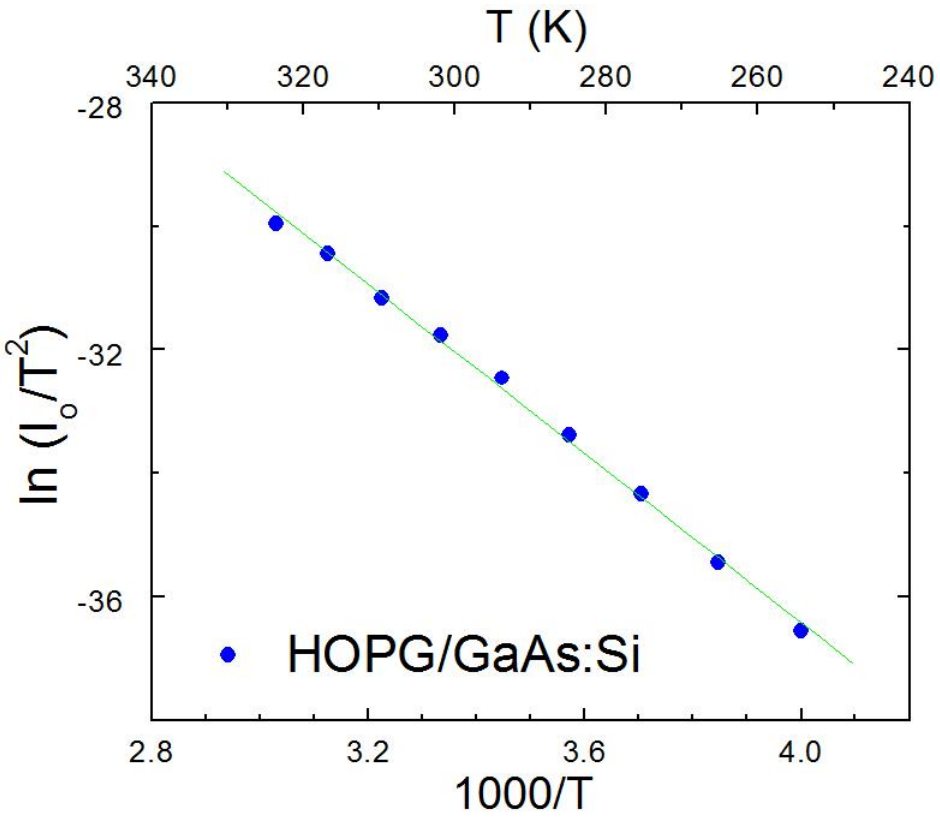

Figure 3-5. Richardson activation plots ($\ln I_s/T^2$) as a function of T^{-1} from 250 K up to 330 K on multi-layer-graphene/GaAs:Si junctions.

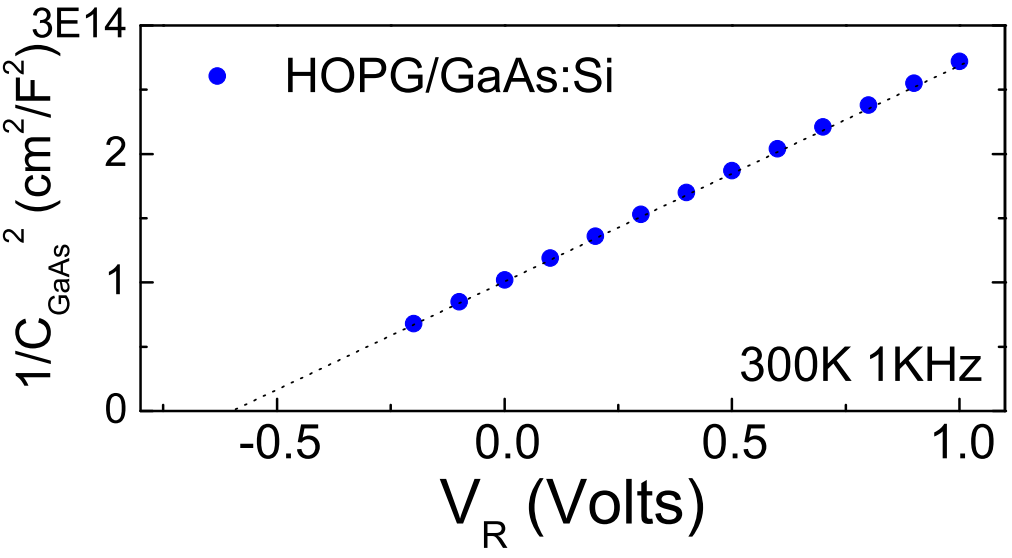

Figure 3-6. Inverse square of capacitance per unit area measured at 1 kHz as a function of reverse bias at room temperature: multi-layer-graphene/GaAs:Si

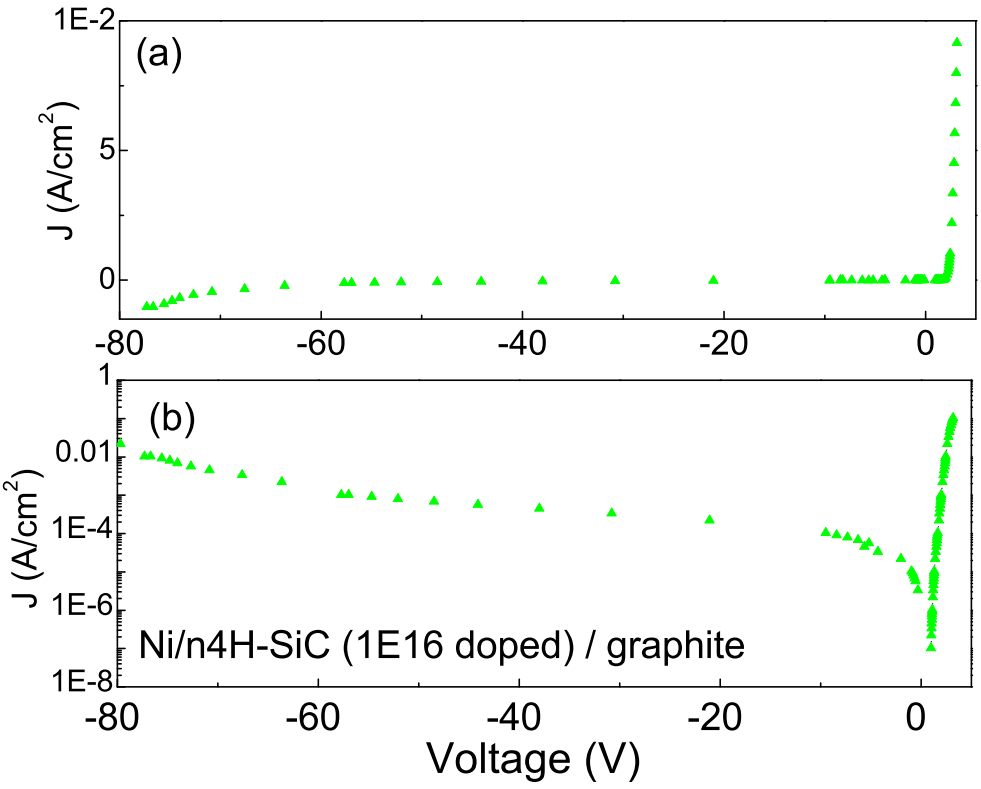

Figure 3-7. Plots of the room temperature current density, J, with respect to applied bias V on n-type 4H-SiC/multi-layer-graphene junctions $J-V$ plots on (a) linear and (b) semilogarithmic axes

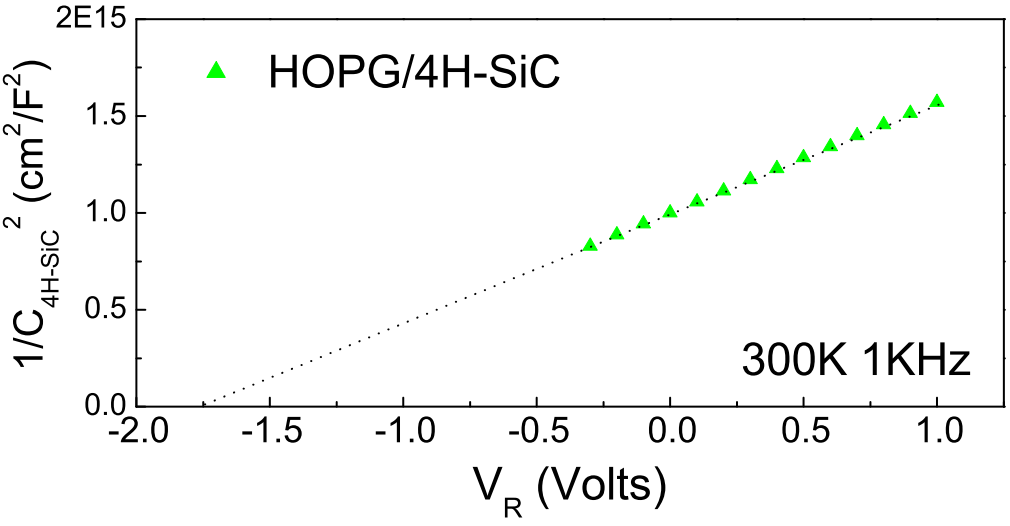

Figure 3-8. Inverse square of capacitance per unit area measured at 1 kHz as a function of reverse bias at room temperature on multi-layer-graphene/4H-SiC.

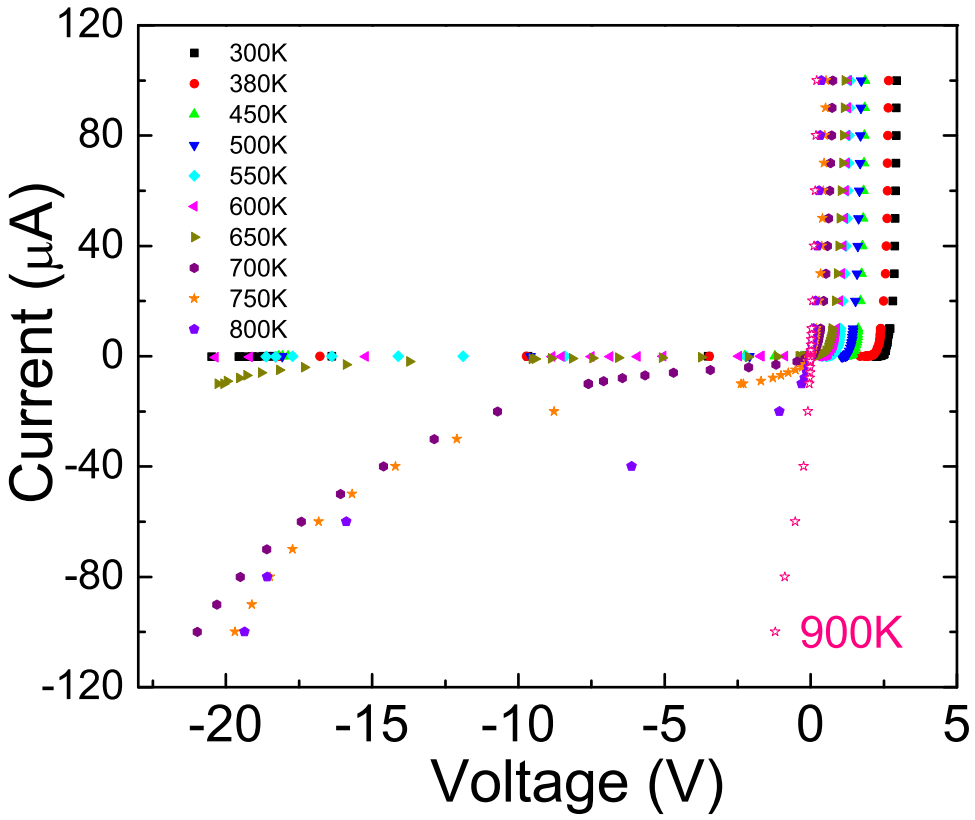

Figure 3-9. I-V characteristics of multi-layer-graphene/4H-SiC Schottky barriers from 300 K up to 900 K.

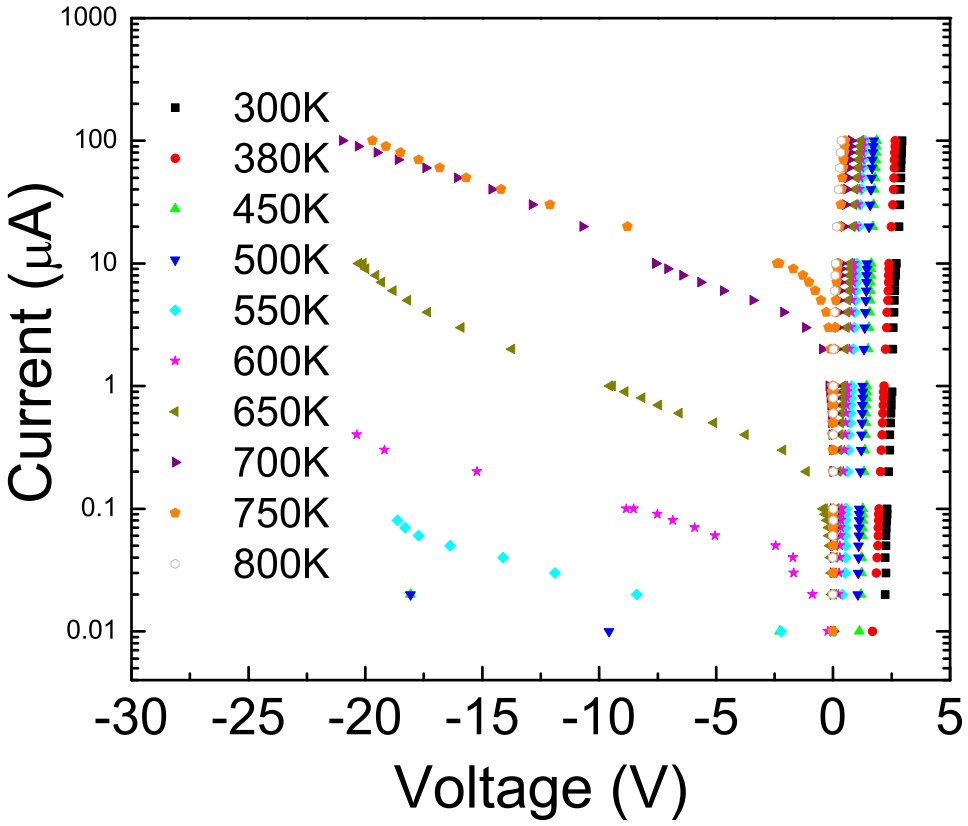

Figure 3-10. I-V characteristics of multi-layer-graphene/4H-SiC Schottky barriers from 300 K up to 800 K in the semilogarithic form.

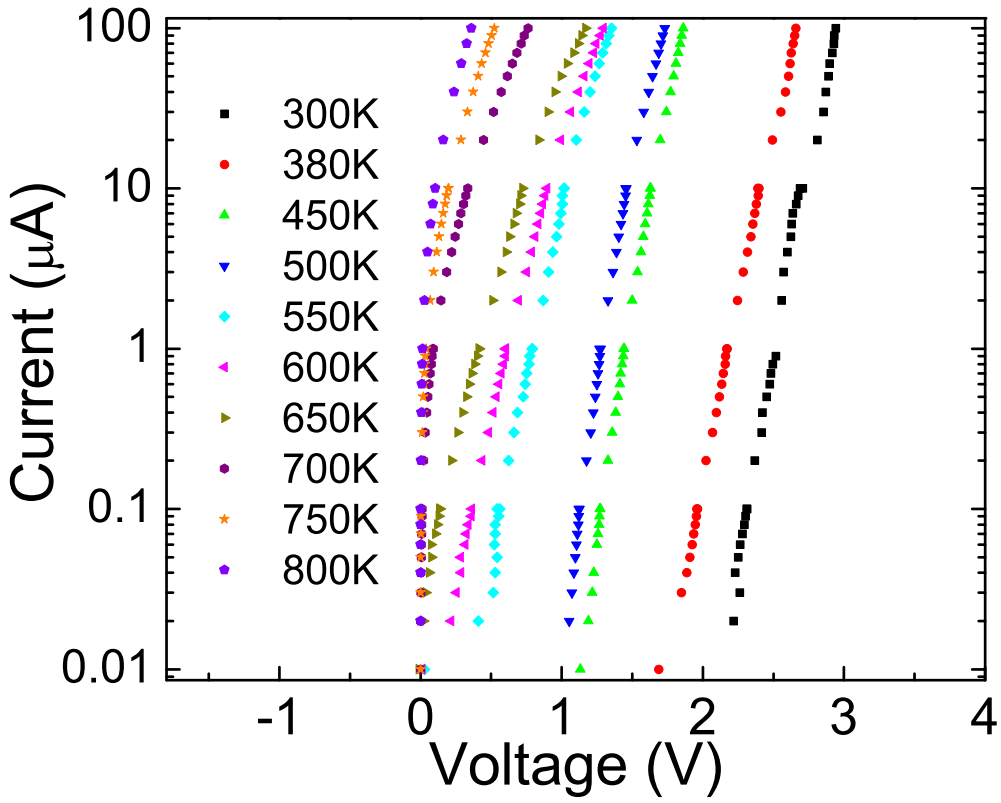

Figure 3-11. I-V characteristics of multi-layer-graphene/4H-SiC Schottky barriers from 300 K up to 800 K in the semilogarithic form in the forward bias.

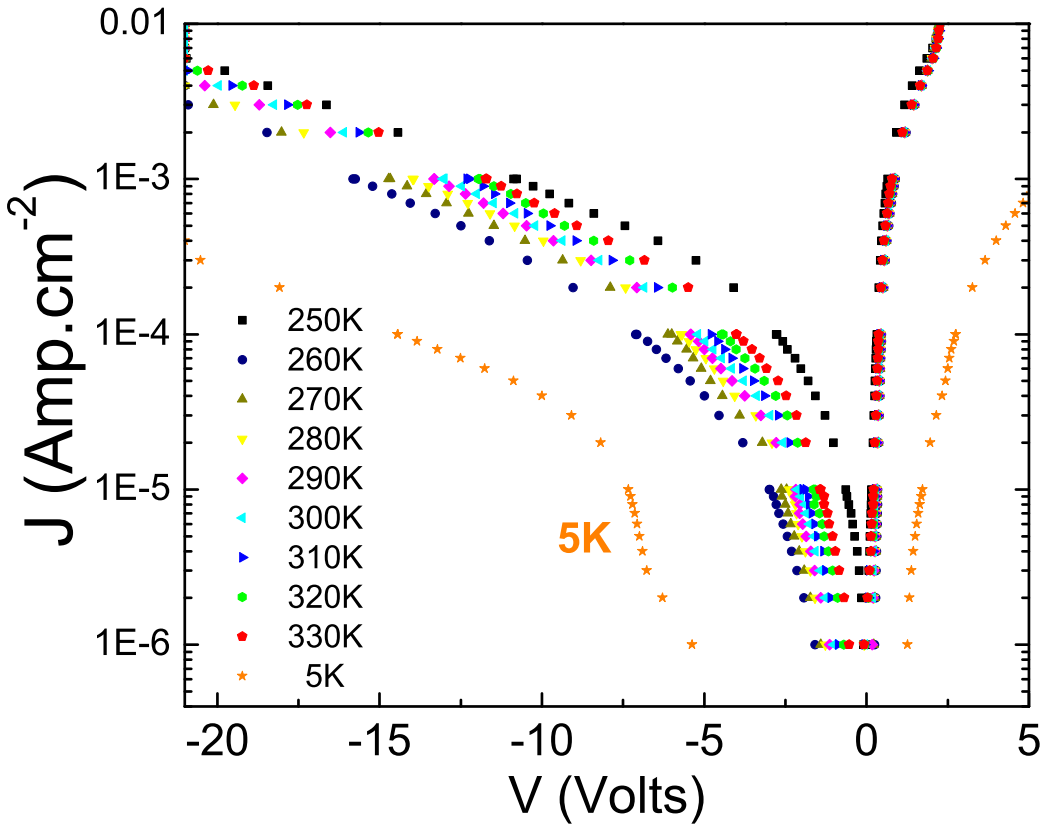

Figure 3-12. Semilogarithmic J-V characteristics of multi-layer-graphene/GaN:Si Schottky barriers from 5 K up to 330 K.

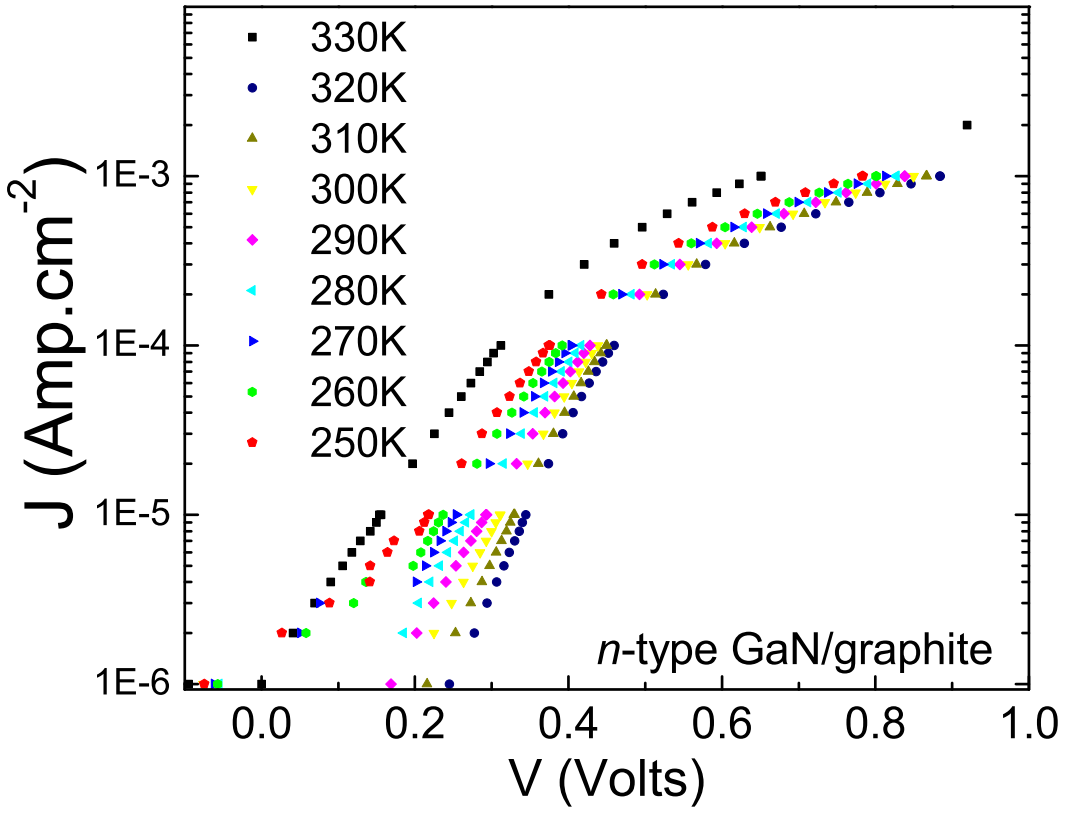

Figure 3-13. Semilogarithmic J-V characteristics of multi-layer-graphene/GaN:Si Schottky barriers from 5 K up to 330 K in the forward bias direction.

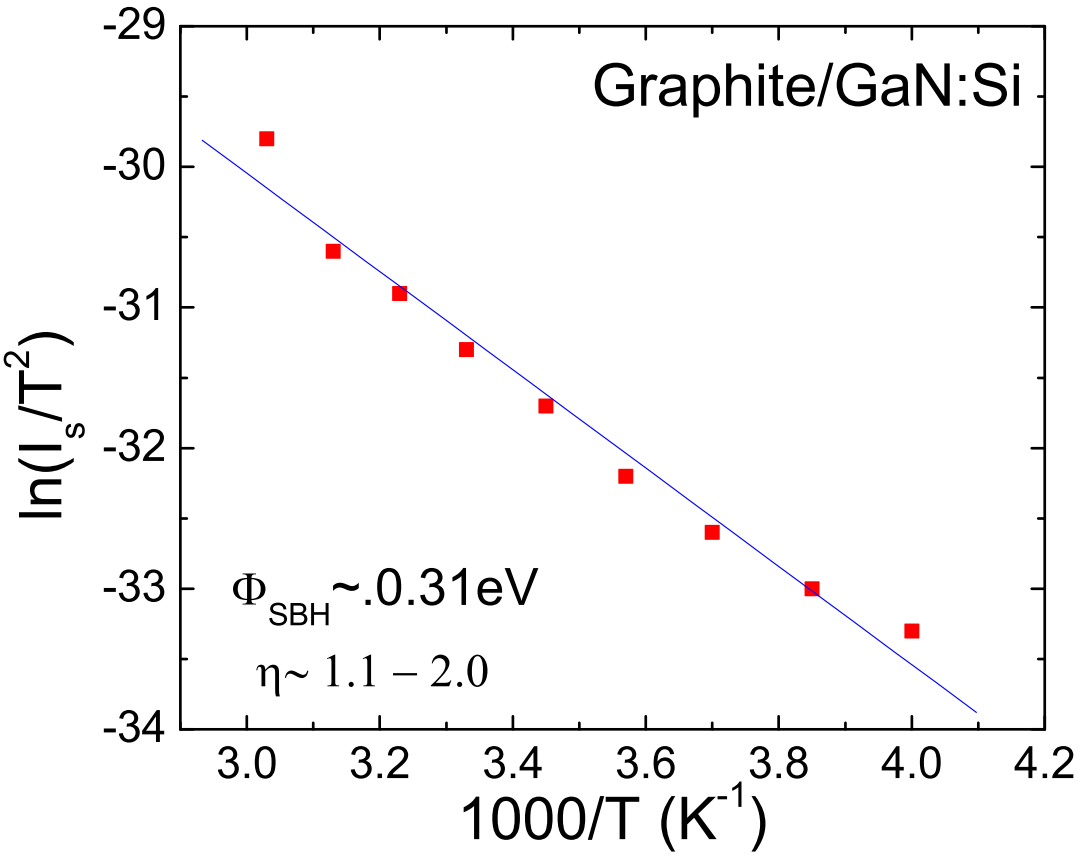

Figure 3-14. Richardson activation plots ($\ln I_s/T^2$) as a function of T^{-1} from 250 K up to 330 K on multi-layer-graphene/GaN:Si.

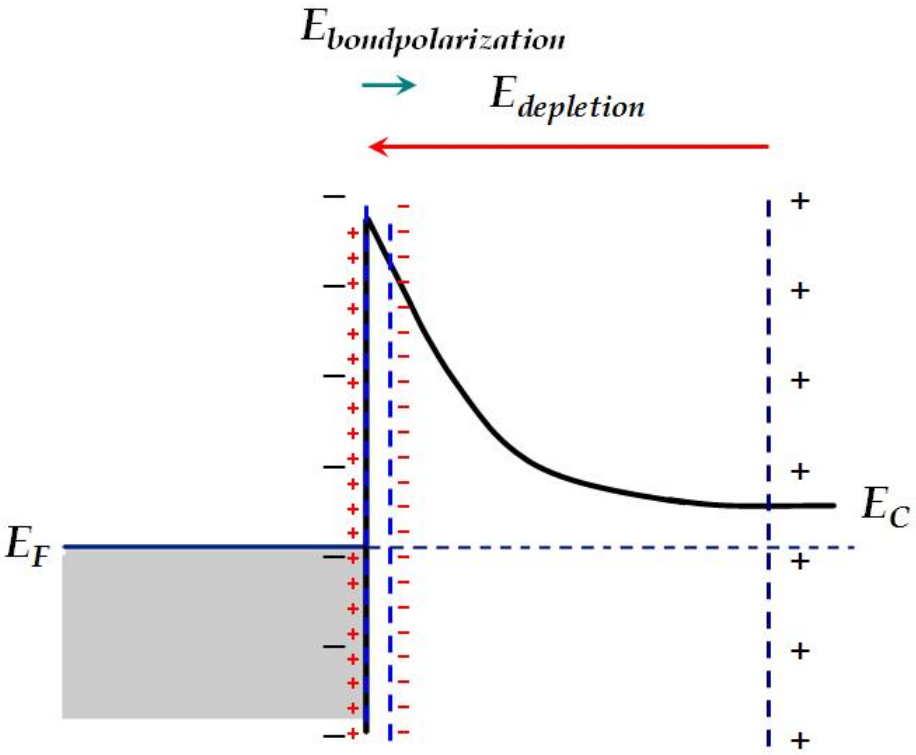

Figure 3-15. Bond polarization theory Schematics

CHAPTER 4
TUNING SCHOTTKY BARRIER HEIGHT AT THE MULTI-LAYER-GRAPHENE / SEMICONDUCTOR INTERFACE BY DOPING

4.1 Introduction

Schottky barriers formed at the metal-semiconductor interfaces are key components of metal - semiconductor field effect transistors (MESFET) and high electron mobility transistors (HEMTs) that are widely used in high frequency, high power device applications. These devices mostly rely on good characteristics of Schottky barriers and any control on the physical properties of Schottky barrier is crucial for efficient operation of the device. If higher Schottky barrier height is achieved, this results in larger gate-breakdown voltage, power gain and output resistance and lower gate leakage current and noise. Tuning of Schottky barrier height has been achieved by applying pressure [53] on the junction, controlling the crystal structure and grain size of metal electrodes [22]. However these methods require special conditions such as order of GPa range pressure and cryogenic metal deposition.

On the other hand, carbon based materials have been the center of attention for more than 5 decades in different forms as 0D fullerenes, 1D carbon nanotubes, 2D graphene and 3D graphite. Although, integration of carbon into existing conventional devices faces numerous challenges, their unique physical properties make them a good candidate for future's electronics applications [35]. Specifically graphene; which is two dimensional single layer of sp^2 bonded carbon atoms and graphite, many layer graphene sheets with Bernal stacking, are of particular interest due to their exotic band-structure, excellent conductivity, high mobility and stability as well as tunability of their properties by the interaction with ambient gases or intercalant atoms / molecules (graphite intercalation compounds (GICs)) [54]. Published demonstration of Schottky barrier formation on various semiconductors using multi- layer- graphene to replace the metal electrode [55] anticipated in accord with bond polarization theory, that graphene

should manifest the same behavior, since the Schottky barrier characteristics are mainly governed by the first layer of multi- layer- graphene at the interface (subsection 3.7.2)

In this chapter, we will report the tuning of Schottky barriers formed between multi- layer- graphene and various types of semiconductors (*n*-Si and 4H-SiC) by bromine intercalating the semi-metal multi- layer- graphene electrode. Prior to bromine intercalation, Schottky barriers displayed typical rectifying *J-V* and linear C^{-2} vs. V_R characteristics. The small coupling between each graphene sheet allows us to intercalate bromine in between the planes and increases the separation in between each consecutive graphene planes. As the intercalant diffuses in between the layers, the lattice constant increases and inter layer coupling parameters diminish, therefore pushing graphite / multi- layer- graphene into graphene limit. Charge transfer in between carbon atom and strong electronegative bromine intercalant increases the total hole carrier density of multi- layer- graphene / graphite / HOPG and the work function, $\phi_{graphite}$. Within the Schottky-Mott relation (Eq. 1–12) an increase in $\phi_{graphite}$ leads to an increase in Schottky barrier height which is confirmed from *J-V* and *C-V* measurements. Tuning Schottky barrier height at the multi- layer- graphene / semiconductor interface has important implications in HEMTs and MESFETs as well as integration of carbon based materials into existing conventional semiconducting devices.

4.2 Experimental Procedure

We have used commercially available *n*-type Si:P (10^{15}-10^{16}cm^{-3}) and layered 4H-SiC wafers compromising 5μm epilayer (10^{16}cm^{-3}) grown on insulating SiC substrates. Prior to Schottky diode formation,ohmic contacts are made using multi-layer ohmic contact recipes existing in the literature [3, 56]. Multilayers are deposited by thermal evaporation and/or RF sputtering at 10^{-7} Torr and followed by rapid thermal annealing (RTA) annealing in N_2 gas for various times. Ohmic contacts displayed linear and low contact resistance from 300 K down to 20 K.

multi- layer- graphene Schottky diodes are formed on the substrates by three different techniques: (a) mechanical exfoliation of multi- layer- graphene using thermal release tape (refer to Chapter 3 for experimental details) (b) application of graphite paint; mixture of residue free 2- butoxyethyl acetate and octyl acetate with graphite powder collected from dicing HOPG by diamond impregnated wire [55] at controlled rates and (c) mechanical exfoliation of natural graphite and HOPG [42]. In the latter technique, multi- layer- graphene flakes typically flatten out on the smooth substrate surface due to the Van der Walls (VdW) interaction between the multi- layer- graphene and the semiconducting substrate.

Semi-metal multi- layer- graphene contacts placed by mechanical exfoliation or graphite paint method on the semiconducting substrates are then bromine intercalated by direct bromine gas exposure. The bromine exposure is performed at room temperature in a sealed chamber for various duration times. An addition to these methods, the graphite paint contact solution can be made out of already bromine intercalated graphite powder. In this method, the graphite powder is bromine intercalated prior to mixing with organic solvents (rather than direct bromination of the pristine graphite paint contact) and 'brominated graphite paint' directly applied to the different semiconducting substrates. The *J-V* characteristics are measured using Keithley 182/220 or Keithley 2400 current-source meter and *C-V* using Agilent 4284A LC capacitance bridge. A total of 15 samples were prepared by the methods described above, 'direct bromination' and 'brominated multi- layer- graphene flake paint' method. Measured *I-V* and *C-V* characteristics did not show any dependence on the type of method followed.

Changes in the properties of multi- layer- graphene / graphite / HOPG such as crystal structure changes, atomic percentages and change in E_F in graphite are measured by X-ray diffraction (XRD), Auger electron spectroscopy (AES), X-ray photoelectron spectroscopy (XPS) respectively. Graphite pieces used in this work displayed typical $\theta - 2\theta$ XRD with 0.5 degree mosaic spread measured by x-ray omega

rocking curve (ω-RC) measurements and no contamination using in AES and XPS measurements was observed prior to the bromination.

4.3 Results and Discussion

4.3.1 Effect of Bromine Doping on the MLG / Semiconductor Schottky Barrier Diode $I-V$ Characteristics

The two panels in the Fig. 4-2 display the measured current density (J) versus applied voltage (V) characteristics at the multi- layer- graphene/ n-Si junction before (red squares) and after (blue triangles) the bromine exposure. The J-V characteristics measured on 15 different samples show a good rectification [55] with Schottky barrier heights values and ideality factors (η) spanning around 0.4 eV-0.6 eV and 1.12-1.90 respectively. The blue triangles in Fig. 4-2 correspond to J-V characteristics after the 'direct bromine exposure' at the same interface. A one decade decrease in the forward bias current density (J_{For}) and a two decades decrease in the reverse bias current density (J_{Rev}) implies that multi- layer- graphene / semiconductor interface and semi-metal multi- layer- graphene are sensitive to bromine exposure. Reported results in this work are independent of the method for forming multi- layer- graphene junction, bromination technique as well as type of semiconductor used. Similar changes / trends in J-V and C-V measurements are measured on samples prepared by 'direct bromine exposure' on graphite paint / semiconductor and 'brominated graphite paint' / semiconductor junctions. Moreover, existence of such effects on other conventional semiconductors such as GaN, 4H-SiC and GaAs means that bromine sensitivity of the diodes is not specific to the type of semiconductor used but originates from the interaction of bromine with multi- layer- graphene semi-metal electrode and associated changes in physical properties of multi- layer- graphene and interface bonding / dipole. The effect of bromine gas on the semiconductors are measured using AES, and XPS. Si and 4H-SiC are found to non-interacting while GaAs strongly interacts with bromine.

Therefore, the effect of on multi- layer- graphene / *n*-GaAs diodes are not reported in this work.

In principle, Schottky barrier height, ϕ_{SBH}, and ideality factor (η) can be extracted out from the thermionic emission over the barrier height using,

$$I = I_s(T)[\exp(qV/\eta k_B T) - 1], \tag{4–1}$$

where $I_s = AA^* T^2 \exp(-q\phi_{SBH}/k_B T)$ is the saturation current, $q\phi_{B0}$ is the zero bias Schottky barrier height, A^* is Richardson constant, T is the absolute temperature, and V is the voltage across the ohmic and multi- layer- graphene contacts. Before Br exposure, Schottky barrier height and ideality factors vary in between 0.4 eV-0.6 eV and 1.12-1.9 respectively on 15 different multi- layer- graphene / *n*-Si samples and are roughly in agreement with the Schottky-Mott model ($\phi_{Sch} = \phi_{graphite} - \chi_{Si}$) with the values of $\phi_{graphite}$=4.5 eV and $\chi_{Si} = 4.01$ [2, 49, 57]. On a semilogarithmic scale, the *J-V* plot displays enough linear region in the forward bias (Fig. 4-2b) and extrapolation to the ordinate at zero bias gives J_s as a measure of zero bias Schottky barrier height (Fig. 4-2b inset). In our measurements, the value of J_s decreases upon bromination on all the samples measured. By intuition, when the Schottky barrier height is higher, fewer electrons overcome the barrier and this causes overall decrease in the measured current density *J*. Following the saturation current expression, $J_s = AA^* T^2 \exp(-q\Phi_{SBH}/k_B T)$, J_s and hence $J_{Forward}$ and $J_{Reverse}$ decreases only if Schottky barrier height increases upon Br intercalation.

4.3.2 Effect of Bromine Doping at the MLG / Semiconductor Interface: Possible Mechanisms

Within the Schottky-Mott model (Eq. 1–12), the increase in the Schottky barrier height can only be attributed to an increase in work function of graphite ($\phi_{graphite}$) or a decrease in the electron affinity of the silicon (χ_{Si}). Bromine is highly reactive and electronegative element with its [Ar] $4s^2\ 3d^{10}\ 4p^5$ electron configuration and interacts

with other substrates in such a way that it makes the material p-type after the charge transfer takes place. In principle, this charge transfer in between the semiconductor and bromine vapor leads to an increase in χ_{Si} rather than decrease in χ_{Si}. Moreover, the absence of an interaction in between bromine and Si, and 4H-SiC as determined from AES and XPS also prevents any charge transfer, and a change in χ_{Si} is not expected. With χ_{Si} fixed, the increase in Schottky barrier height and measured decrease in saturation current density can only originate from an increase in $\phi_{graphite}$. Therefore, change in $\phi_{graphite}$ determines the change in Schottky barrier height at the multi- layer-graphene semiconductor interface. To elucidate this point, various techniques and measurements will be presented in subsection 4.3.3 and the remainder of the chapter.

On the other hand, the bond polarization theory does not directly associate the magnitude of the measured Schottky barrier height only to work function of metal and electron affinity of semiconductor but also incorporates the bonding information at the interface after the metal contact is placed on the semiconductor. After the formation of bonding, the interface dipoles if formed at the interface and the barrier height is mainly dominated by this inhomogeneous region (charge discontinuity). In this case, the barrier height is strongly dependent on the bonding information and the initial binding properties of the metal and the semiconductor surfaces. Upon bromine intercalation, the bonding and the binding information changes at the multi- layer- graphene surface as demonstrated in section 4.3.3 nad causes Schottky barrier to change. And this change is expected be an increase in the barrier height since multi- layer- graphene is more electronegative after the bromine intercalation and draws more electrons for the semiconductor surface.

4.3.3 Characterization of Br Intercalated Graphite: XRD, AES and XPS Measurements

A semi-metal graphite with finite overlap in between conduction (E_C) and valence band (E_V) is relatively clean material with low carrier density ($10^{18} - 10^{19} cm^{-3}$) at 300 K

corresponding to 10^{-5} to -10^{-4} free electron per carbon atom (Chapter 5). Moreover, a large lattice constant and a weak coupling in between consecutive graphene sheets allows bromine atoms/molecules [54, 58] to diffuse in between the layers easily thus enabling the interaction in between Br and C. Intercalation of Br into graphite pushes each graphene sheet apart resulting in visual swelling of the graphite samples in the c-axis direction (perpendicular to graphene sheets) and associated increase in c-axis lattice constant determined from X-ray electron diffraction (XRD) measurements. XRD provides a way to study the structural properties of various systems. We have measured the XRD pattern of brominated samples from 10 degrees to 80 degrees in the θ-2θ configuration using Cu K_α X-ray source and the XRD data taken on pristine HOPG and at various Br intercalation times are shown in Fig. 4-3. The stage index determinations are most sensitively made using (00l) reflections [54]. In our samples, we did not observe any peaks indicating a staging phenomena; moreover, the graphite peaks shift and broaden to a lower 2θ indicating an increase in lattice spacing after the doping procedure related to penetration of bromine between the graphene layers.

Due to the low carrier density per carbon (10^{-5} to -10^{-4} free electron per carbon atom), a small interaction (charge transfer) in between the dopant / intercalant and carbon results in orders of magnitude increase in free carrier density per carbon. The charge transfer occurring in between carbon in the graphite matrix and intercalant bromine can be roughly estimated if the number of bromine atoms per carbon is known. We determine the concentration of bromine intercalated inside the graphite using by Auger electron spectroscopy (AES) and X-ray photoelectron spectroscopy (XPS).

The AES technique, can be used to identify the elemental composition on the surface or in the bulk (by removing material from the surface using ion-beam sputtering). In the AES technique, inner shell electron is excited by high energy electron bombardment (5keV) and followed by an electronic relaxation and emission of Auger electrons. The most pronounced Auger peaks originate from neighboring

orbitals such as KLL, LMM, MNN etc. For elements with Z from 14 to 40, the most prominent transition is LMM. For bromine, Auger peaks appear at 55 eV (MVV) and 1396 eV (LMM) and for carbon at 20 eV and 272 eV (KLL). However low energy Auger electrons scatter and decay easily, therefore their magnitudes are typically rather small or non-observable. In Fig. 4-4, we show Auger spectrum, as dN(E)/dE versus energy, where N(E) is the energy distribution of detected secondary electrons on a bromine doped sample. The scan is typically taken on 100 micron by 100 micron area. Bromine is a weak Auger sensitive element, for this reason HOPG sample has been doped for a long time to observe bromine Auger peaks clearly. Since non-destructive depth profiling is not possible in AES as it is in XPS, samples have been cleaved to probe different depths of the sample and relative bromine concentration have been measured to check for the sample uniformity. Bromine Auger peaks located at 1396 eV and 1442 eV corresponds to LMM Auger transitions and different depths in the same sample shows similar bromine concentration implying that the sample is uniform. Moreover, scans taken at different parts on the surface of the sample also shows similar concentrations of bromine implying within 100micron by 100micron resolution. 1% to 5% charge transfer measured by AES roughly gives 10^{-2} charge transfer. Large charge transfer in between Br and C strongly changes hole carrier density [58], and Fermi level (E_F) of the graphite as confirmed by XPS measurements (Fig. 4-5b).

Another method for measuring the percentage composition at the surface is X-ray photoelectron spectroscopy (XPS). Surface sensitivity and quantitative and chemical state analysis capabilities of XPS technique allow us to analyze the physical properties of bromine doped samples at room temperature. However, the depth of the material sampled varies from 2 atomic layers up to 10-20 atomic layers depending on the electron mean free path of created ejected electron after core electrons are ionized by radiated x-rays. For carbon it is typically in between around ten angstroms but the depth of the material sampled can be varied by changing the incoming xray beam angle

(hence x-ray penetration depth) and this allows us to selectively probe surface and bulk-like regions. High energy photon (or short wavelength) can ionize an atom and produces an ejected free electron. According to Einsteins photoelectric law, the binding energy of the particular electron to the atom can be extracted out if the kinetic energy of ejected electron is measured.

$$K.E = h\nu - B.E, \tag{4–2}$$

The binding scale is calibrated taking the Au4f level at 83.9 eV. Studied pristine graphite samples are cleaved before introduction in the the UHV chamber for XPS measurements. After the XPS measurements are performed on pristine graphite,the samples are exposed to bromine gas as described above to study the effect of bromine doping. The studied samples were conductive before and after the bromine doping and no charge effect has been detected. When there are no charging effects, binding energies of individual atom / level are directly measured with respect to the Fermi level of the studied sample. Therefore any shift of the particular elemental peak position not only gives an idea about bonding information but also shifts in the Fermi level in the system. The entire XPS spectrum of 30 min. bromine exposed graphite sample is measured using a monochromatized Mg X-ray source from 0 eV up to 1100 eV in a UHV chamber Fig. 4-5a. After pristine graphite is exposed to bromine vapor, bromine 3d and 3p orbital peaks appear at 68.5 eV and 181.7 eV respectively and found to be around 1% to 3%. In XPS measurements elemental peaks such as C 1s, are measured with respect to the Fermi level of the system. When the E_F of the system changes drastically as it does in graphite intercalation compounds, the change in the Fermi level of the system manifests itself as a change in the C 1s elemental peak position and these relative changes in the C 1s peak positions provide a way to estimate the changes in E_F. The C 1s electron binding energy of pristine graphite is typically at 284.5 eV consistent with the reported values in the literature [59] and after the intercalation C 1s

peak lowers to 284.1-283.9 eV (Fig. 4-5b). However, interaction of carbon atoms with highly electronegative bromine creates positively charged carbon atoms which possess a higher binding energy. The experimentally measured decrease in binding energy as opposed to an increase as predicted by electrostatic rule can be explained by redefining the E_F of the system after the bromination. In brominated graphite, the Fermi level is known to be signicantly larger in magnitude compared to pristine graphite and the C 1s binding energy is thus measured with respect to the lower E_F of the hole doped system. Accordingly, the increase in the C 1s binding energy is more than compensated for by the decrease in E_F , giving an overall decrease in the C 1s peak position as observed. Similar results and trends have been reported in the literature [60, 61] for different graphite intercalation compounds. This method thus gives a lower limit to the order of magnitude change of E_F which from Fig. 4-5b corresponds to 0.5 eV.

4.3.4 Modification of the Band Structure at the Interface and $C-V$ Measurements

The decrease in E_F, or an increase in $\phi_{graphite}$, changes the band structure at the multi- layer- graphene / semiconductor interface as shown in Fig. 4-6c-d. Before contact is made, the Fermi level of the semiconductor already lies above the Fermi level of the pristine graphite. After thermal equilibrium electrons in the semiconductor flow into the low energy states in the graphite, making E_F constant throughout the system and creating positively charged donors atoms in the depletion width (W) Fig 4-6b-d. Within this picture, Schottky barrier height equals to $\phi_{SBH} = \phi_{graphite} - \chi_{Si}$ (Schottky-Mott approximation) and bromine intercalation of graphite increases the $\phi_{graphite}$, resulting in an increase in Schottky barrier height as displayed in Fig 4-6d. Greater difference in between Fermi level of the silicon and brominated graphite requires more electrons to flow from the semiconductor into the multi- layer- graphene, thus leaving a more positively charged region and an increase in the charge density within the W (Fig. 4-6b).

While J-V measurements are exponentially sensitive to the changes in zero bias Schottky barrier height (Eq. 4–1) and leads to a decrease in current density (Fig. 4-2),

associated changes in the charge distribution ($\rho(x)$) across the depletion width region, meaning an increase in the charge density, does not manifest itself. On the other hand, electrical field associated with the charge distribution ($\rho(x)$) in the *W* gives a finite capacitance at the multi- layer- graphene / semiconductor junction and therefore unlike *J-V*, capacitance measurements emphasize on the $\rho(x)$. Total capacitance at the interface derives from the solution to the Poisson's equation for specific charge distribution in the depletion width region and is written as,

$$\frac{1}{C^2} = \frac{2\,(V_{bi} + V_R)}{(eN_D\epsilon_s)} \tag{4–3}$$

and $C^{-2} - V_R$ plots yields a straight line with a slope of $-2/eN_D\epsilon_s$. Linear extrapolation to the intercept with the absiccsa corresponds to the built-in potential (V_{bi}) and Schottky barrier height can be expressed as $\phi_{SBH} = V_{bi} + (E_c - E_F)$, where E_c is the conduction band energy.

Fig. 4-7 displays measured capacitance at the multi- layer- graphene / *n*-silicon junction at room temperature at 1 KHz frequency in the form of $C^{-2} - V_R$. Before and after the bromine intercalation, *C-V* plots are found to be linear as predicted by Eq. 4–3. The intercept with the absicca, which is V_{bi}, typically spans around 0.40-0.60 eV corresponding to Schottky barrier heights of 0.54-0.74 eV before the intercalation (Fig. 4-7 red squares) and increases to 0.60-0.90 eV with Schottky barrier heights of 0.74-1.04 eV after the intercalation. The 0.3-0.4 eV increase in the Schottky barrier height (Fig. 4-7 red squares) roughly agrees with the changes in graphite work function measured by XPS (Fig. 4-5a-b). The slopes of the brominated multi- layer- graphene / silicon junctions are typically smaller by 2-6 times compared to pristine multi- layer-graphene / silicon junctions. The decrease in the slope, increase in N_D or charge density the depletion width, *W*, can be attributed to larger difference in between $\phi_{graphite}$ and χ_{Si} and hence more electron flow from Si into the multi- layer- graphene creating more positively charged region as discussed above. Solution to Poisson's equation at

the interface for increased charge density in the W leads to an increase in measured capacitance as illustrated in Fig. 4-7 inset.

4.3.5 Results on MLG / SiC Junctions and Sensing Applications

In this section, for completeness of this dissertation, the effects of bromine intercalation of multi- layer- graphene on the Schottky barrier characteristics of multi-layer- graphene / SiC junctions will be presented. Since the $J-V$ characteristics of the Schottky diodes are very sensitive to the bromination, changes of the measured current at fixed forward bias will be presented as a function of intercalation time to illustrate the possibility of sensing applications based on the multi- layer- graphene (or graphene) based Schottky junctions. Results presented on sensing applications are particularly interesting since graphene is particularly sensitive to different species atoms (not limited to bromine), and any interaction in between the graphene and various gases leads to a change in the Fermi level of the graphene. Therefore any interaction taking place in between various gases, molecules and macro molecules (DNA etc.) and graphene should display a large change in the $J-V$ characteristics as a result of change in barrier height and the number of ionized impurities with the depletion width. Combined with bond-polarization theory [1] and the Schottky-Mott model, these results suggest possibility of sensing application on graphene based Schottky junctions.

Changes in the doping level of the graphite with bromination, decrease in Fermi level (increase in graphite work function) and associated increase of ionized impurity concentration hence modification of the band diagram as shown in Fig. 4-6 have been discussed in the previous sections. Schottky characteristics of multi- layer- graphene / 4H-SiC diodes also show similar changes upon intercalation and can be explained by the changes in the Fermi level of graphite, modification of the band structure (Fig. 4-6) and increase in the barrier height. Within this picture, the current density is expected to drop drastically when the metal electrode (multi- layer- graphene) is brominated. The

$J-V$ characteristics of multi- layer- graphene / 4H-SiC junctions are displayed in linear and semilogarithmic forms in Fig. 4-8.

Based on the results shown in Fig. 4-2 and 4-8, the current measured across the Schottky diode is very sensitive to the bromine gas, meaning if the current is measured at fixed voltage with respect to time and bromine gas is turned on and off, one should observe a drastic drop in the current density. In Fig. 4-9, 1.85 V fixed voltage (forward bias) is applied across the multi- layer- graphene / 4H-SiC junction, and the current is recorded as a function of time. As seen in the figure shortly after the bromine exposure, the current across the junction goes down from 3.5 A/cm^2 to $\sim$0.7 A/cm^2. Even though this particular sample has shown five times current drop, on different samples more than an order of magnitude current drops have been achieved at different voltages or in reverse / forward bias directions. When the bromine gas is released in the chamber, the current starts to saturate eventually. The effect described above is semi-reversible, because when the bromine gas is pumped out of the chamber, the total current across the metal / semiconductor junction starts to increase but never reaches its original values. We attribute this effect to out gassing of bromine from multi- layer- graphene over time. Out gassing of various intercalants of graphite have been studied in the literature [54] and is beyond the scope of this dissertation, however intercalants are known to out-gas over time and eventually forming a *residue compound* of graphite. Therefore, the increase in the current density when the bromine gas is turned off can be attributed to the out-gasing of intercalants in between the graphene layers, and eventually some of the intercalant forms a residue compound. The intercalants forming residue compounds lower the Fermi level of the system as discussed in the previous sections, and lead to an increase in the barrier height and decrease in current density. Hence the current is expected to be lower than the original current density value (prior to the bromination). Upon further intercalation, the current density starts decreasing from 2.5A/cm^{-2} down to 0.4A/cm^{-2} consistent with the doping picture given above and

eventually saturating at another current density value (as a result of a residue compound with different stoichiometry) when the bromine gas is turned off for the second time.

These results presented above have significant implications in sensing molecules, gases and macromolecules. Since the formation of Schottky barrier at the metal / semiconductor junction is the most sensitive to the interface structure and the couple layers from the interface, these results are expected to be valid for graphene junctions as well. More importantly, since graphene is very sensitive to the environment and interaction of other molecules and charge transfer, the sensing application based on the $J-V$ characteristics at the graphene / semiconductor junctions are more likely to probe different gases and molecules.

4.4 Overview

In this chapter, we have demonstrated that the Schottky barriers formed at the multi- layer- graphene / semiconductor interface can be tuned by changing the work function of graphite $\phi_{graphite}$ by bromine intercalation. Sensitivity of Schottky diodes to bromine vapor is measured as an decrease in current density (*J*) in *J-V* and increase in capacitance (*C*) in *C-V* measurements. We attribute these changes to a decrease (increase) in Fermi level (work function) determined from the XPS and Hall measurements. Within the Schottky-Mott model an increase in the work function leads to an increase in the barrier height. This technique not only allows one to tune the barrier across the multi- layer- graphene / semiconductor interface using the same type of metal (in this case, multi- layer- graphene) by intercalation of semi-metal multi-layer- graphene electrode but also decreases the J_{rev} and improves the breakdown bias. In MESFETs and HEMTs where the characteristics of Schottky barriers are crucial, higher barrier heights are preferable due to larger gate-breakdown voltage, power gain and output resistance and lower gate leakage current and noise. Therefore, such results are particularly important for semiconductors which have no established native or ideal dielectric thus gating semiconductors is achieved through Schottky

barriers. Even though, this dissertation specifically focuses on bromine intercalation of graphite, an increase or decrease in Schottky barrier height can be achieved using other donor or acceptor type of intercalants such as K, Li, Ca, and I_2 [54]. Finally, these results open a new channel in integration of carbon electronics into semiconductors as well as applications such as sensing and tuning with different molecules, atoms and intercalants.

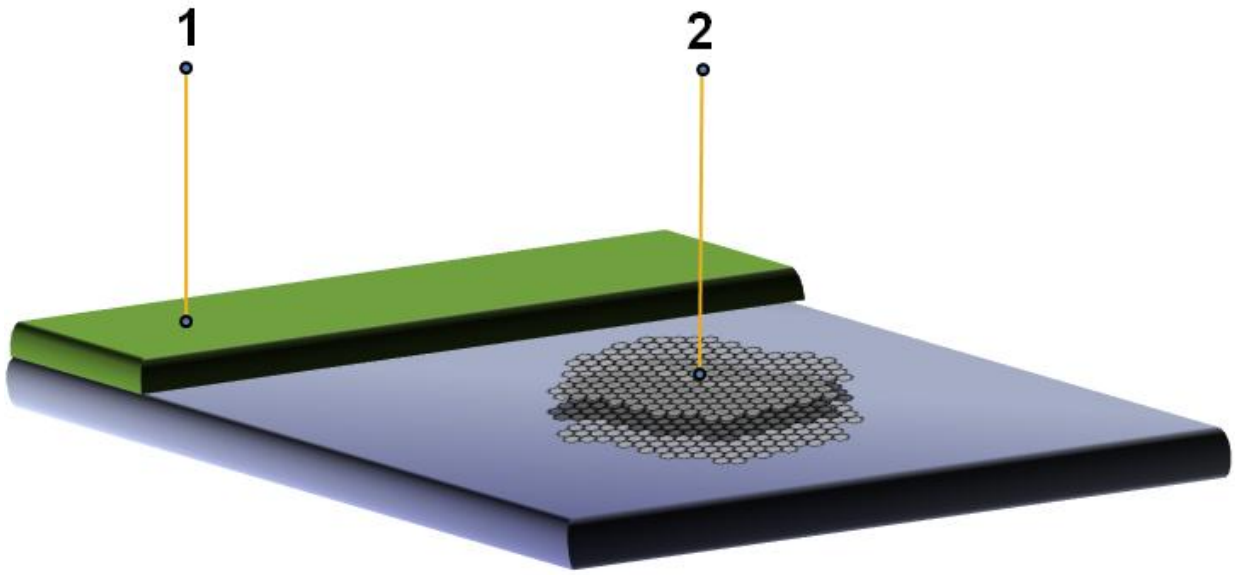

Figure 4-1. Schematics of multi-layer-graphene / *n*-Si($1E^{16}$cm$^{-}3$).

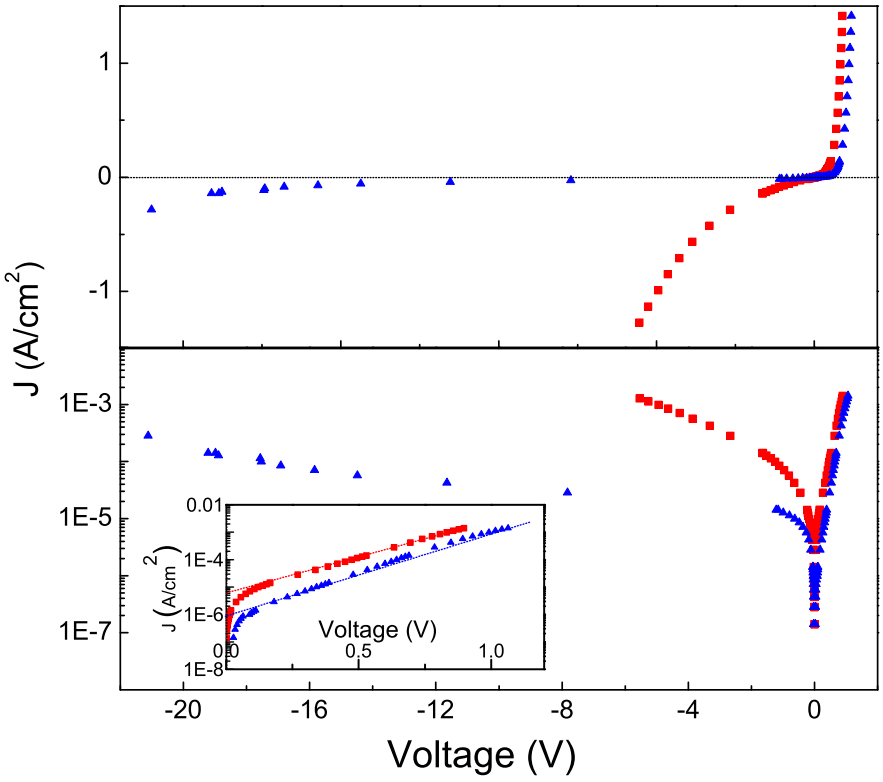

Figure 4-2. *J*-*V* plots on MLG / *n*-Si before (red squares) and after the bromination (blue triangles) in linear (top) and semilogarithmic scale (bottom) Inset: Forward bias $J - V$ plots.

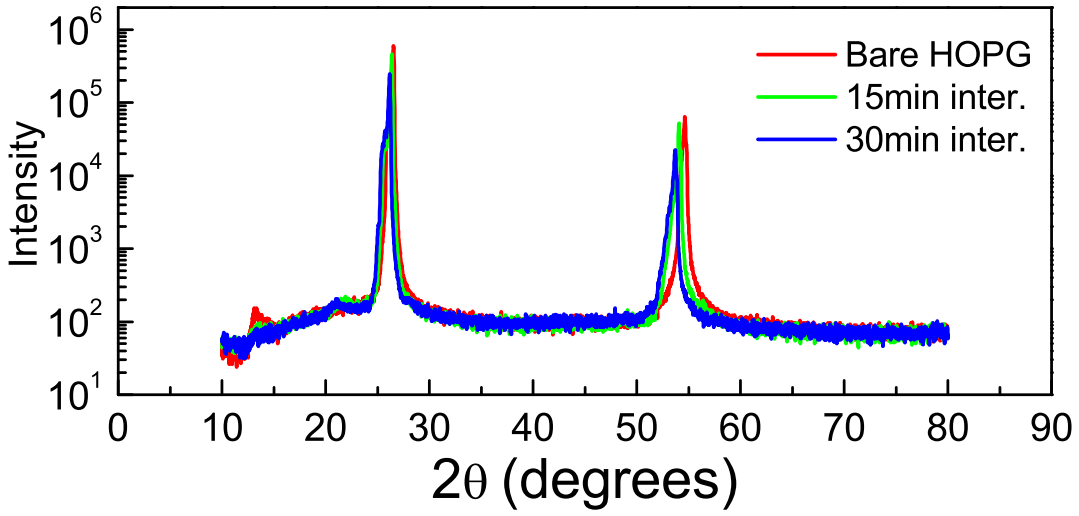

Figure 4-3. (a) X-ray photoelectron spectrum (XPS) of brominated graphite measured using monochromatized Mg X-ray source from 0eV up to 1100eV in a UHV chamber (b) C 1s measured by XPS on pristine (black solid lines) and brominated graphite (red and blue solid lines).

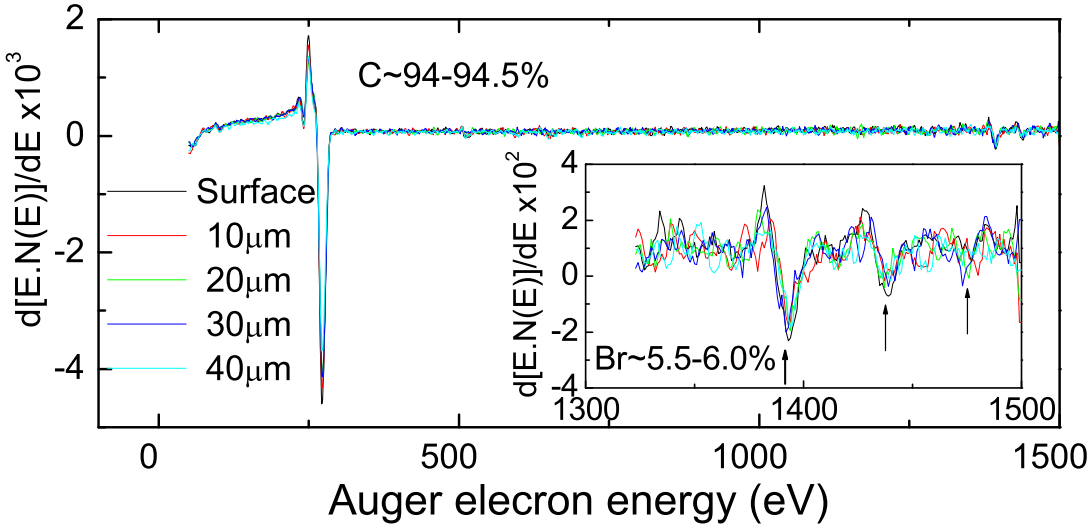

Figure 4-4. Auger electron spectrum (AES) taken on brominated graphite from 0eV up to 1500eV at different depths indicated in the legend. Inset: bromine Auger peaks located at 1396eV, 1442eV, and 1475eV corresponding to LMM Auger transitions

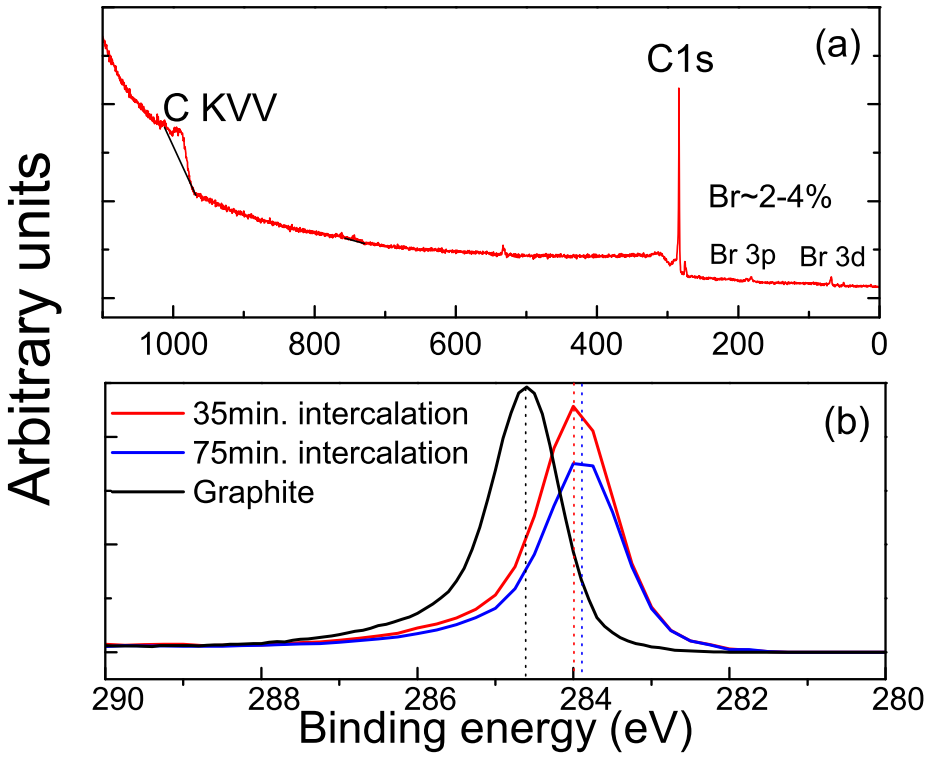

Figure 4-5. (a) XPS data of brominated HOPG sample (b) C1s peak of pristine (black solid lines) and brominated HOPG (red and blue solid lines).

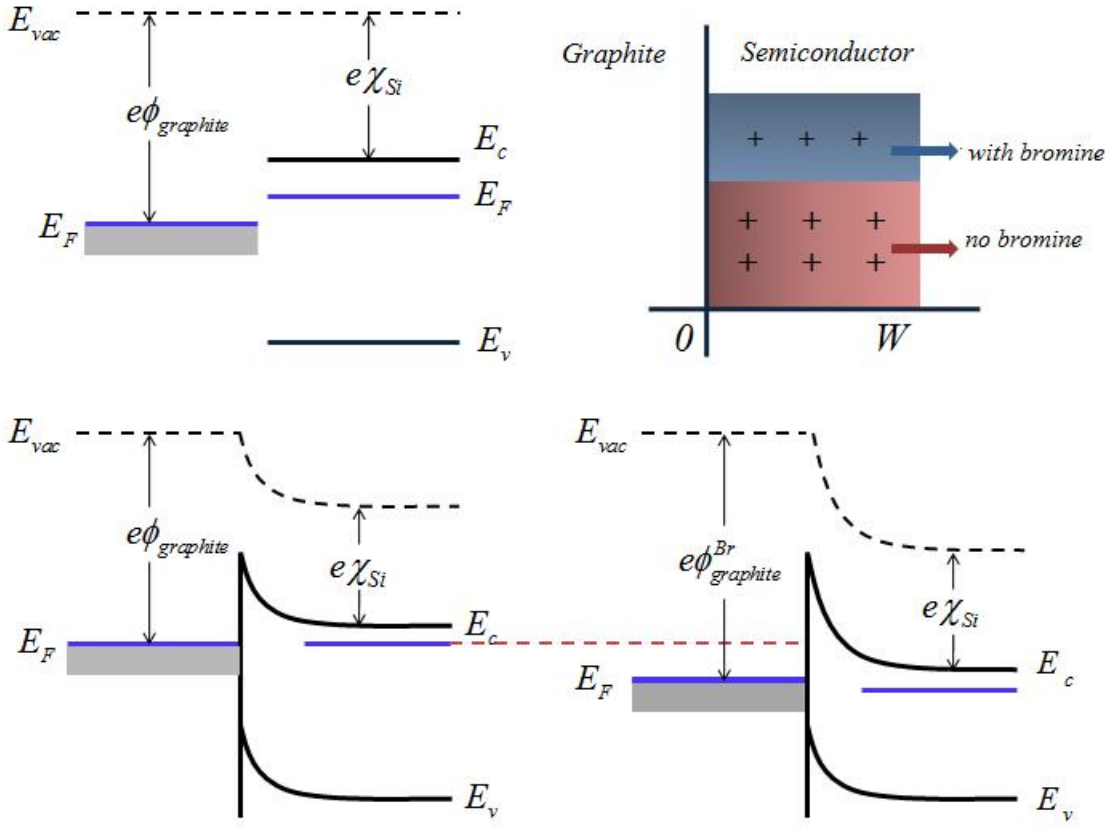

Figure 4-6. (a) Band structure at the metal-semiconductor interface before the physical contact and thermal equilibrium. (b) Change in charge distribution ($\rho(x)$) in the depletion width (*W*) before (red) and after (blue) the bromination. (c) Charge transfer and associated band bending, meaning Schottky barrier formation, at the interface after the physical contact made. (d) Change in Fermi levelm, band structure and Schottky barrier height (SBH) after the physical contact at the brominated graphite / semiconductor interface

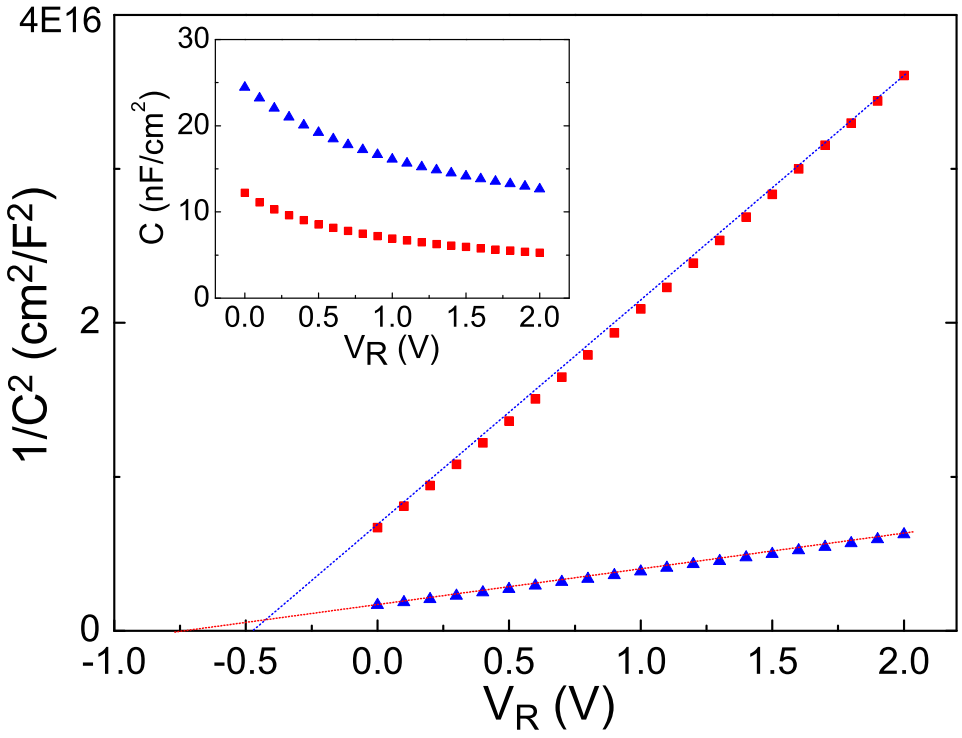

Figure 4-7. C^{-2} vs. V_R plots of MLG / *n*-Si(10^{16}cm^{-3}) substrates at 1KHz and 300 K before (red squares) and after the bromination (blue triangles). Inset: C vs. V_R plots

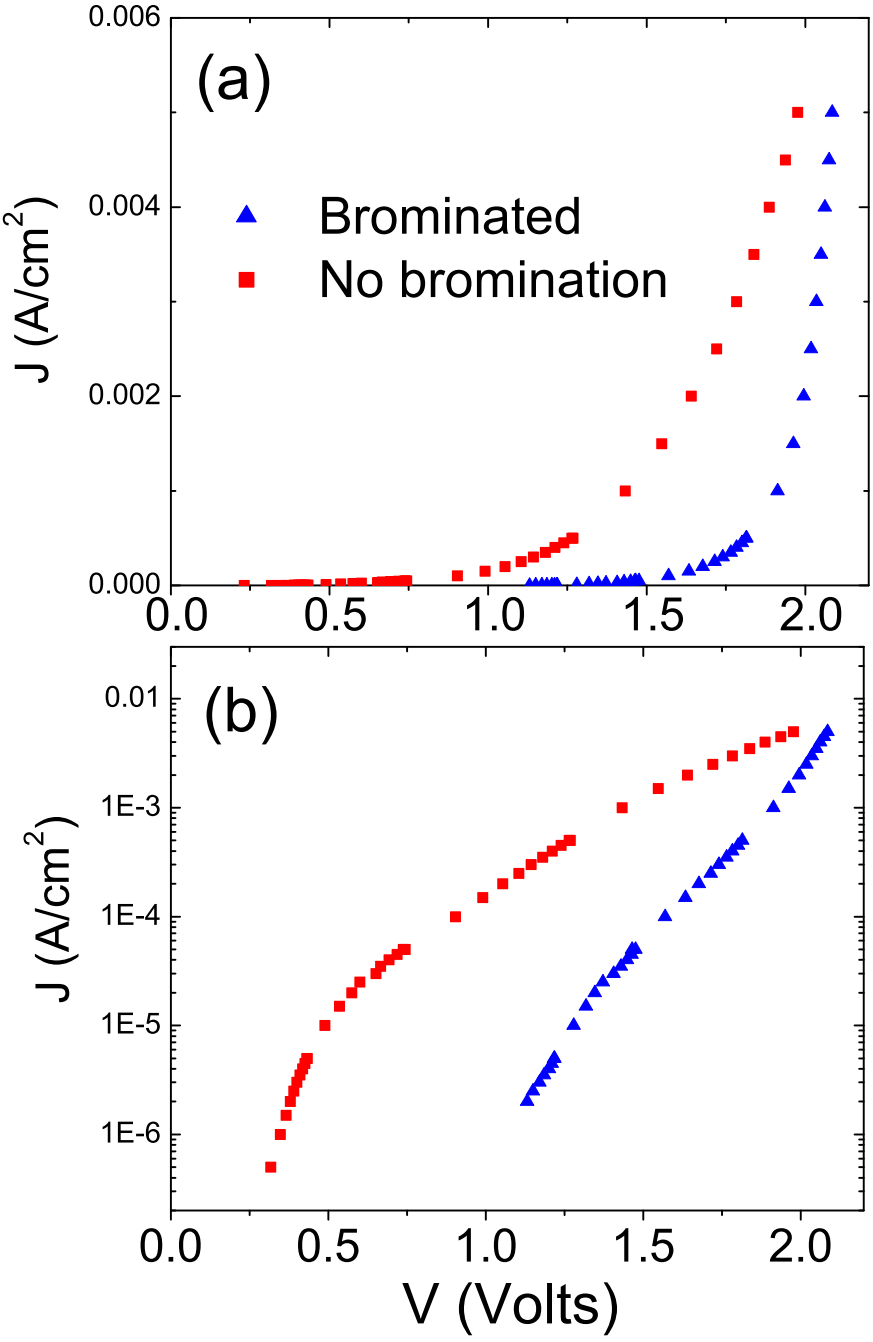

Figure 4-8. Room temperature current density, J, with respect to applied bias, V, on MLG / *n* - 4H-SiC before (red squares) and after the bromination (blue triangles) in linear (top) and semilogarithmic scale (bottom)

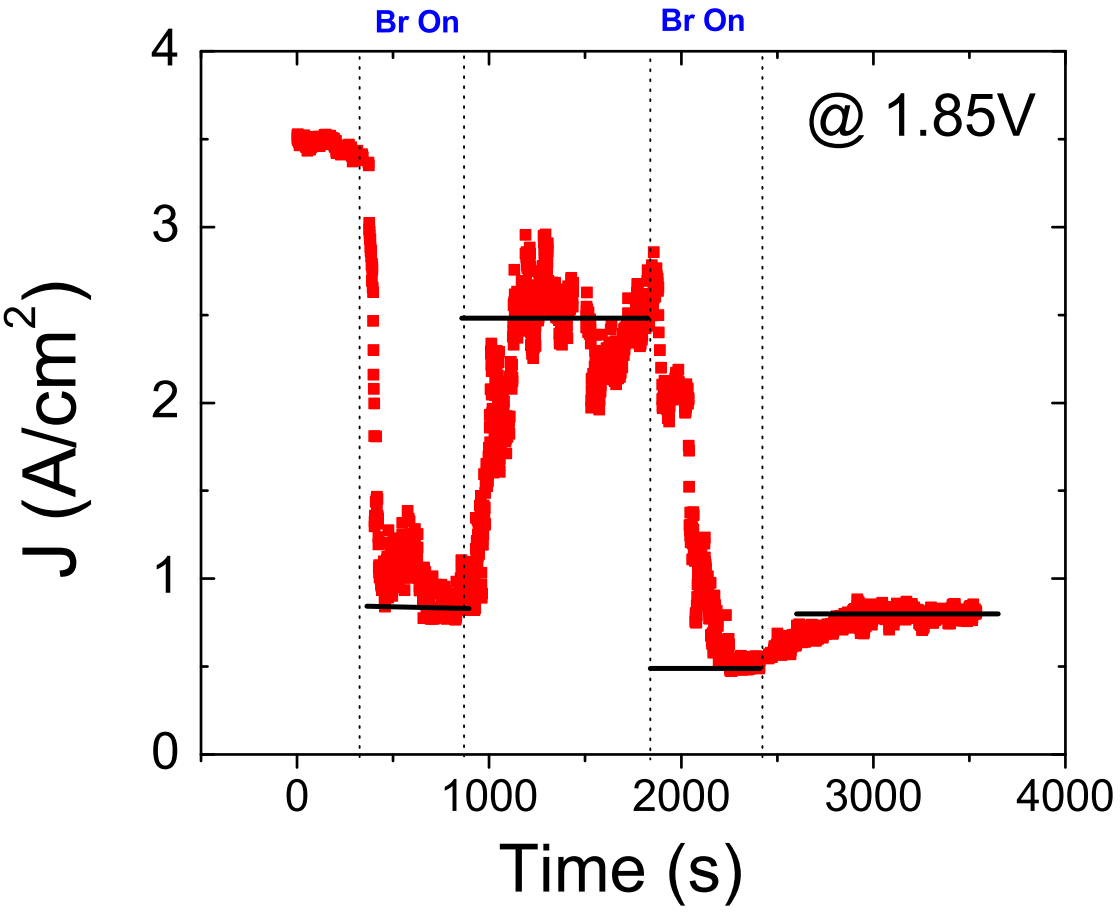

Figure 4-9. Plot of forward current at fixed voltage (1.85 V) with respect to the time. Bromine is turned on/off at specified times at the top of the graph.

CHAPTER 5
BAND STRUCTURE OF GRAPHITE

5.1 Introduction

Graphite is the most stable carbon allotrope. Carbon atoms in graphite crystal make three bonds (sp^2 hybridization) to the nearest neighbor carbon atoms, just like in many other forms such as carbon nanotubes (CNTs), graphene and C_{60} fullerene. Although graphite shares the same element and the same/similar bonding type, its electrical transport properties differ drastically from the other stable carbon based structures. Graphite is classified as a semi metal with finite overlap in between the conduction and valance bands with majority holes and electrons both contributing to the total current. Just like other typical semi metal materials such as bismuth (Bi), Antimony (Sb) and germanium telleride (GeTe), semi metals display very low density of carriers with Fermi level typically lower than room temperature (25.8 meV). In addition to these properties, graphite has a low cyctrotron mass (m_c) and is a very clean material with high impurity scattering times (τ_{imp}).Graphite can also be driven into the ultra-quantum regime at laboratory attainable magnetic fields and temperatures because of its low carrier density and light cyctrotron mass. Moreover, graphite consists of individually stacked graphene planes that are weakly coupled in Bernal (ABABAB) stacking. Since the adjacent layers of graphene are very weakly coupled, it displays high anisotropy in the electrical resistivity, with a resistivity rates $\rho_c/\rho_{ab} \approx 10^4$. Electronic transport in layered metals shows different behavior of the in-plane (ρ_{ab}) and out-of-plane (ρ_c) resistivities: while temperature dependence in ρ_{ab} (in plane) is metallic like, that of ρ_c (out-of-plane) is either non-monotonic or insulating like. This resistivity behavior is observed in different types of graphite, such as kish graphite, highly oriented pyrolytic graphite (HOPG), natural graphite [62], and other various metals such as layered perovskite Sr_2RuO^4 [63], high temperature superconductors [64] and organic metals [64].

The exotic properties of graphite have attracted a lot of attention in the literature in last five decades and a vast amouth of work has been done. During that period, the focus has been shifted to other allotropes of carbon: fullerenes [65] in 80s-90s, CNTs [66–68] in 90s-00s and recently graphene [42]. There are many questions left open or unanswered. However, in the last decade research on graphite has intensified after the discovery of single layer atomic sheet, graphene, and discovery of Dirac fermions [37], ferromagnetism [69, 70], quantum hall effect [71], intrinsic superconductivity [72], field driven metal-insulator transition [73, 74].

This chapter of this dissertation aims to give the reader an introductory idea about the theory background in graphite that will be used in the other chapters in the dissertation. An interested reader is encouraged to refer other sources and references in this chapter for detailed band theory of graphite.

5.1.1 Crystal Structure of Graphite and Graphene

Graphite consists of many graphene layers in which the carbon atoms are arranged in a hexagonal (honeycomb) network within each layer. In an ideal graphite, these layers are generally stacked in the ABAB sequence which is often referred as *bernal stacking*. This results in a hexagonal unit cell with lattice dimensions of c=6.73A and a=2.47A. The unit cell consists of 4 carbon atoms, as labeled by A,A',B and B' in Fig. 5-2. The Bernal stacking is known as stable and most common type of the graphite phase in the literature. In reality laboratory grown highly oriented pyrolytic graphite, naturally found graphite (natural graphite) and kish graphite samples display other minor phases. Another ordered and stable graphite phase is known to be rhombohedral graphite with ABCABC stacking (*rhombohedral stacking*). Due to its rhombohedral stacking, it belongs to different space group. Moreover, rhombohedral graphite phase has the same lattice constants as for Bernal phase with slightly larger graphene to graphene separation. Changes in the stacking order do not alter very strong nearest neighbor carbon-carbon bonding while it is different by 2-5% for the ext-to-nearest neightbor

coupling along the the c-axis. The binding energy per carbon atom or the total energy of these two phases differ slightly and nature favors Bernal stacking over rhombohedral stacking. In percentage terms, bernal phase consists most of the pristine graphite (97%) while the remainder is in rhombohedral phase (2.5%) and AAA stacking ($\sim$0.5%). These minority phases called as stacking faults in the literature and its effects on the transport properties and the bandstructure remain largely unknown [75].

Other than those phases changes, graphite is known to be one of the most highly anisotropic material known to man. The high anisotropy measured in graphite largely comes from the fact that the in- plane interatomic distance (nearest neighbor C-C distance) is 1.42 Åwhile the interplanar distance is 3.37Å. Within each carbon plane, graphene, carbon is arranged in hexagonally and the unit cell is described by 2 carbon atoms in a rhomb unit cell. The unit cell in-plane lattice constant is a=2.47Å. However, major graphite phase Bernal phase is stacked in ABAB fashion and in the unit cell of graphite there are 4 atoms with c=6.73Å. The resultant unit cell and the translational vectors of graphene and graphite are shown in Figs. 5-1 and 5-3 respectively.

The translation vectors of graphene, namely a_1 and a_2 (Fig. 5-1), can be written in orthonormal coordinates as follows,

$$\vec{a_1} = a\left(\sqrt{3}/2, -1/2, 0\right) \vec{a_2} = a\left(\sqrt{3}/2, 1/2, 0\right) \vec{a_3} = (0, 0, 1)\,, \tag{5–1}$$

where a is the distance in between neighest neighbor C-C distance, 1.42Å, and c is the lattice constant in the out-of-plane direction, 6.72Å. Using the translation vectors given in Eq. 5–1, the direct vector (D_n) and the reciprocal vectors (R_n) read as,

$$\vec{D_n} = (n_1\vec{a_1} + n_2\vec{a_2} + n_3\vec{a_3})\, \vec{D_n} = \left(a\sqrt{3}/2\,(n_1 + n_2)\,,\, a/2\,(n_1 + n_2)\,,\, cn_3\right), \tag{5–2}$$

and

$$\vec{R_n} = \left(m_1 \vec{b_1} + m_3 \vec{b_2} + m_3 \vec{b_3} \right), \tag{5–3}$$

Here $\vec{b_{1,2,3}}$ are the reciprocal lattice basis vectors derived from the translation vectors $\vec{a_{1,2,3}}$ by

$$\vec{b_1} = \frac{2\pi}{a}\left(\frac{1}{\sqrt{3}}, -1, 0\right) \vec{b_2} = \frac{2\pi}{a}\left(\frac{1}{\sqrt{3}}, 1, 0\right) \vec{b_3} = \frac{2\pi}{c}(0, 0, 1), \tag{5–4}$$

Therefore the reciprocal lattice also shares the same symmetry as direct lattice and the first Brillouin zone can be described as in Fig. 5-4.

Each carbon in graphite or in individual graphene sheets makes three nearest neightbor bondings or sp^2 hybridization. Therefore there of four valance electrons are involved in the σ bonds while the last valence electron participates in the π bonding. The four carbon atoms in the unitcell of graphite involves total 16 valance electrons that correspond to 16 bonding of which 8 of them are bonding and the other 8 are anti-bonding energy states. On the other hand, total number of valance electrons in the unit cell of graphite that are involved in the σ bonding add up to 12. Those electrons create 6 bonding and 6 anti-bonding energy levels and they are roughly separated by 5.1 eV and do not cross the Fermi level. The 3 valence electrons (in each carbon atom) involved in the σ bonding, do not contribute to the electronic properties of the graphite. The other 4 valence electrons in the unitcell that are participating to the formation of π bonds are on the other hand gives 4 energy levels and those bonding and anti-bonding states lie around the Fermi level of the system. It is therefore, the valence electrons involved in the π bonding which contribute to most of the transport properties of graphite. The upper and lower π bands overlap by 30 meV along the Brillouin zone boundaries (through HKH, H'K'H' symmetry points) (Fig. 5-4) creating its signature semi-metallic properties: Both electrons and holes contributing to the transport with order of similar mobilities (4000cm^2/V.s for holes and 6000cm^2/V.s for electrons) and effective masses (0.3 m_0 for electrons and 0.5 m_0 for holes).

5.1.2 Band Structure:Energy Spectrum of Electrons / Holes in Graphite

The electronic properties of graphite are well explained by Slonzewski, Weiss and McClure (SWMc) theory. The details of the theory demand separation discussion and are beyond the scope of this chapter. However, the interested reader is encouraged to read SWMc's original article given by reference [76, 77]. Nevertheless, the physical parameters used in the theory and the later in the dissertation as well as some preliminary steps might be necessary to understand the physics behind graphite.

The SWMc theory uses a total of 7 different parameters describing the interaction in between carbon atoms in the graphite matrix and determines the dependence of the energy spectrum on the wavevector by using the crystal symmetry as a tool. Therefore, SWMc theory is considered as a phenomenological treatment to predict band structure of the graphite. The parameters used in the SWMc model are listed in Table 5-1.

Under the assumption that the γ_3 parameter is zero, the secular equation for the hamiltonian of the system can be solved exactly. Here the assumption (γ_3=0), reduces fourth order equations to second order equations and allows one to obtain the four branches of the spectrum as,

$$\epsilon_1^{\pm} = \frac{1}{2}\left(\epsilon_1^0 + \epsilon_3^0\right) \pm \left[\frac{1}{4}\left(\epsilon_1^0 - \epsilon_3^0\right)^2 + \nu_\rho^2 k_\rho^2 \left[1 - \frac{\gamma_4}{\gamma_0}\Gamma\right]^2\right]^{1/2}, \tag{5–5}$$

and

$$\epsilon_2^{\pm} = \frac{1}{2}\left(\epsilon_1^0 + \epsilon_3^0\right) \pm \left[\frac{1}{4}\left(\epsilon_1^0 - \epsilon_3^0\right)^2 + \nu_\rho^2 k_\rho^2 \left[1 + \frac{\gamma_4}{\gamma_0}\Gamma\right]^2\right]^{1/2}, \tag{5–6}$$

Here, ϵ_2^+ and ϵ_1^+ correspond to the majority and minority electrons while ϵ_1^- and ϵ_2^- correspond to majority and minority holes. The resultant band diagram is sketched near the HK high symmetry points in Fig. 5-5. In the diagram, the 4 π energy bands are labeled as E_1, E_2 and doubly degenerate (along the zone edges) E_3 bands. E_1 band displayed in Fig. 5-5 is an empty band while E_2 band barely crosses the Fermi level

at the H point of the Brillouin zone creating minority holes. This band displays almost linear spectrum at this high symmetry point and the dirac-like properties sometimes observed in pristine graphite are attributed to these minority carriers[37]. The doubly degenerate E_3 band is partially occupied in between H-K symmetry points and gives rise to majority electron and hole pockets as displayed in Fig. 5-5 and in the H-K zone boundary in the Brillouin zone (Fig. 5-4). Reader is kindly reminded that this band structure is calculated within some approximations and the γ_3 coupling parameter described in Table. 5-1 is set to zero for exact solution to the secular equation. This mild approximation defines the Fermi surface as cylindrical and the cylindrical symmetry automatically breaks down for non-zero γ_3 couplings. For non-zero γ_3, the hole and electron pockets along the HKH (or H'K'H') symmetry points start touching from 4 different points (forming legs). This effect is typically called as a *trigonal warping of graphite* and the effect of this coupling parameter on the bandstructure of graphite has been studied in the literature. The interested reader is advised to review the central ideas and the references therein [78, 79].

For the completeness of this chapter, it is important to discuss the limit when γ_2 or γ_2 and γ_1 is taken as zero. When the coupling in between two B atoms from the nearest equivalent layers (γ_2) is taken zero, the energy spectum can also be calculated by tight binding approximation [80] consistent with the SWMc prediction and expressed as,

$$\epsilon = \pm\frac{1}{2}\Gamma \pm \left[\frac{\Gamma^2\gamma_1^2}{4} + \nu_\rho^2 k_\rho^2\right]^{1/2}, \tag{5–7}$$

In this limit where all the coupling parameters γ_i i=2 and higher are set to zero, graphite interacts only with the adjacent graphene layer and this regime is called *bi-layer graphite regime*. Here, when the γ_1 parameter is set to zero as well each graphene layer are isolated from each other and the energy spectrum reduces to the Dirac spectrum given by $\epsilon = \pm\nu_\rho k_\rho$.

Table 5-1. Values and description of the parameters used in SWMc model

Coupling parameters	Description	Values
γ_0	Interaction in between the nearest neighbor carbon atoms in a plane	∼3.2eV
γ_1	Interaction in between two nearest A carbon atoms next to the consecutive layer	∼0.4eV
γ_2	Interaction in between two carbon atoms B from nearest equivalent (not consecutive) layers (determines Fermi level of the system)	∼0.02eV
γ_3	Interaction in between carbon atom A with the atom B in the neighboring layer	∼0.3eV
γ_4	Interaction in between atom A in one layer to the nearest atom A in the neighbor layer	∼0.1eV
γ_5	Interaction in between atom A in one layer to the nearest atom A in the nearest equivalent layer	∼0.01eV
γ_6 or Δ	Difference in crystalline experienced by inequivalent carbon sites in layer planes.	∼0.01eV

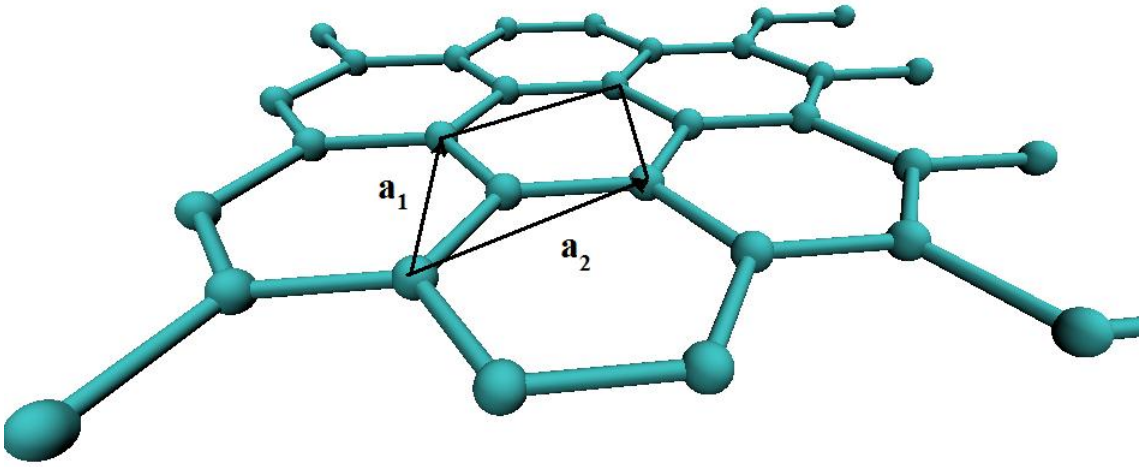

Figure 5-1. One unit cell of graphene with translational vactors a_1 and a_2

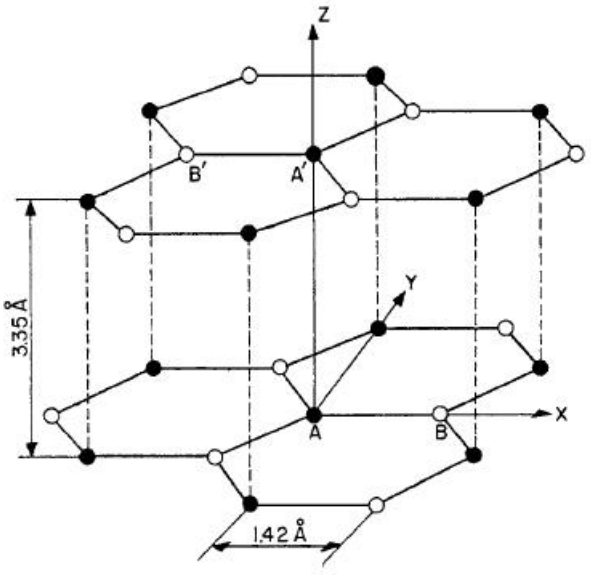

Figure 5-2. Crystal structure of graphite showing consecutive layers with A B and A' B' atoms.

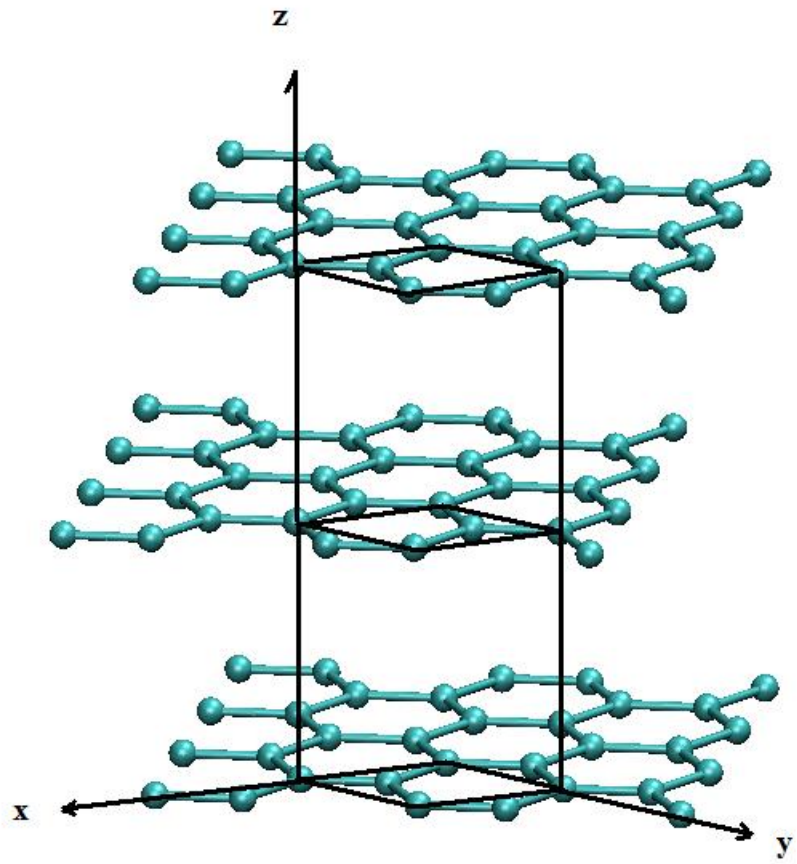

Figure 5-3. One unit cell of graphite with translational vactors a_1 and a_2 and c

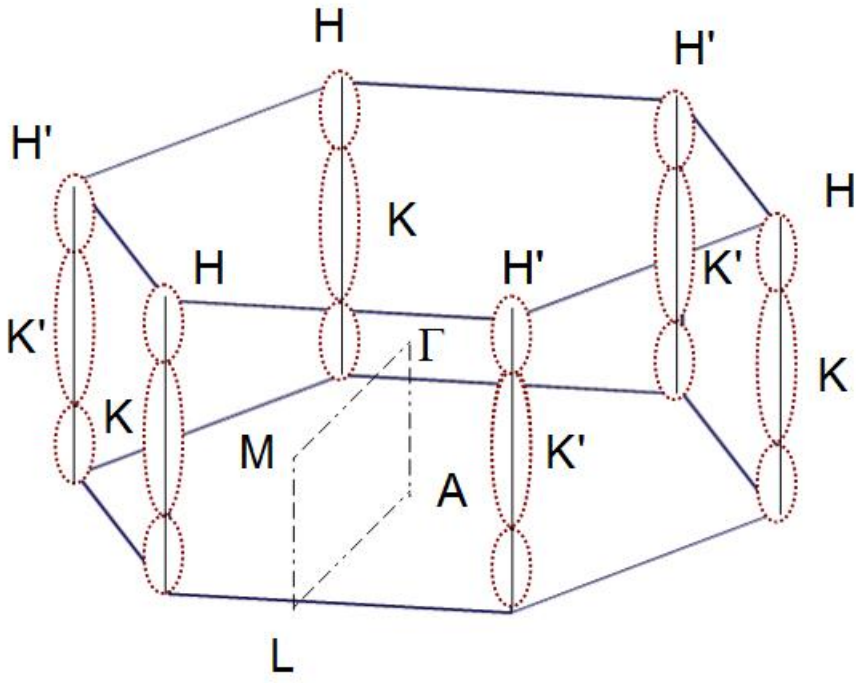

Figure 5-4. The first brillouin zone of graphite. Electron and hole pockets are cylindrically positioned along the HKH and H'K'H' high symmetry points with finite overlap which is comparable to γ_2=0.02eV

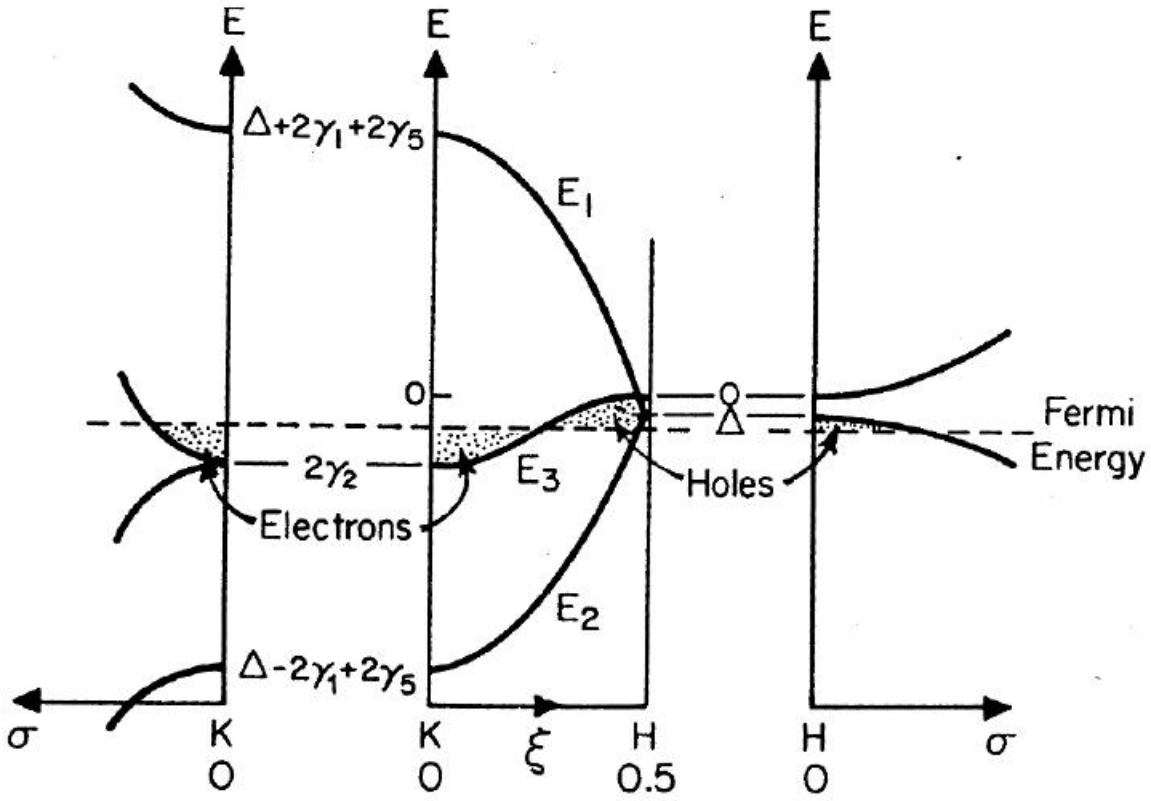

Figure 5-5. The band structure of graphite near the high symmetry points H-K (or H'-K') as calculated from SWMc model.

CHAPTER 6
TRANSPORT PROPERTIES OF HIGHLY ORIENTED PYROLYTIC GRAPHITE (HOPG) FROM 3K UPTO 1500K

6.1 Introduction

The family of carbon allotropes includes fullerenes, carbon nanotubes, graphene, graphite, and diamond. A combination of chemical simplicity and diverse physical properties, characteristic for these materials, makes carbon-based electronics a promising field of research and application. Surprisingly, the most common member of this family, graphite, has been very active field of research in the last decade after observation of dirac fermions [37], ferromagnetism [69, 70], quantum hall effect [71], intrinsic superconductivity [72], field driven metal-insulator transition [73, 74]. These recent findings observed on traditional and 'well known' material graphite raised many questions and are still under debade and yet to be explained both experimentally and theoretically. Nevertheless, these findings all implied that physics of graphite is not as simple as it was thought and there are in fact more unknown aspects to it rather than known.

The transport properties of graphite have been measured more than five decades from low temperatures up to room temperature on various quality and types of graphite including kish, natural and pyrolytic graphite. The quality of the laboratory grown graphite was very poor till 70s and after 80s highly oriented pyrolytic graphite with very little impurity content as well as very minuscule mosaic spread became available. Prior to successful HOPG growth, samples sizes were very small and thus reliable experimental results on out-of plane resistivity properties were not possible. Moreover, the resistivity properties were also dependent on the part of the natural/kish/pyrolytic graphite that the samples were cut from. Despite those fundamental differences in their resistivity properties, the in-plane transport properties of various types of graphite have shown something in common: metallic temperature dependence from 1.7 K up to room temperature. The metallic temperature dependence of ρ_{ab} explained within the Drude

like picture derives from the competition in between temperature dependence of number free carriers and the scattering times. However, the transport properties of graphite at temperatures higher than the Fermi level of the system have not been studied. This not only offers a fruitful physical regime since most metals evaporate before the temperatures comparable to their Fermi level values (order of couple eV) are reached but also is necessary to understand properties of graphite since graphite (or graphene) - semiconductor junctions operate even at high temperatures and is of technological importance.

This chapter of the dissertation, aims to explain the in-plane transport properties (ρ_{ab}) of highly oriented pyrolytic graphite (HOPG) from 1.7 K up to 900 K and out-of plane transport properties (ρ_c) from 1.7 K up to 1300 K. All the experimental results presented in this dissertation belong to the author of this dissertation, however all the interpretation and theoretical explanations are result of collaboration with Prof. Dr. D.Maslov, Dr. D. Gutman and doctorate student H.K. Pal [38].

6.2 In-Plane Transport (ρ_{ab}) from 1.7 K up to 900 K

6.2.1 Experimental Details

The samples measured in this chapter are supplied from Dr. Fischer (UPenn) and all HOPG samples were identified to have 0.5 degree mosaic spread determined by X-ray rocking curve measurements. All the HOPG samples displayed high anisotropy (ρ_c/ρ_{ab}) reaching up to 10^3-10^4 with typical graphite room temperature resistivity values (ρ_c $\sim$30mΩ·cm and ρ_{ab} $\sim$30$\mu\Omega$·cm). The samples have been cut in proper dimensions using diamond impregnated wire. After the dicing, samples has been cleaved by conventional micro cleavage method [42] until smooth and clean surfaces are exposed. The electronic properties have been measured from 1.7 K up to 300 K in a physical property measurement system (PPMS) at zero magnetic field in four terminal contact configuration using LR-700 16Hz AC resistance bridge. The contacts are made to the sample either using high temperature silver paint or home-made graphite paint. The

results presented in this chapter are independent of the type of the paint used. The high temperature measurements are done in a home made vacuum oven under high vacuum ($\sim 10^{-6}$ Torr) or in a nitrogen flowing gas. The room temperature resistivity was measured to be $\rho_{ab}^{300K} \approx 32\ \mu\Omega$·cm before and after annealing, consistent with the existing literature values. Since ρ_{ab}^{300K} remains at the same value before and after annealing, we conclude that adsorption/desorption of impurities or doping does not occur up to 900 K. In addition to this observation, X-ray photoelectron spectroscopy (XPS, Fig. 6-1a) and Auger electron spectroscopy (AES, Fig. 6-1b) were performed on different samples and contamination was not observed. The XPS and AES spectra displayed respectively a characteristic C_{1s} peak at 284.6 eV and a C auger peak at 271.8 eV. The shape and position of the XPS C_{1s} peak was unaltered indicating that C remained in the same chemical state (Section 4.3.3). The sample temperature has been recorded using cernox and platinum thermocouple in PPMS and K-type thermocouple in the vacuum oven at a close proximity to the sample (1mm). Typical temperature dependence of the in-plane resistivity of HOPG is displayed in Fig. 6-2

Reproducibility of the results was checked by superimposing the temperature - dependent resistivities of two separate samples (Fig. 6-2 black and red data points). Reproducibility of the measurements was also checked by sweeping the temperature up and down in the range $1.7\ \text{K} \leq T \leq 900$ K and no significant temperature lagging effect was observed.

6.2.2 In-Plane Transport from 1.7 K up to 300 K: Drude Formula

The temperature dependence of ρ_{ab} in HOPG is metallic like from 1.7 K up to the room temperature (Fig. 6-2). The in-plane resistivity shows no significant temperature dependence at temperatures lower than 6 K. At this temperature range, total resistivity is due to the impurity scattering and the total scattering time τ is expected to be temperature independent (τ_{total}=τ_{imp}). Above 6 K, in-plane resistivity increases with temperature and shows a sign of saturation around room temperature. In-plane

transport mechanism in pristine graphite is essentially governed by the classical theory (Drude formula) $\sigma_{xx} = \frac{ne^2\tau}{m^*}$, which is competition in between temperature dependent mobility (μ) and carrier concentration (n). The temperature dependence of mobility, scattering time and carrier concentration have been previously exacted out from the measured ρ_{xx} and ρ_{xy} in the low magnetic field region (0.2 Tesla) [73] and the temperature dependence of these parameters are shown in Fig. 6-3. Black and red data points correspond to majority electron and hole carriers while the blue data points represent the minority hole carriers with Dirac-like spectrum (Chapter 5). Electron-phonon scattering decreases drastically below $\sim$70 K and the mobility is expected to increase by factor of 5 times while it is less temperature dependent at temperatures higher than 70K. As mentioned above, the minority hole band (blue data points in Fig. 6-3) has Dirac-like features and hence has much larger mobilities comparing to the mobility of majority band carriers (black and red data points) but possess the same temperature dependence due to the nature of the electron-phonon scattering. After discussing the temperature dependence of the scattering times, the temperature dependence of the carrier concentration is necessary to understand the temperature variation of ρ_{ab} using the Drude formula. In principle, in a regular metal where the Fermi level is on the order of couple eVs, the carrier concentration is not expected to be temperature dependent at those temperatures. However, the low Fermi energy ($\sim$300 K) in graphite makes the carrier concentration a strong function of temperature as seen in Fig. 6-3. Carrier concentration increases with the temperature by $\sim$4-5 times from 5 K up to $\sim$70 K and it becomes less temperature dependent above. The combination of temperature dependence of the mobility and number density, gives a slowly varying resistivity in between 70 K-300 K range while it decreases drastically below 70 K as observed in Fig. 6-2 and becomes temperature independent below 6K.

6.2.3 In-Plane Transport from 300 K up to 900 K

The in-plane transport properties of HOPG in the 1.7 K - 300 K range can be explained within the simple Drude formula. However, at temperatures much higher than room temperature, two striking differences in the material fundamental properties appear: (1) temperatures become comparable to or larger than the Fermi level of the graphite and this temperature range identifies a new transport regime and (2) all the higher order coupling parameters other than γ_0 and γ_1 become negligible since their energies are less than 300K. When graphene layers are interacting by only γ_0 and γ_1 coupling parameters, graphite can be pictured as *bi-layer graphite* (BLGT). The band overlap in between the conduction and the valance band comes from the $gamma_2$ coupling (Chapter 5) and in this limit, meaning when γ_2 coupling is negligible, graphite becomes zero band gap semiconductor with zero overlap between conduction and valence bands. Prior transport measurements of graphite were performed at or below 300 K, where it behaves as a compensated semi-metal with finite Fermi energy. There is, however, a very interesting but hitherto unexplored regime of temperatures, $E_F \lesssim T \lesssim \gamma_1 \approx 4060$ K. This regime can be viewed as a critical region of the transition from a semi-metal with finite band overlap to a semiconductor with finite band gap. If slanted hopping (γ_3) is also neglected, BLGT is described by a simple (and historically the first) Wallace model of graphite [80], which contains only two hoppings: γ_0 and γ_1. The energy spectrum in this model consists of two electron and two hole branches,

$$\varepsilon_{\mathsf{k}} = \pm\gamma_1\Gamma \pm \sqrt{\gamma_1^2\Gamma^2 + \gamma_0^2|S|_{\mathsf{k}}^2}, \tag{6–1}$$

where $\Gamma = \cos(k_z c/2)$, c is the c-axis lattice constant and S_{k} is structure factor for hopping between inequivalent (A and B) atoms.

When all the higher order couplings are ignored, but $\gamma_{0,1}$, the Fermi energy of the system reduces to zero and density of states, $\nu \sim \gamma_1/v_0^2 c$, becomes independent of temperature. On the other hand, the Fermi function scales linearly with temperature

when E_F=0 eV and there density of carriers, $n = \int \nu f(\epsilon) d\epsilon$, also scales linearly. Using the Drude formula, the in-plane conductivity scales as (up to $\mathcal{O}(\varepsilon/\gamma_1)$ terms),

$$\sigma_{ab} = (4 \ln 2/\pi) \left(e^2/c\right) T\tau. \tag{6–2}$$

When the temperature is higher than the Fermi energy of the system, $1/\tau$ scales linearly with temperature and the conductivity saturates. The computed values of resistivity from this simple model are given in Fig. 6-4 with blue dashed lines.

The experimental results for $\rho_{ab}(T)$ are presented in Fig. 6-4 as points. Note that the tendency to saturation pronounced at $T \sim 300$ K is superseded by a rapid increase which continues unabated up to the highest temperature measured. The dashed line in the Fig. 6-4 shows the theoretical prediction for $\rho_{ab}(T)$, calculated for $1/\tau = 1/\tau_0 + \alpha T$ and for a realistic energy spectrum of carriers. While this model describes the experiment at low temperatures, it fails completely for $T > 300$ K. A slow increase in the theoretical curve, which amounts only for a $\sim 12\%$ increase of ρ_{ab} from 300 to 900 K, is due to corrections of order T/γ_1 to Eq. (6–2).

Before proceeding with a discussion of such mechanisms, it is instructive to develop a more intuitive picture of transport in BLGT. To this end, we replace the Wallace spectrum by a massive (Galilean) form obtained by expanding Eq. 6–1 in $k_{||} \equiv \sqrt{k_x^2 + k_y^2}$ and keeping only the degenerate branches of electrons and holes:

$$\varepsilon_{\mathrm{k}}^{\pm} = \pm k_{||}^2/2m_{||}(k_z), \tag{6–3}$$

where $m_{||}(k_z) = \Gamma\gamma_1/v_0^2$ is the k_z-dependent mass of the in-plane motion. Evaluating the in-plane conductivity as

$$\sigma_{ab}(T) = 4e^2 \int d^3k \left(-\partial f_{\mathrm{k}}^0/\partial\varepsilon_{\mathrm{k}}\right) v_{||}^2 \tau(\varepsilon_{\mathrm{k}}, T)/(2\pi)^3 \tag{6–4}$$

with spectrum (6–3), $\tau = \mathrm{const}$, and $f_{\mathrm{k}}^0 = 1/(\exp(\varepsilon_k/T) + 1)$, we reproduce Eq. (6–2).

Typical momenta contributing to σ_{ab} are $k_z \sim 1/c$ and $k_{||} \sim k_T \equiv \sqrt{2\bar{m}_{||} T}$, where $\bar{m}_{||} \equiv m_{||}(k_z = 0) = \gamma_1/v_0^2$. Although expansion in $k_{||}$ breaks down near the H points ($k_z = \pm\pi/c$), where Γ vanishes and the spectrum is Dirac-like, the contribution of Dirac fermions to σ_{ab} is small in proportion to the volume of the Brillouin zone they occupy.

Therefore, a typical carrier (in zero magnetic field) in BLGT is massive rather than Dirac-like and the isoenergetic surfaces are corrugated cylinders centered near the K points. As in the case of bi-layer graphene [78, 81, 82], γ_3 hopping (responsible for trigonal warping of the isoenergetic surfaces) leads to a linear-in-$k_{||}$ term in the energy spectrum, which is smaller than the quadratic term for energies $> \gamma_1\gamma_3^2/\gamma_0^2 \sim 30$ K. Since we are not interested here in special effects arising solely from trigonal warping, meaning longitudinal magnetoresistance, this term can be safely neglected.

As discussed in Chapter 5, graphite contains four atoms in a unit cell and with three degrees of freedom that results in total twelve modes in which 3 of are acoustic and the remaining nine modes are optical phonon modes. The phonon spectrum consists of two groups of modes: “hard”and “soft” [83]. The characteristic energy scale of hard modes, which are present already in graphene, are on the order of ~ 0.1 eV. On the other hand, soft modes, with typical energies of order 10 meV, arise from weak coupling between graphene sheets. For the temperatures of interest ($T > 300$ K), all soft modes are in the classical regime, in which the occupation number and, thus, the scattering rate scale linearly with T as discussed above. Although hard acoustic modes are still below their Debye temperatures, they are also in the classical regime. For example, typical in-plane phonon momenta involved in scattering at a hard, graphene-like acoustic mode with dispersion $\omega_A = s_{ab} q_{||}$ are $\bar{q}_{||} \sim \bar{k}_{||}$. The corresponding frequencies $\bar{\omega}_A \sim s_{ab}\bar{k}_{||}$ are smaller than T as long as $T \gg \bar{m}_{||} s_{ab}^2 \sim 1$ K. Therefore, all soft modes as well as hard acoustic modes lead to linear scaling of the scattering rate $\tau_{\mathrm{e-ph}}^{-1} = \alpha T$ and do not account for the experimental observation in Fig. 6-4.

Switching briefly to another scattering mechanism–electron-electron interaction–we notice that although $1/\tau_{e-e}$ due to this mechanism scales as T^2 for $T < E_F$, this scaling does not hold at higher T. In fact, the screened Coulomb potential in BLGT does not practically depend on the in-plane momentum transfer and can be regarded as a constant, while the number of carriers scales linearly with T. Consequently, $1/\tau_{e-e} \propto T$. This linear scaling persists even at higher temperatures ($T \gtrsim \gamma_1$), in the single-layer limit [84]. Therefore, neither scattering at phonon modes in the classical regime nor electron-electron interaction provides an explanation of the experiment. On the other hand, the remaining hard modes are graphene-like optical phonons, such as the longitudinal optical (E_{2g}) mode with frequency $\omega_0 \approx 0.17$ eV at the Γ point [83, 85]. For $T \lesssim \omega_0$, scattering at these modes leads to an exponential growth of the resistivity with temperature. The remainder of this chapter will focus on explaining the experimental results ($\rho_{ab}(T)$) without going in to the theoretical details which can be found elsewhere [38].

By constructing a very simplified model for the interaction between longitudinal phonons and electrons, of the matrix of the tight binding Hamiltonian elements are calculated and the corresponding scattering times are evaluated. The finalized scattering time can be expressed as,

$$\tau_{iv}^{-1}(\varepsilon_k, T) = \bar{\tau}^{-1} \frac{\coth(\omega_0/2T)\cosh^2(\varepsilon_k/2T)}{\cosh^2(\varepsilon_k/2T) + \sinh^2(\omega_0/2T)}, \tag{6–5}$$

where all model-dependent details of the electron-phonon interaction are incorporated into $\bar{\tau}^{-1}$. For a thermal electron ($\varepsilon_k \sim T$) the scattering rate behaves as $\exp(-\omega_0/T)$ for $T \ll \omega_0$. For $T \gg \omega_0$, scattering at this mode crosses over into the classical regime and $\tau_{iv}^{-1} \sim T/\omega_0\bar{\tau}$.

At sufficiently high temperatures, where intervalley scattering is the dominant mechanism, the conductivity is obtained by substituting $\tau_{iv}(\varepsilon_k, T)$ into Eq. (6–4), and this results in,

$$\sigma_{ab}^{(\mathrm{iv})} = \left[\left(4\ln 2 - 1\right)/3\pi\right]\left(e^2/c\right)\, T\bar{\tau}\exp\left(\omega_0/T\right)\ , \tag{6–6}$$

Based on this result, we fit $\rho_{ab}(T)$ by

$$\rho_{ab} = \left(\frac{1}{\tau_0} + \alpha T\right)\frac{1}{\varepsilon^*} + \frac{c}{e^2}\frac{1}{a_0 T\bar{\tau}}\exp\left(-\frac{\omega_0}{T}\right), \tag{6–7}$$

where $a_0 = 2\left(4\ln 2 - 1\right)/3\pi \approx 0.376$ and $\varepsilon^* \equiv c\int d^3k v_{||}^2\left(-\partial f_{\mathrm{k}}^0/\partial\varepsilon_{\mathrm{k}}\right)/8\pi^2$.

When calculating ε^*, we account for hopping between next-to-nearest planes, described by $\gamma_2 \approx 0.02$ eV. The first term in Eq. (6–7) accounts mostly for the low-T behavior of ρ_{ab}, when scattering at impurities ($1/\tau_0$) and soft phonons (αT) dominate transport. The second term is due to intervalley scattering. Equation (6–7) contains four fitting parameters: $\tau_0, \alpha, \bar{\tau}$, and ω_0. The results of the fit are shown in the top panel of Fig. 6-4 are a red solid line. The fitting parameters are $\tau_0 = 6.29\times10^{-12}$ s, $\alpha = 0.09$, $\bar{\tau} = 1.4\times10^{-14}$ s, and $\omega_0 = 0.22$ eV. The values of τ_0 and α are in reasonable agreement with those found previously [73]. The frequency ω_0 is somewhat higher but still close to the frequency of the $E_{2\mathrm{g}}$ mode [83, 85]. A rather short nominal time $\bar{\tau}$ indicates strong coupling between electrons and optical phonons in graphite.

To summarize, we have studied, both experimentally and theoretically, the in-plane resistivity of HOPG. We found that its temperature dependence is determined by a competition between the number density and the scattering rate. At low temperatures, the scattering rate increases linearly with T, leading to a quasi-saturation of ρ_{ab} at $T \sim 300$ K. As the temperature increases, scattering off hard optical phonons becomes important, which leads to an exponential growth of the scattering rate with T. This results in a further increase of ρ_{ab} with T and in this temperature range bulk graphite can be imagined as bi-layer graphite (bi-layer graphene) since the higher order coupling terms are negligible.

6.3 Out of Plane Transport (ρ_c) Properties from 3K up to 1500K

So far in this chapter, we have discussed the in-plane transport properties of HOPG from 1.7 K up to 900 K and we have attributed the upturn in the resistivity at temperature above 300 K to scattering off hard phonons coming into the play and leading to an exponential increase in the scattering rate with temperature. Although the experimentally observed temperature dependence of the in-plane resistivity is rather unexpected and theoretically hard to explain, the temperature dependence of the in-plane resistivity from 1.7 K up to 300 K was quite expected and has already been explained by classical models [73]. However, the temperature dependence of the out-of-plane direction resistivity has always been puzzling in the literature and no concrete theory has been proposed and many models are still under debate.

The temperature dependence of the out-of-plane resistivity (ρ_c) in graphite is non-monotonic, meaning it is metallic like from 1.7 K up to T_{max} which is in the range 39 K -50 K. Above T_{max} the dependence is insulator like as displayed in Fig. 6-5. Surprisingly, similar temperature dependence in ρ_c has been experimentally observed on other layered materials with totally different Fermi energies and physical properties and electrical resistivity values such as layered perovskite Sr_2RuO^4 [63], high temperature superconductors [64], organic metals [64]. The fact that each of these materials possess different physical properties, but are still fortunate (or unfortunate) enough to share the same temperature dependence in the out-of-plane resistivity points out the only thing that those material have in common: weak coupling in between adjacent layers and high electrical anisotropy ($\rho_c/\rho_{ab} \approx 10^3 - 10^4$).

6.3.1 Breakdown in the Classical Model

Correlation in between the layered nature of these materials and the high electrical resistivity addressed in the literature and possible mechanisms can be listed but not limited to (1) stacking faults [86] (2) resistor network combination of tunneling across the planes and stacking faults [87] (3) coherent to incoherent cross-over (Anderson

localization) [88, 89]. The necessity of these non-trivial mechanisms might be questionable but all have been proposed in attempt to explain the non-monotonic behavior as well as large electrical anisotropy simultaneously which classical theory can not explain. Trivial application of the SWMc model to calculate the electrical anisotropy only predicts the out of plane resistivity values to be two orders of magnitude higher than the in-plane resistivity ($\rho_c \sim 10^2\ \rho_{ab}$). This difference is essentially comes from the different effective masses in the *c*-axis and *ab*-plane directions. On the other hand, experimentally the anisotropy reaches to $10^3 - 10^4$ and such large anisotropy can not be explained only by the differences in the effective masses. Lastly, even if the anisotropy is explained band theory does not handle the non-monotonic temperature dependence of the ρ_c well and lacks physical explanation.

6.3.2 Proposed Mechanisms and Discussion

After discussing the failure of the classical model to account for the large anisotropy and observed temperature dependence of the out-of-plane resistivity, we discuss the possibility of Anderson localization or coherent to incoherent crossover picture. Coherent to incoherent crossover occurs when the tunneling time between the layers becomes larger than the inelastic scattering time τ_{inelas}. When $\tau_{tun} < \tau_{inelas}$, electrons coherently tunnel through many layers before they experience collision. And accordingly; when $\tau_{tun} > \tau_{inelas}$, the electrons experience many collisions before they tunnel (incoherent). This model emphasizes on this transition occurs roughly around the resistivity peak temperature (T_{max}). However it has been experimentally shown that in the incoherent regime ($T > T_{max}$) there is no signature of non-metallic conductivity [88, 89] and the non-monotonic behavior this can not be explained.

Another proposed mechanism is based on the idea that electron waves are scattered from the stacking faults in the graphite [86]. As mentioned in Chapter 5, graphite consists of bernal stacked graphene layers (ABAB) while other minority phases such as rhombohedral phases (ABC stacking) and AAA stacking also exist. In this

model, naturally occurring stacking faults play an essential role in the out-of-plane transport direction. In this model, the variety of resistivity values measured on different HOPG sample has been successfully explained within the SWMc theory, however the temperature dependence of the ρ_c remained unexplained. Later on many other modifications to this model have followed [90] and decent fittings have been obtained best with unphysical relaxation times.

The final model in this chapter explaining the temperature dependence of c-axis resistivity is the resistor network model [87, 90]. In this model c-axis transport tunneling across the graphene sheets are in parallel combination with the spatially occurring metallic - like transport. In here, the parallel resistor model is an assumption and each process mentioned above serves as a conduction channel since the conductivities add to each other and the total conductivity reads,

$$\sigma_{total} = \sigma_T + \sigma_M, \tag{6–8}$$

where the σ_T and σ_M correspond to conductivity due to tunneling across the planes and metallic like transport. The σ_M is the phonon limited metallic like contribution and can is written as

$$\sigma_M = \frac{a}{b + T^2}, \tag{6–9}$$

and σ_T is the tunneling component fitted as

$$\sigma_T = cT^2 + \sigma(T = 0K), \tag{6–10}$$

Even though, parallel combination of these two transport mechanism gives fits the data, the extracted parameters don't give physical insight and this model also can't explain the high anisotropy measured in the samples [87, 90].

To understand the out-of-plane resistivity properties in graphite, we start expanding the temperature range where ρ_c is measured. Previously, ρ_c measured from 5K up to 300 K using physical property measurement system (PPMS) and the semiconducting like behavior observed in $T_{max} \leq$T$\leq$300 K range has been attributed to the tunneling processes in between graphene planes. However, these tunneling processes have different temperature dependence depending on the details of the tunneling mechanism, such as resonant tunneling assisted by one or two impurities [91], or direct tunneling [91, 92]. On the other hand, because of the limited temperature range, it is hard to conclude either one of these mechanisms proposed above.

We attempt to understand the transport mechanism that dominates at high temperatures (higher than T_{max}), by extending the resistivity measurements up to 1500 K as shown in Fig. 6-6. In Fig. 6-6 we note that at low temperature resistivity is not temperature in dependent and in fact becomes semiconducting like at temperatures below T_{min}. Moreover, the resistivity keeps decreasing as the temperature is increased without sign of saturation or resistivity upturn. Since the temperature range is extended from 250 K(from T_{max} to 300K) to $\sim$1500 K (from T_{max} to $\sim$1500K), one can clearly see if the resonant tunneling picture or other models can account for the observed temperature dependence in the electrical resistivity.

We first examine the possibility of resonant tunneling assisted by one or two impurities located in between two conducting plates that are separated by an insulator. The temperature dependence of the conductivity in this system has been studied experimentally and theoretically on metal/amorphous silicon/metal tunnel junctions [91] and the total tunneling conductivity is predicted to scale as

$$\sigma_T^1 \sim cT^2, \tag{6–11}$$

and

$$\sigma_T^2 \sim cT^{4/3}, \tag{6–12}$$

where σ_T^1 and σ_T^2 represent for tunneling conductivity across the tunneling junction via 1 or 2 localized impurities (resonant impurities) respectively. By using this system as a reference such that metal/ amorphous silicon / metal is replaced by graphene / gap / graphene, these two models might be applicable. However, the conductivity due to 2 or more localized impurities in the gap is not expected since the distance between adjacent graphene layers is $\sim$3.4$\AA$ and it is hard to physically incorporate 2 impurities in such a small gap. In this case, the conductivity is expected to scale as T^2. In Fig. 6-7, we have plotted the resistivity data in Fig. 6-6 as conductivity with respect to T^2. The data show striking linearity in the 300 K up to 1500 K range implying that the resonant tunneling assisted via one resonant impurity in between graphene planes. We note for the reader that previously such a linear fit was not possible due to the limited temperature range as shown in the inset of Fig. 6-7 and the deviation from the linearity below 300 K can be attributed to a transport mechanism of unknown origin becoming dominant at temperatures below T_{max}. Although the temperature dependence of the out-of-plane resistivity at high temperatures can be explained by the resonant tunneling picture (together with parallel conduction channel which is dominant a low temperatures), this model does not give any insight about the scattering times. Nevertheless, within this model, two independent transport mechanisms can be imagined as working parallel to each other in such a way that their conductivities (rather than their resistivities) are additive where the total conductivity is written as $\sigma_{tot} = \sigma_T + \sigma_M$ and the metallic part of the conductivity is attributed to the tilting (mosaic spread) and associated pick up from the in plane conductivity σ_{ab}.

A very traditional but often ignored model is the theory of band structure by Wallace [80]. Within this model, the conductivity in the c-axis direction can be calculated

by solving Boltzmann equation (Eq. 6–13) in the c-axis direction and using graphite's energy spectrum given by Eq. 6–14 (or Eq. 5–7),

$$\sigma_c(T) = 4e^2 \int d^3k \left(-\partial f_k^0/\partial \varepsilon_k\right) v_c^2 \tau(\varepsilon_k, T)/(2\pi)^3 \tag{6–13}$$

$$\epsilon = \pm\frac{1}{2}\Gamma \pm \left[\frac{\Gamma^2\gamma_1^2}{4} + \nu^2 k_\rho^2\right]^{1/2}, \tag{6–14}$$

and by taking the integral, the conductivity in the c-axis direction scales as [80],

$$\sigma_c \sim \alpha\tau T^2 \cdot ln\left(\frac{\gamma_1}{k_b T}\right), \tag{6–15}$$

Fitting predicted conductivity formula to the experimental results at high temperature are shown in Fig. 6-8 in the resistivity form. It can be seen from the figure that the conventional band structure picture by Wallace [80] can also explain the temperature dependence of ρ_c at high temperatures. However Wallace's model never received enough credit for explaining the c-axis transport properties simply because the high temperature resistivity properties were absent in the literature and the proper fitting has never been performed at temperatures above 400K. As a result of this lack of experimental data, most times Wallace's model has been overlooked and other exotic transport mechanisms have been exclusively considered in the literature. The fitting displayed in Fig. 6-8 essentially implies that the resonant tunneling model is not the unique model capable of explaining the data at those temperatures. The fitting to the Wallace's model (Eq. 6–15) starts to deviate around 400 K and possibly other transport mechanism starts to become apparent and eventually entirely dominate the transport below T_{max}. In the inset of Fig. 6–15 we show the fitted values of the τ given as a dashed line with the value of $2.8 \cdot 10^{-14}$ sec and is temperature independent since the fitting is done in the 400 K-1500 K range. To explain the temperature dependence of the out-of-plane resistivity, we revisit the Boltzmann equation given by Eq. 6–13.

In this equation, the integration *I*, $\int d^3k \left(-\partial f_k^0/\partial \varepsilon_k\right) v_c^2 \tau\left(\varepsilon_k, T\right)/(2\pi)^3$, can loosely be interpreted as the carrier density *n*. In this case, the conductivity scales as Drude formula, $\sigma_c \sim ne^2\tau/m^*$,meaning resistivity peak might be explained as a competition between carrier density *n* and the scattering time τ. The temperature dependence of number of carriers in HOPG graphite has been measured in the 5 K-300 K temperature range [73] and *n* increases with temperature. To account for the non-monotonic temperature dependence (Fig. 6-6), τ is expected to grow faster than *n* does.

A rough estimate of the scattering time, τ, can be extracted by dividing theoretically computed σ_c/τ (Eq. 6–13) by experimental σ_c^{exp}. The temperature dependence of the τ extracted out by this model is given by blue circles in Fig. 6-8 inset. First of all, the temperature dependence is rather minuscule and in agreement with the parameters extracted from the fitting values. Insensitivity of the scattering time τ essentially disregards the possibility of explaining the non-monotonic behavior by a competition in between *n* and τ. Nevertheless, the band theory [80] gives a good fit at high temperatures and the low temperature resistivity behavior can not be explained by this simple picture unless another transport mechanism is envoked.

In conclusion, in this section we have experimentally studied the transport properties of HOPG in the out-of-plane direction from 3K up to 1500 K experimentally. These results give a valuable insight into the possible mechanisms governing the transport at high temperatures. We have mainly considered the resonant tunneling mechanism where the impurity in between two graphene sheets acts as a resonant impurity and we have found that it gives good fit in the 300 K-1500 K rather, however it doesn't give any value on the scattering time τ as well as the low temperature (metallic like resistivity) has to be explained by another mechanism with parallel conduction channel. Similarly, Wallace's simple band structure theory also reproduces a good fit in the 400 K-1500 K range and is free of exotic transport mechanisms. It gives good fit with physical τ and γ_1 parameters. On the other hand, due to the temperature independent

scattering times (Fig. 6-8 inset blue circles), the low temperature resistivity can not be explained simply as a competition in between carrier density *n* and scattering time τ.

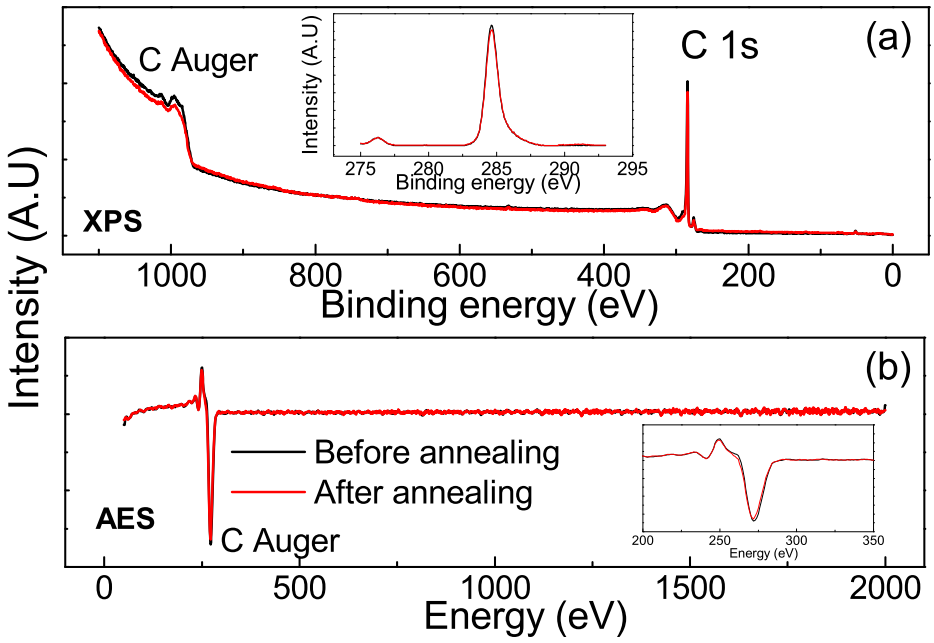

Figure 6-1. (a) XPS spectra before and after annealing. (b) AES spectra before and after annealing. Insets: magnified carbon peaks.

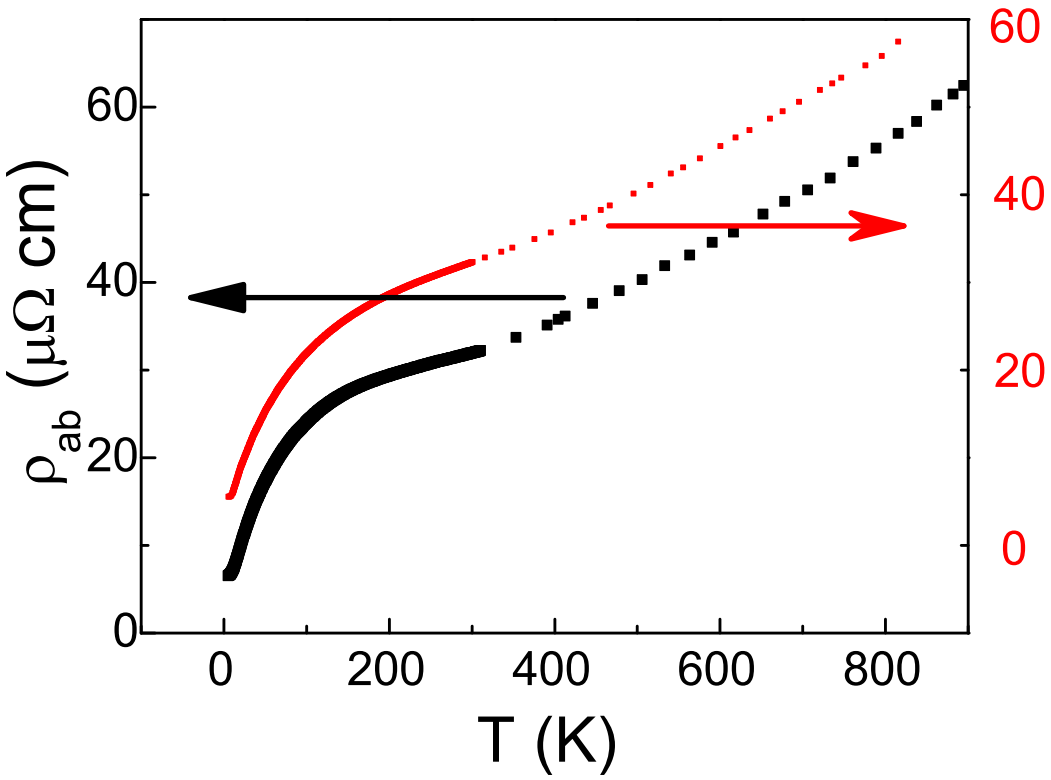

Figure 6-2. Temperature dependence of in-plane resistivity (ρ_{ab}) in HOPG from 1.7 K up to 900 K measured on two separate samples (black and the red curve).

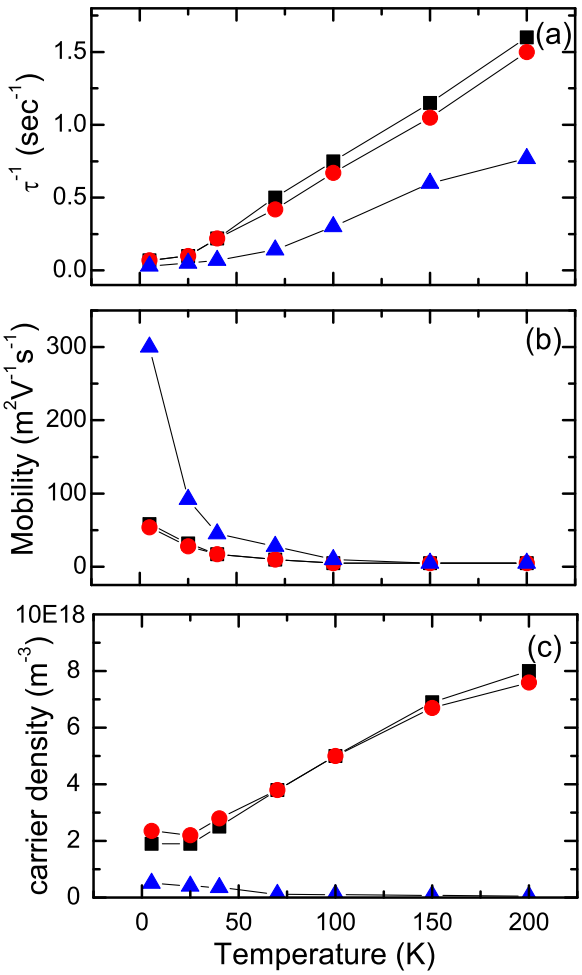

Figure 6-3. Temperature dependence of (a) τ^{-1} (b) mobility μ and (c) carrier density (*n*) from 300 K down to 5K.

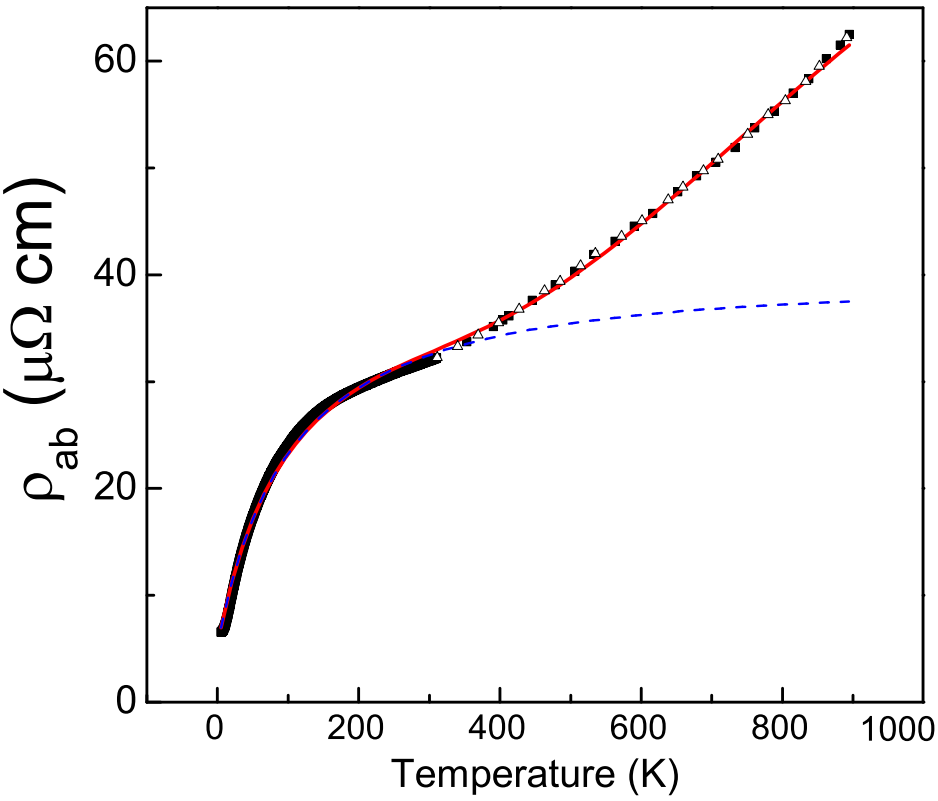

Figure 6-4. ρ_{ab} versus T in HOPG from 1.7 K up to 900 K for warming (black squares) and cooling (black hollow triangles). Blue dashed fit corresponds to the fitting from Wallace's model.

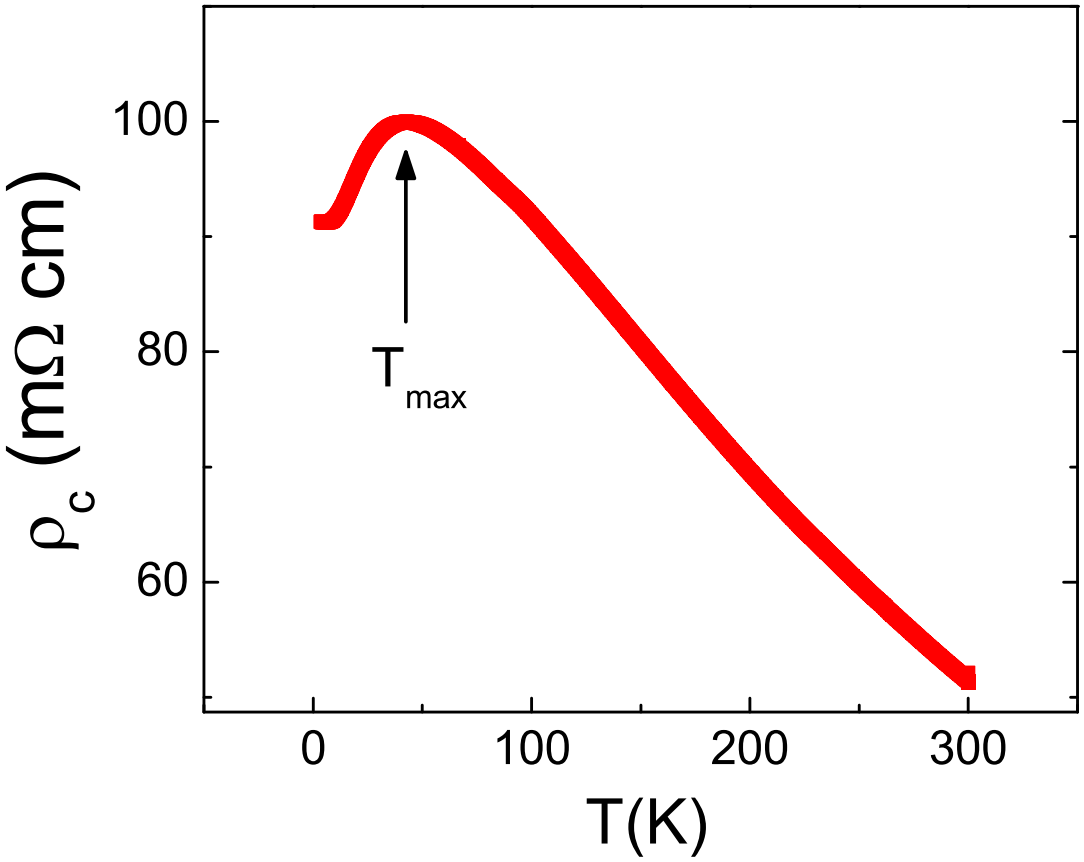

Figure 6-5. Temperature dependence of ρ_c in HOPG from 3K up to 300K. Resistivity gives a peak at temperature T_{max} as indicated in the figure

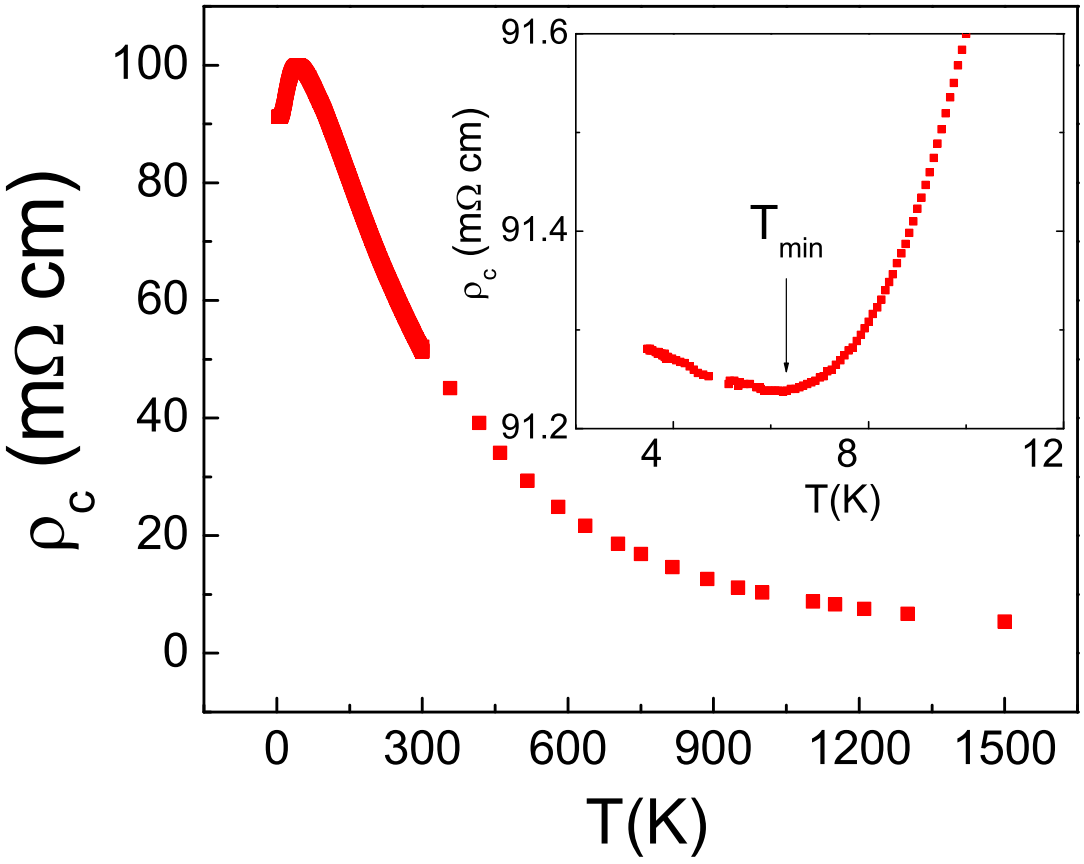

Figure 6-6. Temperature dependence of ρ_c in HOPG from 3K up to 1500K. Inset: Resistivity upturn observed below T_{max}

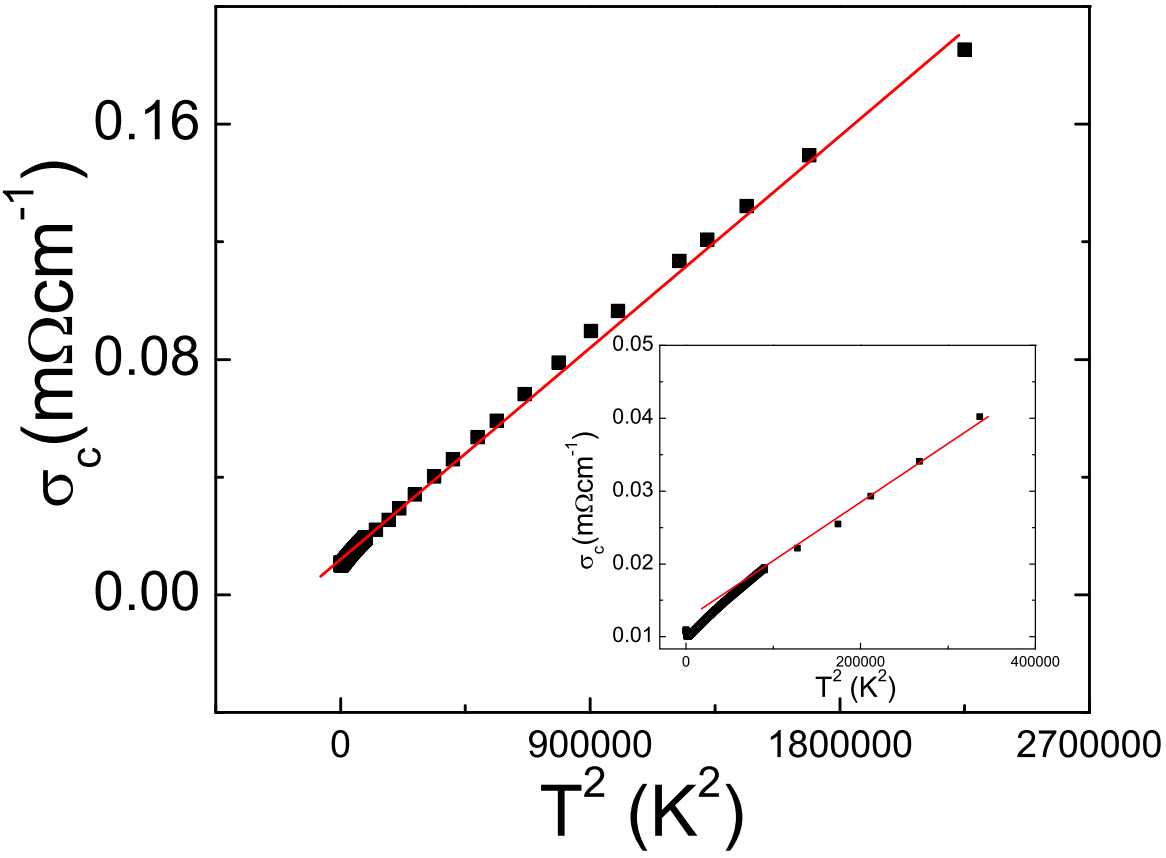

Figure 6-7. σ_c versus T^2 in the 300 K to 1500 K range with a linear fit (red line) Inset: Deviation from linearity below 300K due to unknown transport mechanisms.

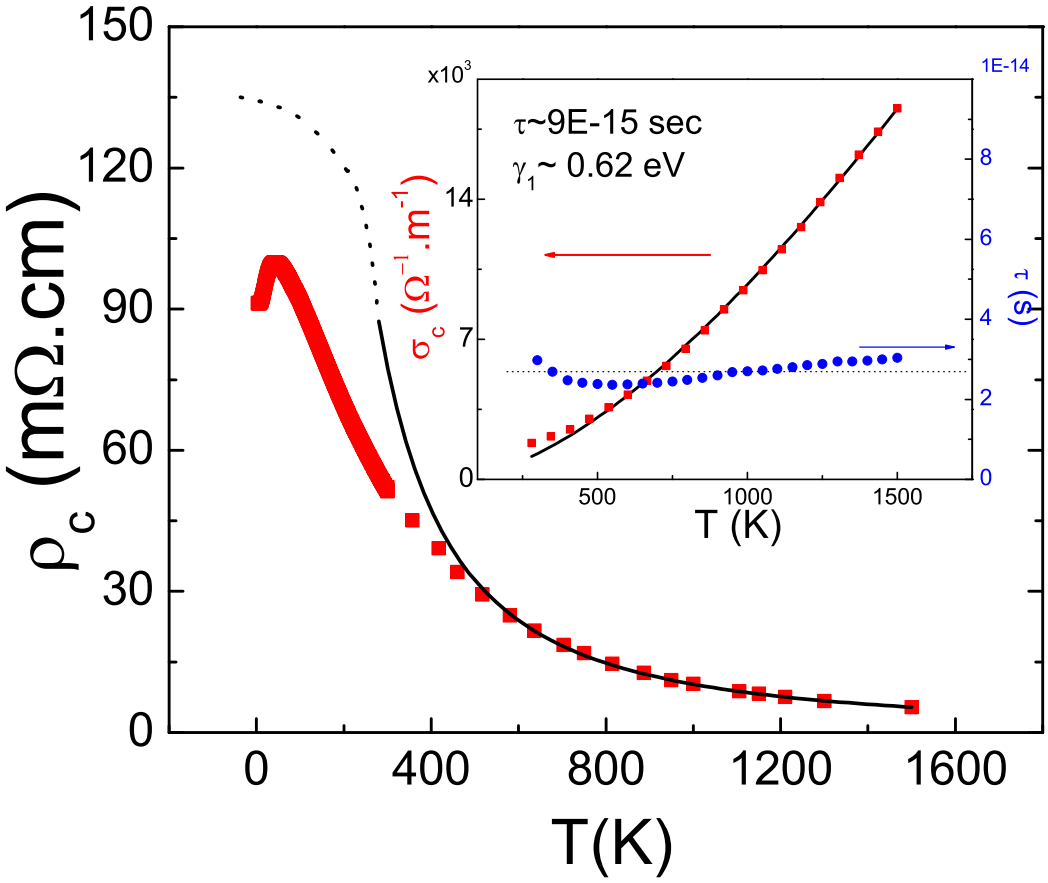

Figure 6-8. σ_c versus T^2 in the 300 K to 1500 K range with theoretical fitting (black line) Inset: τ extracted from experiment and theory (blue circles) and fitting to the experimentally measured resistivity (red circles in the inset) given by black straight line.

CHAPTER 7
SUPERMETALLIC CONDUCTIVITY IN BROMINE INTERCALATED GRAPHITE

7.1 Introduction

At the simplest level graphite can be thought of as an ordered Bernal stacking (refer to section 5.1.1) of weakly-coupled graphene sheets. Delamination or deconstruction of graphite into isolated graphene sheets for experimental characterization by mechanical means [42] has nucleated intense experimental and theoretical investigation into the electronic properties of this two-dimensional carbon allotrope. The presence of Dirac-like electronic excitations, an anomalous integer quantum Hall effect, and signature sensitivity to different types of disorder are but a few of the fascinating phenomena emerging from these studies. Bernal stacked graphite with an interplanar spacing $c = 3.4$ Å manifests properties that are precursors to the unusual behaviors associated with graphene and few-layer graphene. For example the presence of Dirac fermions near the H point in the Brillouin zone has been detected by angle-resolved photoemission spectroscopy [93].

Graphite intercalation compounds (GICs) have long been recognized as having unusual and sometimes surprising properties [54]. This chapter of the dissertation takes the approach of using bromine (Br) atom as an intercalant to simultaneously dope and separate the adjacent graphene planes in graphite and thereby begin an approach to the limit where the interplanar coupling is sufficiently weak to assure that the resulting in-plane conductivity can be considered as the parallel contribution of relatively independent doped graphene sheets. Since the band structure of graphite gives nearly equal numbers of electrons and holes (Chapter 5.1.2), with a density on the order of 10^{-4} carriers per carbon atom, [73] a small charge transfer between the intercalant and the adjacent carbon planes can result in a significant increase in free carriers per carbon. We find that random site interplanar doping with bromine to concentrations ($\leq$ 6 at%) gives rise to a pronounced decrease of the in-plane

resistivity ρ_{ab} to *supermetallic* values that are significantly lower than Cu over the temperature range 300 K$> T >$1.7 K. The remainder of this chapter is focused on displaying and discussing the observed changes in the electrical, structural, optical and the magnetization properties of HOPG upon bromine intercalation. Hall and X-ray photoelectron spectroscopy (XPS) measurements confirm that the Br dopant acts like an acceptor, thus hole doping the graphene planes. Optical reflectance measurements confirm the supermetallic in-plane conductivity and further reveal a doping-induced increase of mobility and carrier density. The diamagnetic susceptibility decreases toward zero as would be expected for isolated graphene sheets, [77] and there is no evidence of diamagnetic screening that might be associated with superconducting fluctuations. At $T = 5$ K the inferred sheet resistance per graphene plane of less than 1 Ω is significantly lower than reported for isolated graphene sheets either biased by an adjoining gate [42] or doped with impurity atoms. [94]

This chapter aims to report the experimental findings on Br intercalated graphite, understand and explain the physical processes/mechanisms associated with observation of supermetallicity. Section 7.2.1 gives the experimental details and material and characterization measurements such as X-ray diffraction (XRD), Auger electron spectrocopy (AES), X-ray photoelectron spectroscopy (XPS). In section 7.2.2, we show our main finding; ultraconductivity in Br intercalated graphite and we support these data with addition Hall effect data. To convince reader that the enhanced conductivity is real, we present optical data in section 7.2.3 and the magnetization properties in section 7.2.4 and discuss the results in section 7.2.5. In this chapter, the optical data presented in section 7.2.3 is taken in collaboration with Dr.J.Hwang and Dr. D. Tanner in Tanner's laboratory and all the theoretical considerations and interpretations are a result of collaboration with Dr. D. Maslov and his graduate student H. K. Pal.

7.2 Experimental

7.2.1 Sample Preparation and Characterization

The HOPG samples are cut from a single piece having 0.5° mosaic spread and typically have dimensions on the order of 1–5 mm. Prior to the transport measurements and bromine intercalation, samples are freshly cleaved. The samples are exposed to Br gas at room temperature in closed chamber at controlled rates for various intercalation times. After each exposure samples are removed from the chamber and measured in a four-contact arrangement using a LR700 17 Hz resistance bridge at temperatures and fields along the c-axis in the ranges 5 K $< T <$ 300 K and -7 T $< B <$ 7 T respectively using physical property measurement system (PPMS). Physical contacts to the samples are made by commercially available silver paints and homemade graphite paint. In highly anisotropic samples, precautions are needed to assure uniform current density between voltage leads [95]. We therefore used platelet (brick) shaped samples for the ρ_{ab} and ρ_c measurements while taking care to assure uniformly contacted current leads for each case. Results for the resistivity of a given sample are reproducible to 1% and for twelve different samples cut from the same piece reproducible to 3%. After each measurement, additional intercalations could be made on the same sample. Weight uptake and volume increase, measured to an accuracy of $\sim$ 3%, give a good measure of the correlation between Br concentration and doping time t_{Br}.

To characterize further the differences between pristine HOPG and the Br-doped samples, we also used X-ray diffraction (XRD), optical reflectance, Auger electron spectroscopy (AES), scanning electron microscopy (SEM) and x-ray photoelectron spectroscopy (XPS) (Chapter 4). SEM characterization did not detect any intercalation induced changes in surface morphology. The $\theta - 2\theta$ XRD scans revealed only (00l) reflections that were shifted to lower angle (increased lattice spacing) with increased intercalation time and hence the concentration of Br between the graphene layers. This expansion is in agreement with the observed swelling of the sample. There were

no additional reflections indicating staging [54] or, equivalently, ordering of the Br intercalants.

Optical reflectance measurements were made at 300 K using a Bruker 113v Fourier spectrometer over the range 40-5000 cm^{-1} (5-600 meV) and a Zeiss MPM 800 micro-spectrophotometer over 4000-40,000 cm^{-1} (0.5-5 eV). The low frequency limit is set by the signal-to-noise and diffraction limitations of our small samples. Br LMM Auger peaks are observed to be located at 1396 eV, 1442 eV and 1476 eV for Br exposure times $\geq$ 30 minutes. The samples were repeatedly cleaved and remeasured to probe the Br concentration at different depths of the sample; the peak heights for a given sample remained constant to within 5 %. The Br concentrations extracted from the Auger measurements agreed well with the weight-uptake/volume-expansion measurements.

XPS spectra of bromine doped HOPG samples were measured with a 99% monochromatized Mg X-ray source with energies up to 1100 eV. Sattelite peaks shifted by $\sim$ 10 eV were barely visible. Elemental percentage analyses were found to be consistent with AES and weight uptake measurements. The C 1s electron binding energy measured relative to the Fermi level is observed to be at 284.5 eV for pristine and at 284.0 eV for the t_{Br} =70 min sample. At first sight, the reduction in the C 1s binding energy by 0.5 eV contradicts the acceptor nature of Br, the more positively charged carbon should, for fixed E_F, have a higher binding energy. However, similar trends/findings in donor (acceptor) type intercalants and associated increase (decrease) in C 1s binding energy have been reported in the literature for different compounds [60, 96] and attributed to the change in E_F before and after intercalation. In brominated HOPG, E_F is negative and significantly larger in magnitude compared to pristine HOPG and the C 1s binding energy is thus measured with respect to the lower E_F of the hole-doped system. Accordingly, the increase in the C 1s binding energy is more than compensated for by the decrease in E_F, giving an overall decrease in the C 1s peak position as observed. The XPS method thus gives another way of estimating the

change in Fermi level and implies a ~ -0.5 eV change in E_F after hole doping to 6 at% Br. (refer to section 4.3.3).

7.2.2 Electrical Measurements

Fig. 7-1a shows the dependence of ρ_{ab} on Br intercalation time at $T = 300$ K. Although the initial linear dependence is not understood, we note that after 70 minutes, ρ_{ab} appears to saturate at a value which is approximately a factor of five lower than the room temperature value ($1.7\ \mu\Omega$cm) of copper indicated by the horizontal dashed line. Our interpretation of how the carrier density N, the scattering time τ and the effective mass $m^\star$ are affected by Br intercalation is based on using the Drude model in which the conductivity σ of each contributing band is $\sigma = Ne^2\tau/m^\star = Ne\mu$, where the mobility $\mu = e\tau/m^\star$.

In Fig. 7-2 we show the evolution of the field (B) dependent transverse resistance ρ_{xy} for various intercalation times t_{Br} ranging from $t_{Br} = 0$ (pristine HOPG) to $t_{Br} = 70$ min. The data for pristine HOPG are well fit by the expression for the two-band model, [73]

$$\frac{\rho_{xy}(B)}{e\rho_{xx}(0)^2} = \frac{\left(-n_e\mu_e^2 + n_h\mu_h^2\right) B + \mu_e^2\mu_h^2\left(n_h - n_e\right) B^3}{1 + e^2\rho_{xx}(0)^2\mu_e^2\mu_h^2\left(n_h - n_e\right)^2 B^2} \tag{7–1}$$

where $\rho_{xx}(0)$ is the $B = 0$ in-plane resistivity and the subscripts e and h refer respectively to the electron and hole bands. The parameters n_h, n_e, μ_h and μ_e are obtained by the following procedure;

within two band model the transverse resistivity can be written as,

$$\rho_{xy} = \frac{\left(\rho_h^2 R_e + \rho_e^2 R_h\right) B + R_h R_e\left(R_h + R_e\right) B^3}{\left(\rho_h + \rho_e\right)^2 + \left(R_h + R_e\right)^2 B^2}, \tag{7–2}$$

where $R_h = 1/n_h e$, $R_e = 1/n_e e$, $\rho_h = 1/n_h e\mu_h$ and $\rho_e = 1/n_e e\mu_e$. By using these expressions in Eq. 7–2 reduces to,

$$e\rho_{xy} = \frac{\left(-n_e\mu_e^2 + n_h\mu_h^2\right) B + \mu_e^2\mu_h^2 \left(n_h - n_e\right) B^3}{\left(n_e\mu_e + n_h\mu_h\right)^2 + \mu_e^2\mu_h^2 \left(n_h - n_e\right)^2 B^2} \tag{7–3}$$

In graphite, majority electron and holes contribute to the conductivity and the total resistance ρ_{xx} reads,

$$\rho_{xx}^{-1} = \rho_e^{-1} + \rho_h^{-1} = e\left(n_e\mu_e + n_h\mu_h\right), \tag{7–4}$$

substituting Eq. 7–4 into Eq. 7–2 yields,

$$\frac{\rho_{xy}(B)}{e\rho_{xx}(0)^2} = \frac{\left(-n_e\mu_e^2 + n_h\mu_h^2\right) B + \mu_e^2\mu_h^2 \left(n_h - n_e\right) B^3}{1 + e^2\rho_{xx}(0)^2\mu_e^2\mu_h^2 \left(n_h - n_e\right)^2 B^2} = \frac{\alpha B + \beta B^3}{1 + \gamma B^2} \tag{7–5}$$

where α, β and γ are given by

$$\alpha = -n_e\mu_e^2 + n_h\mu_h^2 \tag{7–6}$$

$$\beta = \mu_e^2\mu_h^2 \left(n_h - n_e\right) \tag{7–7}$$

$$\gamma = e^2\rho_{xx}(0)^2\mu_e^2\mu_h^2 \left(n_h - n_e\right)^2 \tag{7–8}$$

$$\frac{\gamma}{\beta} = e^2\rho_{xx}^2 \left(n_h - n_e\right) \tag{7–9}$$

Fitting the transverse resistivity in the form given in Eq. 7–5 to the hall magnetoresistivity displayed in Fig. 7-2 results in set of fitting parameters, α, β and γ. After determination of all the parameters, one determines the deviation from compensation from Eq. 7–9, which is expressed as $n_h - n_e$. Similarly, rearranging Eq. 7–7 gives another important relation regarding to $\mu_e\mu_h$ given as,

$$\mu_e\mu_h = \sqrt{\frac{\beta}{n_h - n_e}} = \sqrt{\frac{\beta}{\frac{\gamma}{e^2\rho_{xx}^2\beta}}} = \frac{e\rho_{xx}\beta}{\gamma^{1/2}} \tag{7–10}$$

Another equation that is used in determining number density and mobility of each channel is can be derived from the fitting parameter α as follows,

$$\alpha = -n_e\mu_e^2 + n_h\mu_h^2 = \mu_e^2\mu_h^2\left(\frac{n_h}{\mu_e^2} - \frac{n_e}{\mu_h^2}\right) = \frac{\beta}{(n_h - n_e)}\left(\frac{n_h}{\mu_e^2} - \frac{n_e}{\mu_h^2}\right) \tag{7–11}$$

using $n_h - n_e$ in Eq. 7–11 gives,

$$\alpha = \frac{\beta}{\frac{\gamma}{\beta e^2\rho_{xx}^2}}\left(\frac{n_h}{\mu_e^2} - \frac{n_e}{\mu_h^2}\right) \tag{7–12}$$

by arranging the last equation we get,

$$\left(\frac{n_h}{\mu_e^2} - \frac{n_e}{\mu_h^2}\right) = \frac{\alpha\gamma}{e^2\rho_{xx}^2\beta^2} \tag{7–13}$$

To summarize all the equations used to analyze the Hall data,

$$n_e + \mu_e + n_h\mu_h = \frac{1}{e\rho_{xx}}, \tag{7–14}$$

$$n_h - n_e = \frac{\gamma}{e^2\rho_{xx}^2\beta}, \tag{7–15}$$

$$\mu_e\mu_h = \frac{e\rho_{xx}\beta}{\gamma^{1/2}}, \tag{7–16}$$

$$\left(\frac{n_h}{\mu_e^2} - \frac{n_e}{\mu_h^2}\right) = \frac{\alpha\gamma}{e^2\rho_{xx}^2\beta^2}, \tag{7–17}$$

These four equation involve four unknowns (μ_e, μ_h, n_e and n_h), and can be solved exactly. The obtained fitting parameters are $n_h = 2.0(1) \times 10^{19}$ cm^{-3}, $n_e = 1.6(1) \times 10^{19}$ cm^{-3}, μ_h = 4700(100) cm^2/V·s and μ_e = 6800(100) cm^2/V·s showing that our pristine HOPG is slightly hole doped with similar mobilities in each band.

In graphite, Eq. (7–1) is applicable for $\mu B \gtrsim 1$, when $\rho_{xx}(B)$ is quadratic in B. [97] At $T = 300$ K, $\mu B = 1$ corresponds to $B = 0.3$ T in pristine graphite, so

Eq. (7–1) describes most of the field range presented in Fig. 7-2. With increasing t_{Br}, the quadratic dependence of $\rho_{xx}(B)$ occurs over a decreasing field range, thus restricting the range of validity of Eq. (7–1). Constrained by this requirement, we extract a square-root dependence of N on t_{Br} shown in Fig. 7-1b. As seen in Fig. 7-2, the low-field slope, which is positive for $t_{Br} \geq$20 min. decreases with increasing Br concentration and becomes linear for the highest t_{Br}, thus indicating that Br is hole doping the graphene sheets with a carrier density $N = n_h$ dominated by holes.

The temperature-dependent resistivity data of panels (a) and (b) of Fig. 7-3 show that the resistivity scales for ρ_{ab} (ρ_c) decrease (increase) as T is reduced from 300 K to 5 K. The positive curvature for samples with $t_{Br} \geq 70$ min. is consistent with the notion that the doping is sufficient to guarantee $E_F \gg k_B T$ in contrast to pristine HOPG and the lightly doped samples where $E_F \sim$300 K and significant variation of N with T leads to a negative curvature of $\rho_{ab}(T)$. In principle, the negative curvature in the temperature dependence of ρ_{ab} observed in pristine HOPG samples is a result of competition in between the temperature dependence of scattering time τ and number of carriers N. Upon cooling from room temperature down to lower temperatures, because of the small magnitude of the Fermi energy in HOPG, the number of carriers increases by a factor of 4-6 times especially in the 300 K-70 K range and is almost constant below that temperature [73]. On the other hand, the scattering time τ, decreases drastically at low temperatures (1.7 K-60 K) since the phonon scattering is greatly reduced at these temperatures. Using Drude formula, the temperature dependence in these two parameters result in rather slow decrease in resistivity as temperature is lowered from 300 K down to 70 K associated with compensation of increase in τ with decrease in N. However, at lower temperatures number of carriers stays temperature independent as τ starts to increase faster as temperature is lowered from 70 K to 1.7 K and this gives the unique negative curvature in the ρ_{ab} in HOPG. As the HOPG is intercalated as determined from XPS (section 4.3.3) and Hall measurements (Fig. 7-1 and Fig. 7-2),

the Fermi level of the system increases order by 0.5 eV and becomes much higher than the Fermi energy of pristine graphite which is ∼25 meV. In this case, the number density N becomes temperature independent, while the electrical transport is still phonon dominant and when N is completely temperature independent, ρ_{ab} is expected to have a positive curvature. In Fig.7-3, as the HOPG is intercalated the curvature of the temperature dependence of the in-plane resistivity changes slowly from negative to positive. This picture also gives an indirect measure of Fermi energy of graphite after the intercalation takes place. The ratio ρ_{ab}(300 K)/ρ_{ab}(5K) = 47 for the sample with t_{Br}=70 min. is higher by more than a factor of 10 than the same ratio (4.0) for pristine HOPG can also be attributed to the temperature independent N.

In contrast to ρ_{ab}, ρ_c increases with increasing t_{Br} due to the presence of Br intercalants acting like a negative pressure pushing the planes apart (schematic inset of Fig. 7-1a), thereby resulting in decreased interplanar tunneling. With the application of positive pressure the interplanar spacing decreases and there is a corresponding decrease in ρ_c. [87] The hole doping of the planes (decreasing ρ_{ab}) concomitant with an increasing interplanar spacing (increasing ρ_c) leads to an anisotropy ratio ρ_c/ρ_{ab} at 5 K approaching 10^7, a factor of 1000 greater than measured for pristine HOPG at the same temperature.

7.2.3 Optical Measurements

With increasing t_{Br} the far-infrared and midinfrared reflectance increase dramatically as shown in Fig. 7-4a. This increase in reflectance implies an associated increase in optical conductivity which is borne out by a Kramers-Kronig analysis [98]. We used a Drude extrapolation at low frequencies and a power-law behavior at high frequencies, with the results shown in Fig. 7-4b. Note that the optical conductivity curves include frequencies (dashed lines) where we used the extrapolation; the good agreement with the dc conductivity in Fig. 7-1a and the good fits to the reflectance provide confidence that the behavior is as shown. As the doping proceeds, the low-frequency conductivity

increases and the spectral weight (the area under the curve) increases significantly (Fig. 7-4b). The full width of this Drude-like peak represents the carrier scattering rate τ^{-1}which at the highest doping is decreased by a factor of five relative to the pristine sample.

We also note in the raw reflectance data of Fig. 7-4a the appearance of a phonon mode around 1580 cm^{-1}. This mode, which appears to strengthen and develop a Fano lineshape with Br intercalation, can barely be seen as a small feature above the line in the conductivity spectra of Fig. 7-4b. To show this feature in more detail, we have magnified the appropriate region by a factor of 1000 as shown in Fig. 7-5. The weak optical phonon near 1588 cm^{-1} increases in strength by nearly a factor of four and red shifts by 3 cm^{-1}. These trends are consistent with prior results [54, 99] which show that intercalation changes the lineshape, lowers the frequency, and also leads to higher oscillator strength of this mode. Metallic behavior thus persists out to these energies in the strongly intercalated samples.

From the sum rule on the optical conductivity, we can relate the low-energy spectral weight to the carrier density. The spectral weight also affects the real part of the dielectric function, $\epsilon_1(\omega)$, which for free carriers follows $\epsilon_1(\omega) = 1 - \omega_p^2/\omega^2$, where $\omega_p^2 = 4\pi Ne^2/m^\star$ is the plasma frequency. The inset of Fig. 7-4b shows $\epsilon_1(\omega)$ plotted vs $1/\omega^2$; the slopes of these plots give the carrier density, which is seen to increase by more than a factor of eight with increasing t_{Br}. That the curves are straight lines implies strongly that a free-carrier (metallic) picture of the low-energy electrodynamics is an accurate view of the intercalated graphite. The dc resistivities inferred from the Drude fit to the infrared reflectance measurements are shown as blue triangles in Fig. 7-1a. Because the reflectance measurements are made without placing electrical contacts on the sample, the inferred dc conductivities of Fig. 7-4b give independent confirmation of the supermetallic conductivity inferred from transport measurements.

7.2.4 Magnetization Measurements

Fig. 7-6 shows that the temperature dependent dc diamagnetic susceptibility χ (field parallel to *c*-axis) decreases with increasing t_{Br}. Our room temperature value for pristine graphite, $\chi = -21.3 \times 10^{-6}$ emu/g, is in good agreement with previous experiments; [77] the susceptibility decreases by a factor of three for t_{Br}=90 min. This decrease in χ with increased hole doping of the graphene planes is qualitatively understood by realizing that as the Fermi energy moves away from the neutrality point ($n_h = n_e$) of pristine graphite, the cyclotron mass $m_c^\star$ increases and $\chi \propto 1/m_c^\star$ decreases, approaching the limit of exponentially weak diamagnetism for single-plane Dirac fermions. Importantly, there is no signature of superconductivity, which, if associated with the giant conductivity, would become manifest as an *increase* in diamagnetism at some characteristic temperature.

7.2.5 Discussion

Graphite intercalation compounds in the dilute limit are well known to exhibit enhancements of room-temperature conductivity which, with increasing intercalant concentration, saturate to modest values $\sim$10 times the pristine value. [100] The surprising and unexpected result presented here is that for uniformly dispersed non-staged Br dopants at relatively low concentrations near 5-6 at%, the conductivity can justifiably be referred to as “supermetallic”. To make comparisons to single-layer graphene, we convert our ρ_{ab} measurements to resistance per square R_g of each carbon plane and see that R_g near 1000 Ω for HOPG at 300 K decreases to less than 0.5 Ω at 5 K for intercalated samples with t_{Br}=70 min. To our knowledge there are no reports of such a low R_g for graphene.

The experimental results raise many questions, since doping introduces disorder, why does the conductivity increase? At high doping level, most of the carriers (holes) come from negatively charged acceptors, so we have a system in which the number of carriers is approximately equal to the number of scattering centers. On the other

hand, since the Fermi energy shifts downward and increases with doping, the scattering cross-section decreases, so we have two competing effects. Assuming for a moment that the scattering cross-section is of the 2D classical Rutherford form $A_R \sim e^2/E_F$, that E_F obeys the 2D scaling $E_F \propto n_a$, where $n_a = n_h c$ is the number density of acceptors per layer, and estimating the mean free path as $\ell = 1/n_a A_R$, we arrive at a simple result for the parameter $k_F\ell$, which characterizes purity of a material: $k_F\ell \sim 1/r_s$, where r_s is the average inter-carrier distance measured in Bohr radii. Already in pristine graphite, $r_s \sim 1$ (Ref. [101]) and it decreases further with doping, so this simple model predicts that the material becomes "cleaner" with doping, concomitant with an increase in the 2D conductivity, which is proportional to $k_F\ell$.

In reality, this simple picture is modified significantly due to effects of screening. To see this in more detail, we consider the screening mechanism in doped graphite. In pristine graphite, the Fermi energy $E_F \approx 22.5$ meV is on the order of the hopping energy between the next-to-nearest graphene layers, γ_2. Upon doping the Fermi energy increases. We consider two limiting cases: i) $\gamma_2 \ll E_F \ll \gamma_1$ and ii) $\gamma_1 \ll E_F \ll \gamma_0$, where $\gamma_1 \approx 0.3$ eV is the nearest-layer hopping and $\gamma_0 \approx 3.2$ eV is the nearest-neighbor hopping in the graphene plane. In the first case, graphite is the "bi-layer regime": [101]the energy spectrum of holes is approximately $\varepsilon_k = -\hbar^2 k_{||}^2/2m_{||}(k_z)$, where $m_{||}(k_z) = \bar{m}_{||}\cos(k_z c/2)$ is the k_z dependent in-plane mass with $\bar{m}_{||} \equiv \gamma_1/v_0^2$, $v_0 \approx 10^8$ cm/s is the Dirac velocity, and $c \approx 6.8$ Å is the c axis lattice constant. The density of states (per spin and per K point of the graphite Brillouin zone) in this regime $\nu = \gamma_1/\hbar^2\pi^2 v_0^2 c$ does not depend on the electron energy. In the second case, graphite is in the graphene regime: the spectrum is Dirac-like $\varepsilon_k = -\hbar v_0 k_{||}$ and the density of states $\nu = \varepsilon/2\pi^2\hbar^2 v_0^2 c$ increases linearly with energy ε. In the Thomas-Fermi model, the square of the screening wave vector is $\kappa^2 = 16\pi e^2\nu$. Although κ increases with E_F, it still remains much smaller than the reciprocal lattice constant for not too high dopings. Indeed, it is easy to see that $\kappa^2 c^2 \sim (c/a_B)(E_F/\gamma_1)$ in the graphene regime, where

$a_B = \epsilon_0 \hbar^2 / e^2 \bar{m}_{||} \approx 50$Å for the background dielectric constant $\epsilon_0 = 5$. [102] Therefore, $\kappa^2 c^2 \lesssim 1$ for $E_F \lesssim 10\gamma_1 \approx \gamma_0$. Accordingly, in both the bilayer and graphene regimes screening is not sensitive to details of the spectrum, all of which are incorporated into the density of states. In the continuum limit, with the screening radius large compared to the lattice constant, the screened potential is isotropic.

The above arguments allow us to model the potential of a single charged acceptor by a simple Thomas-Fermi form

$$V(q) = -\frac{4\pi e^2}{q_{||}^2 + q_z^2 + \kappa^2}, \tag{7–18}$$

where $\hbar q_{||}$ and $\hbar q_z$ are the in-plane and c-axis momentum transfers of charge carriers. The scattering time can be then obtained from the Fermi Golden Rule

$$\frac{1}{\tau} = \frac{2\pi}{\hbar} n_a \int \frac{d^2 q_{||}}{(2\pi)^2} \int \frac{dq_z}{2\pi} V^2(q)\, \delta\left(\varepsilon_{\mathbf{k}_{||}+\mathbf{q}_{||}, k_z+q_z} - \varepsilon_{\mathbf{k}_{||}, k_z}\right). \tag{7–19}$$

Another simplification comes from the fact that $q_{||}$ is bounded by twice the in-plane radius of the Fermi surface $k_{F||} \sim \sqrt{n_h c}$, which is smaller than κ for not too high dopings. This implies that one can neglect $q_{||}$ in Eq. (7–18). On the other hand, as typical $q_z \sim \kappa \ll 1/c$, one can neglect q_z in the energies entering the δ function in Eq. (7–19). The integral over q_z can be then performed independently of that over $\mathbf{q}_{||}$ and yields an effective coupling constant for in-plane scattering $\bar{V} = \int dq_z V^2(q)/2\pi = 4\pi^2 e^4/\kappa^3$. In terms of $\bar{V}$, the scattering rate can be written as

$$\frac{1}{\tau} = \frac{2\pi}{\hbar} n_a \bar{V} \nu_{2D}, \tag{7–20}$$

where

$$\nu_{2D} = \int \frac{d^2 q_{||}}{(2\pi)^2} \delta\left(\varepsilon_{\mathbf{k}_{||}+\mathbf{q}_{||}, k_z} - \varepsilon_{\mathbf{k}_{||}, k_z}\right) \tag{7–21}$$

is the effective density of states per graphene layer. Accordingly, charged acceptors act effectively as short-range scatterers which affect only the in-plane motion of electrons.

A posteriori, this explains why we ignored the difference between the total and transport scattering times. In the bi-layer regime, $\nu_{2D} = m_{||}(k_z)/2\pi\hbar^2$, while in the graphene regime $\nu_{2D} = \varepsilon/\hbar^2 v_0^2$. In both cases, $\nu_{2D} \sim \nu c$. Therefore, one can write down the following estimate for $1/\tau$:

$$\frac{1}{\tau} \sim \frac{e^2}{\hbar}\frac{n_a c}{\kappa}.$$

In the bi-layer regime, κ does not depend on n_a and, therefore, $1/\tau$ increases linearly with doping. In the graphene regime, κ does increase with doping (so that the effective scattering cross-section decreases) but only weakly–as $\nu^{1/2} \propto E_F^{1/2} \propto n_a^{1/4}$–and $1/\tau$ still increases with n_a (as $n_a^{3/4}$). We see, therefore, that the observed non-monotonic dependence of $1/\tau$ on doping shown in Fig. 7-7 cannot be explained within a model of scattering from randomly placed charged acceptors that are screened by mobile carriers.

A decrease of $1/\tau$ with doping may be attributed to partial ordering of Br ions: the absence of three-dimensional order (staging) does not preclude formation of a laminar structure, in which there is no correlation between ordered layers of the intercalant. [103] Scattering of charge carriers by such layers will be suppressed due to miniband formation (if the Fermi energy lies outside the forbidden gaps) in exactly the same way (partial) ordering of donors in modulation-doped semiconductor heterostructures is believed to be responsible for extremely high carrier mobilities in such structures. At the highest doping level achieved in this study (bulk number density $n = 10^{20}$ cm^{-3} or sheet density per graphene layer $nc/2 = 3.4 \times 10^{12}$ cm^{-2}), the average distance between Br intercalants is 30 Å. For $\epsilon_0 = 5$, the Coulomb energy at this distance is about 0.1 eV, which is about 4 times larger than the thermal energy at room temperature. Theoretical and experimental studies of 2D classical Wigner crystals on structureless (liquid) substrates show that the Coulomb energy exceeds the thermal energy at the melting temperature by a factor of 127. [104] According to this criterion, a Wigner crystal is not expected to be stable above 10 K in our case. Screening by mobile carriers

should lead to a further reduction of the melting temperature. Nevertheless, the 2D order can be stabilized due to the presence of crystalline substrate (graphene sheets). Also, a fully developed 2D order may not be needed–long-range correlations in the positions of Br ions may be enough to reduce their effect on the mobility of free carriers. A detailed analysis of this question requires separate experimental and theoretical studies which are outside the scope of this chapter.

The mobility of Br-intercalated HOPG at room temperature, confirmed by optical measurements, is 50,000 $cm^2/V{\cdot}sec$, a factor of 5 higher than pristine HOPG. From transport data at 5 K we find $\mu_h \sim 10^6$ $cm^2/V{\cdot}$ s but consider this with some reservations in the absence of confirming optical data. Although we have not reached the limit where the interplanar coupling is sufficiently low to consider our intercalated graphite as an ordered stack of isolated graphene sheets each of which is dominated by Dirac fermions, we believe our results illustrate the emergence of intriguing phenomenology at the graphite/graphene boundary accessed by intercalation.

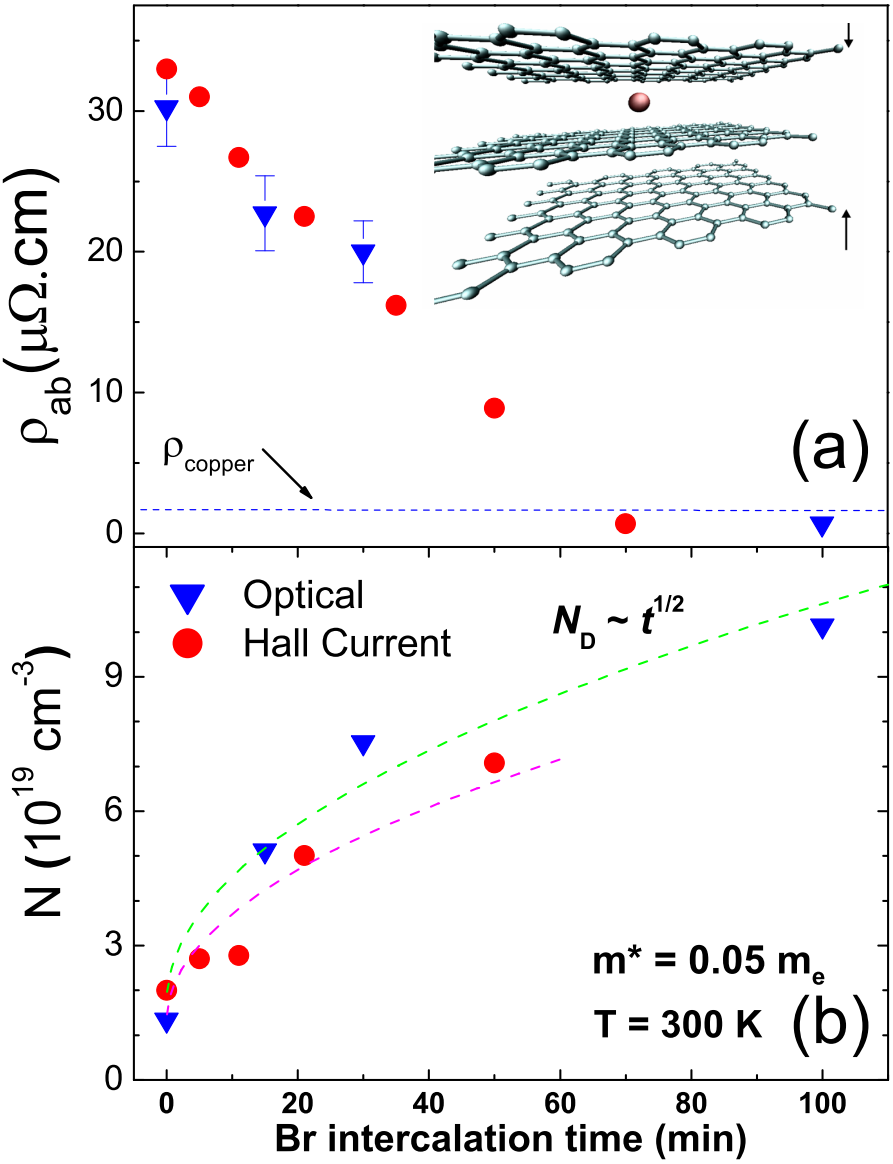

Figure 7-1. Plots of the room temperature in-plane resistivity ρ_{ab} (a) and carrier density N (b) as a function of Br intercalation time. The solid red circles (blue triangles) in both panels are inferred from transport/Hall (optical reflectance) measurements. After 100 minutes ρ_{ab} is reduced by a factor of 100 below its starting value to a resistivity that is a factor of five below that of copper (horizontal dashed line).

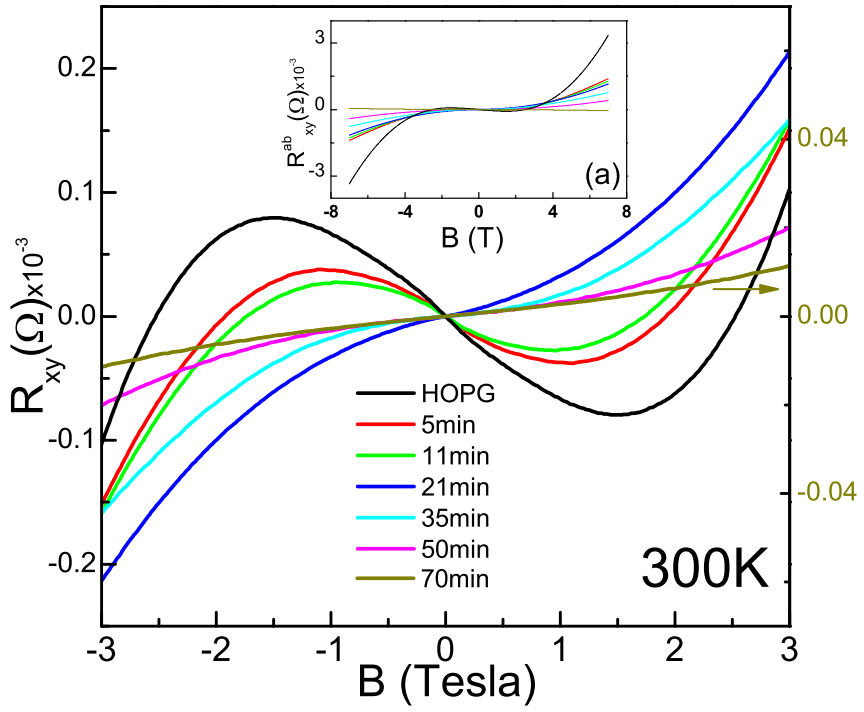

Figure 7-2. Transverse resistance ρ_{xy} as a function of perpendicular magnetic field B for the indicated intercalation times. The inset shows the same data over a larger field range.

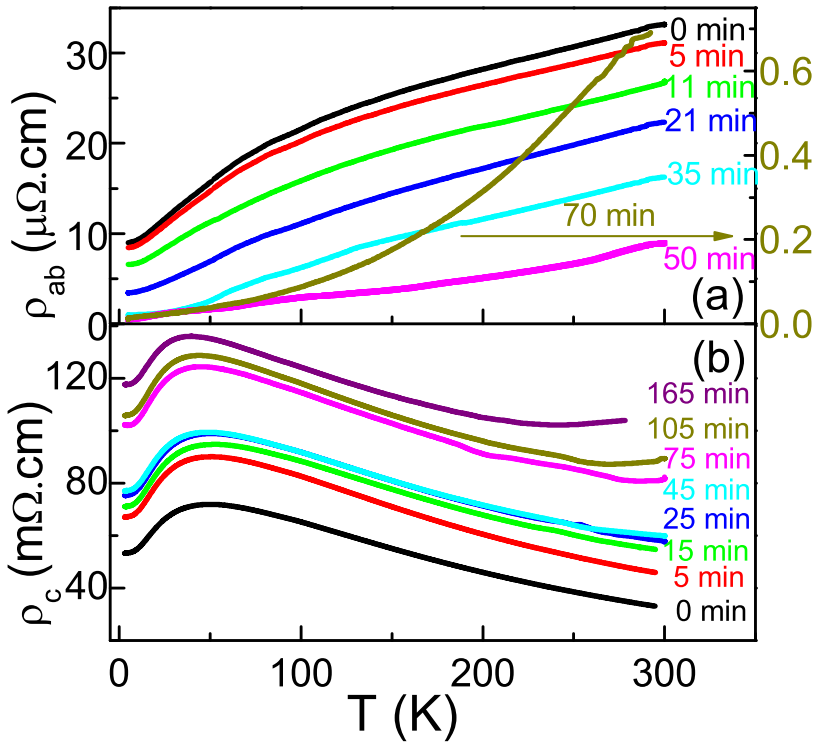

Figure 7-3. Temperature dependence of (a) ρ_{ab} and (b) ρ_c at the indicated intercalation times. The right hand axis of panel (a) is an expanded scale for the t_{Br}=70 min. curve

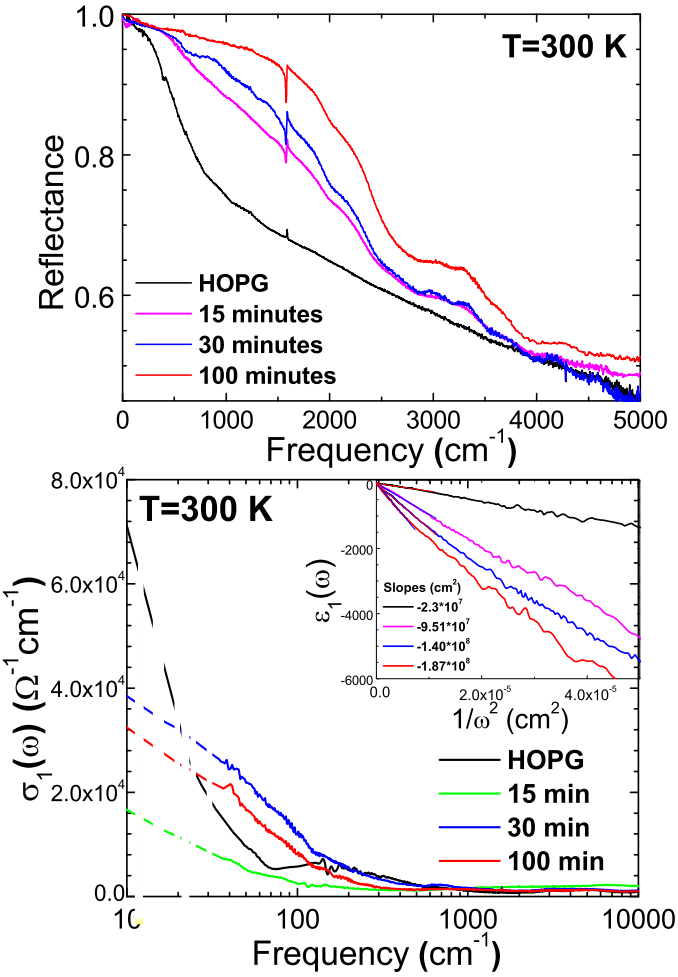

Figure 7-4. Infrared reflectance (a) and optical conductivity, $\sigma_1(\omega)$, (b) at indicated intercalation times t_{Br}. Data below 35 cm^{-1} in panel (b) are from the Drude-Lorentz fit to the reflectance. Inset: Real part of the dielectric function versus $1/\omega^2$. The slope, proportional to the plasma frequency squared, is a measure of the total carrier density.

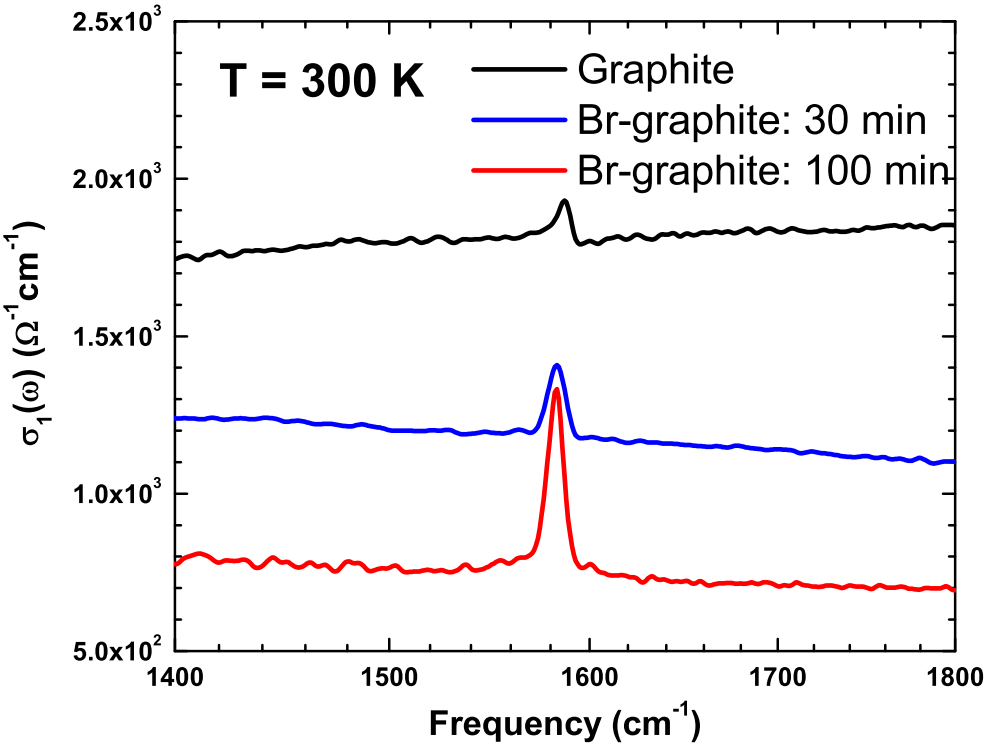

Figure 7-5. Optical conductivity of graphite and Br-doped graphite in the region of the 1588 cm^{-1} phonon corresponding to the intercalation times t_{Br} (top to bottom) indicated in the legend.

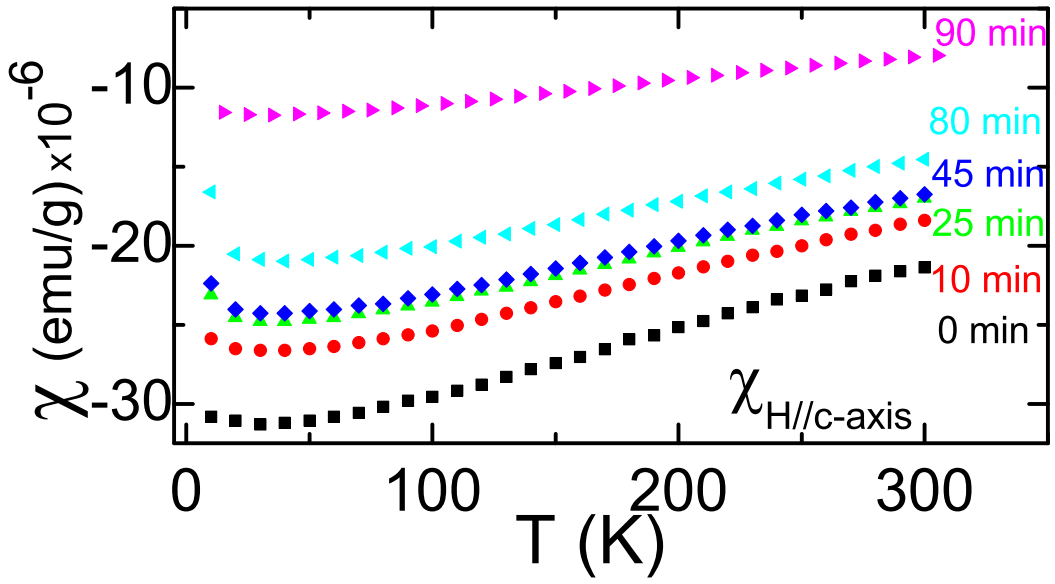

Figure 7-6. Temperature dependence of magnetic susceptibility χ_c at the indicated intercalation times.

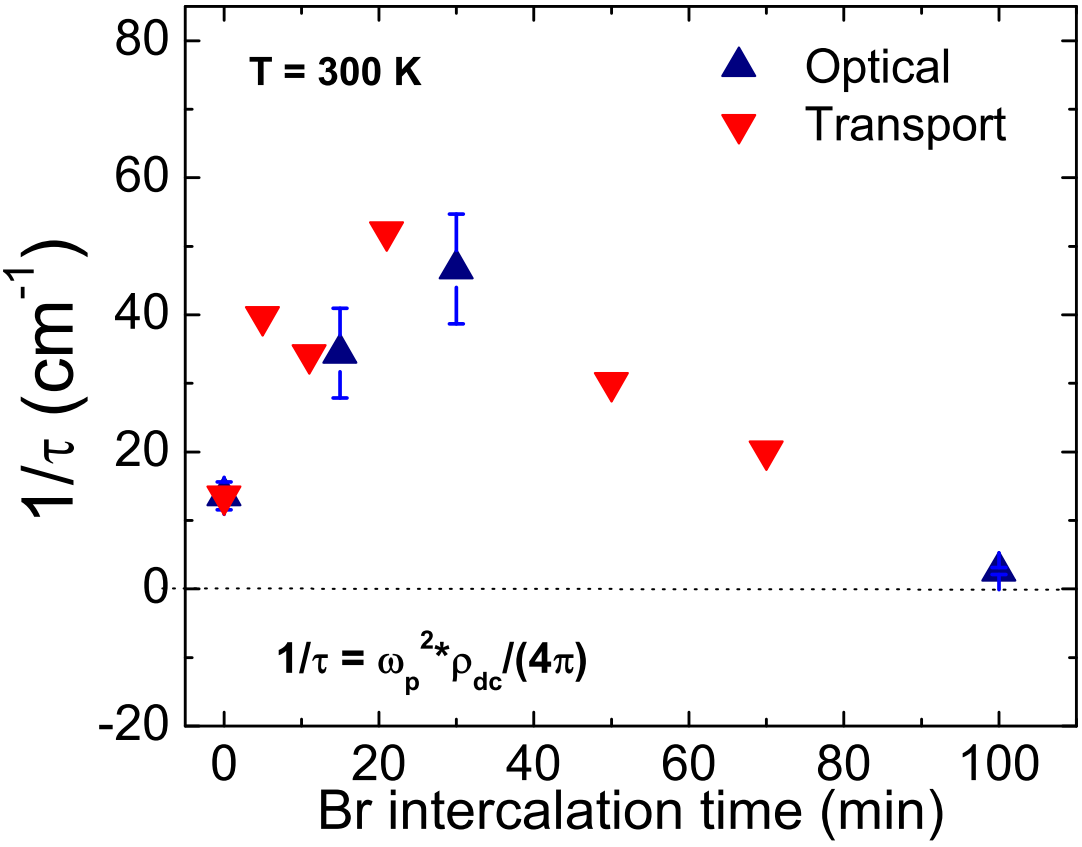

Figure 7-7. Plot of scattering rates determined from optical (blue triangles) and transport (red triangles) shows non-monotonic dependence on bromine intercalation times.

CHAPTER 8
GRAPHENE AND GRAPHITE GROWTH ON SIC BY THERMAL ANNEALING

8.1 Introduction

Graphene is a nearly ideal single layer of sp^2 bonded carbon atoms forming a honeycomb lattice. Graphene is a zero band gap semiconductor with its unique band structure properties such as massless charge carriers (Dirac fermions) with experimentally measured mobilities exceeding 100,000 $cm^2V^{-1}s^{-1}$ (100 times bigger than Si) [105]. The band structure of graphene can easily be derived from graphite's more complicated energy spectrum. The coupling parameters for graphite are identified from γ_0 up to γ_6 and their values and descriptions are given in section 5.1.2, Table 5-1. On the other all those couplings that exist in graphite goes to zero except the nearest neighbor carbon carbon coupling (in-plane carbon carbon coupling) labelled as γ_0, and the bi-layer graphite spectrum given by Eq. 5–7 reduces to $\epsilon = \pm\nu_\rho k_\rho$. Moreover, graphene is transparent in the visible range and the sp^2 nature of the bonding in between carbons makes graphene a chemically/thermally robust material. So far graphene has attracted a lot of attention after becoming experimentally accessible via mechanical exfoliation method [42]. However, various allotropes of graphene have been the center of attention for more than 5 decades as: 0D fullerenes, 1D carbon nanotubes, and 3D graphite. Recent advances in carbon nanotechnology have resulted in the controllable growth of single layer graphene on 4H-SiC, 6H-SiC, various crystalline metals and metal thin films. Such advances have resulted in a tremendous growth of both experimental and theoretical investigations that have lead to a variety of potential applications from engineering to fundamental sciences.

So far single or many layer graphene has been grown on different substrates by solid state sublimation on 4H-SiC and 6H-SiC [52], chemical vapor deposition on nickel thin foils [106] and epitaxial methods on copper thin films [107]. Even though each method has its own strengths, only graphene growth on SiC by solid

state sublimation gives the highest quality graphene. On the other hand, experimental difficulties associated with growth requirements such as UHV, local electron field effect annealing as well as sensitive growth conditions are typically too complicated for the possible industrial proposes. It has been speculated that, if SiC samples are annealed to high enough temperatures the UHV conditions might not be necessary. In this part of the dissertation, we present another new technique to grow graphite and graphene on 4H-SiC and 6H-SiC via a joule heating effect.

8.2 Experimental Details

Most of the graphene growth techniques on SiC involve annealing a very limited area on SiC under ultra high vacuum conditions (UHV) by quantum field emission of high energy electrons from a very sharp tungsten metal tip. These heaters are commercially available and heavily used in scanning electron microscopes (SEM). In this technique [52], local parts of the SiC is annealed up to high temperature for various time scales, electron energy intensity and different soaking temperatures to tune the number of graphene layers grown on SiC. In this chapter, we propose a much simpler and practical way to grow graphite (graphene) on SiC under high vacuum conditions around $10^{-6} - 10^{-7}$ Torr We anneal SiC wafers that are already in thermal contact with a tungsten boat and we pass direct current which is order of 100-200 Amp through the tungsten boat for various time, at various magnitudes, different rates and different cooling rates and soaking temperatures. Many parameters on the growth conditions allows us to tune the number of graphene layers grown on SiC easier than the previous method. The details of the growth parameters will be revealed in a separate publication.

8.3 Material Characterization

We have employed Raman spectroscopy, Auger electron spectroscopy (AES), X-ray diffraction (XRD) measurements, and electrical measurements to validate the quality of the graphite (graphene) grown by this joule heating technique on SiC.

In Fig. 8-1 the data in black data points (upper panel) correspond to the bare 4H-SiC Raman spectra while red and blue straight lines correspond to the joule annealed samples. The Raman data taken on sample given by red lines (middle panel) is annealed by passing 170 Amp for 6 min through the tungsten boat while the sample given in blue (lower panel) is annealed by passing 200 Amp for 3 min. These currents approximately corresponds to 1900 C and 2400 C for 170 A and 200 A accordingly. Comparing black, red and blue lines, shows a clear indication of new additional peaks while native SiC peaks starts to disappear. Those additional peaks are identified as D, G and 2D graphite peaks. Therefore, 200 Amp sets a high limit in the graphene growth on SiC by this method. After the treatment, the samples are typically observed to be black, shiny and conductive. 200 Amp (2400 C) heats up the sample to the high temperature under high vacuum conditions, and creates thick black and shiny graphite on the SiC surface. However, reduction of the current to 170 Amp significantly reduces the thickness to couple layers and becomes less conductive than that of graphite on the SiC. Accordingly, the Raman data taken on the 170 Amp annealed sample doesn't show clear graphite/graphene vibrational modes. Upon close look around the bare SiC sample and annealed SiC samples look slightly different with the background hidden graphite vibrational mode peaks. In Fig. 8-2 the subtraction of the bare SiC raw data from the annealed SiC (200 Amp 3 min.) from shows a clear D, G and 2D graphene Raman modes with G mode position corresponding to somewhere in between Graphite and graphene (single and/or couple layer graphene).

Even though Raman spectroscopy shows an evidence of graphene, graphite on the surface many other techniques can be performed on the sample. Electronic transport, Auger electron spectroscopy, and X-ray diffraction measurements are done on the sample. Fig. 8-3 shows the resistivity data from 300 K down to 1.7 K on 200 Amp annealed SiC (2400 C). The room temperature in-plane resistivity is measured to be around 30 $\mu\Omega$.cm at room temperature (Fig. 8-3) consistent with the pristine highly

oriented pyrolytic graphite (HOPG) sample with 15-30 $\mu\Omega$.cm in-plane resistivities. [38]. In pristine HOPG, the temperature dependence of the in-plane resistivity is metallic while the resistivity of graphite grown on SiC is insulating like and starts to saturate below 50 K. To understand the temperature dependence of the resistivity, we have further characterized samples using AES to measure concentration of the impurities and AFM to determine average grain sizes in the graphite thin film. Fig. 8-4 displays the AFM images taken on the samples. Typical films are observed to have average grain sizes of 25 nm.

Since graphite is a clean semi-metal, the at room temperature the average electron has enough energy to overcome the energy barrier (tunneling) barrier between adjacent grains and the measured resistivity corresponds to resistivity of HOPG graphite. However, as the temperature lowered, tunneling processes become more dominant and becomes temperature independent as observed in Fig. 8-3.

Overall, in this chapter we have displayed a new method to grow graphene or graphite on SiC substrates. AES, Raman spectroscopy, resistivity measurements as well as AFM images show a good quality graphite at 300K. Our current research will be mostly focused on graphene growth on 4H-SiC and 6H-SiC using the method described above, as well as carbon implantation in SiC substrates and diffusion of carbon atoms at high temperatures. Our preliminary measurements imply that lower temperature and pressure graphene growth is possible. Moreover, carbon implantation in Si, Ge, Cu and Ni thin films also show encauraging results. Experimental details, and further discussion on this topic will be published in upcoming articles and continuation dissertations.

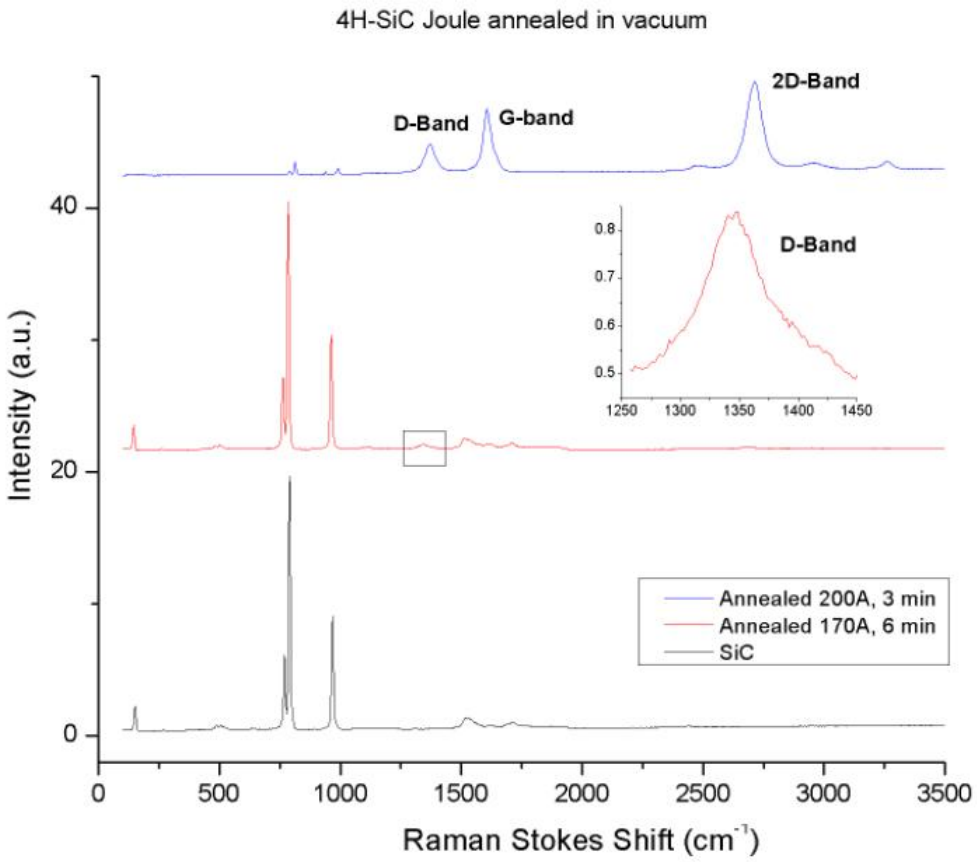

Figure 8-1. Raman spectrum taken on pristine 4H-SiC (black line) and annealed SiC by passing current through Tungsten wire (170A red line and 200A blue line).

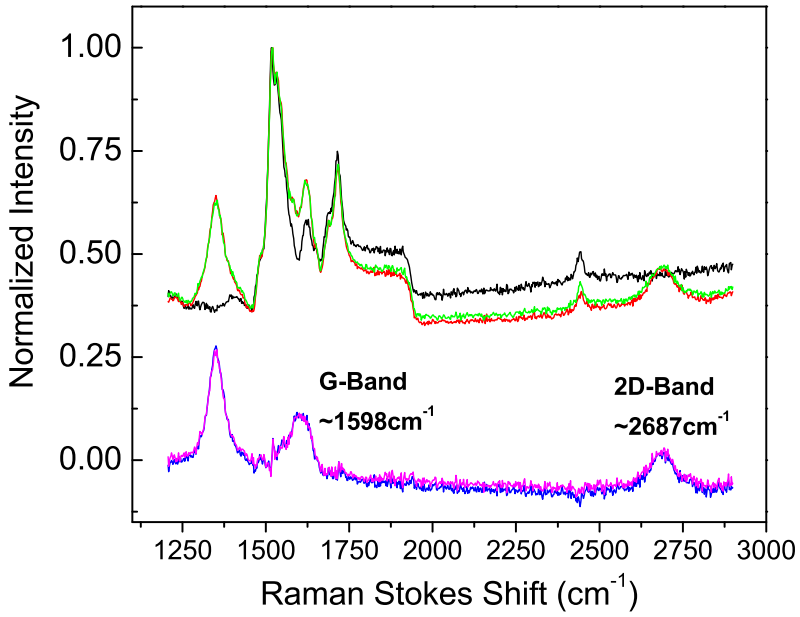

Figure 8-2. Subtraction of Raman spectrum of pristine 4H-SiC (black line) and annealed (2000C for 3 minutes) samples (red and green lines) and existance of D, G, and 2D modes (magenta and blue lines.)

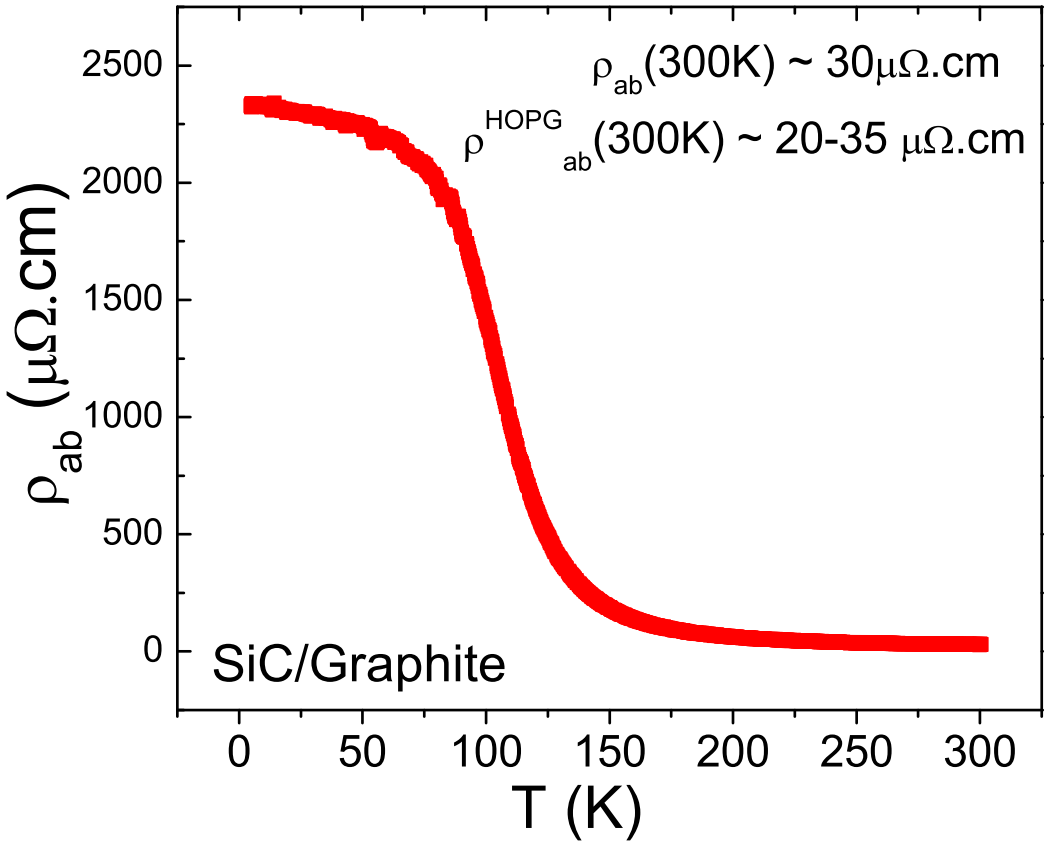

Figure 8-3. Temperature dependence of in-plane resistivity of graphite grown on SiC

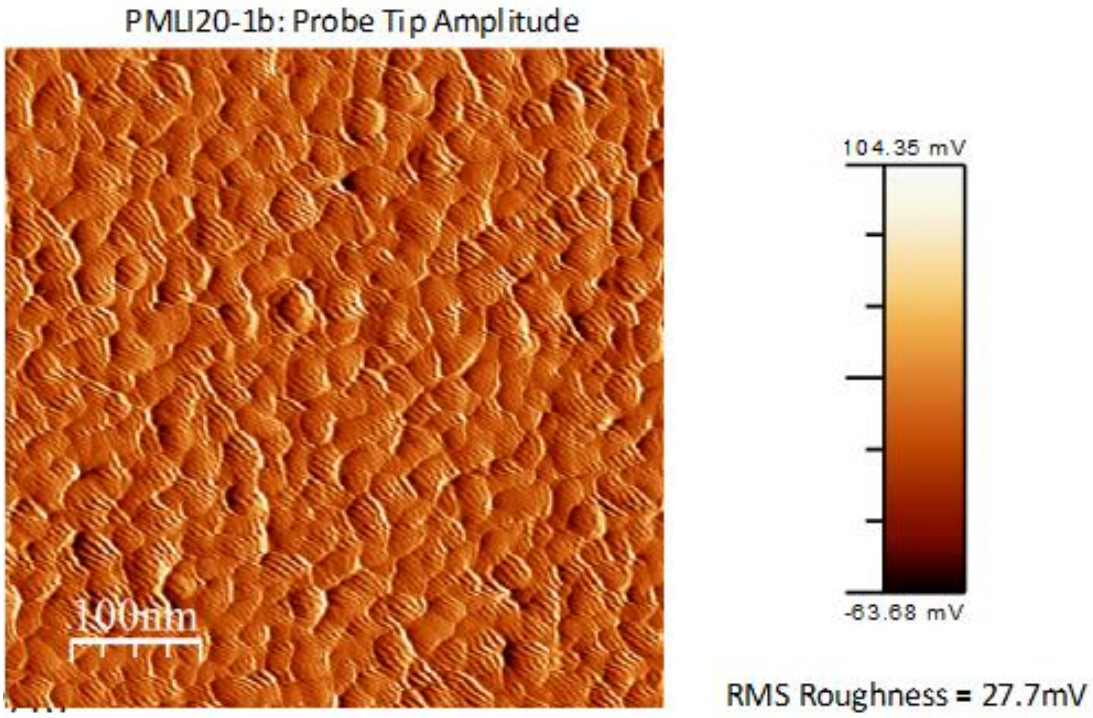

Figure 8-4. AFM image taken on graphite SiC surface

REFERENCES

[1] Tung, R. T. Recent advances in schottky barrier concepts. *Mater. Sci. Eng. R-Rep.a* **35**, 1–138 (2001).

[2] Neamen, D. A. *Semiconductor Physics and Devices, Third ed.* (Mcgraw Hill, Boston, 2003).

[3] Sze, S. M. *Physics of semiconductor devices 2nd edition* (John Wiley and Sons, New York, 1981).

[4] Padovani, F. A. & Stratton, R. Field and thermionic-field emission in schottky barriers. *Solid-State Electronics* **9**, 695 – 707 (1966).

[5] Fowler, R. The analysis of photoelectric sensitivity curves for clean metals at various temperatures. *Phys. Rev.* **38**, 45 (1931).

[6] Louie, S. G. & Cohen, M. L. Self-consistent pseudopotential calculation for a metal-semiconductor interface. *Phys. Rev. Lett.* **35**, 866–869 (1975).

[7] Tersoff, J. Schottky barrier heights and the continuum of gap states. *Physical Review Letters* **52**, 465 (1984).

[8] Fujitani, H. & Asano, S. Schottky barriers at NiSi2/Si(111) interfaces. *Physical Review B* **42**, 1696 LP (1990).

[9] Kim, D. M., Kim, D. H. & Lee, S. Y. Characterization and modeling of temperature-dependent barrier heights and ideality factors in gaas schottky diodes. *Solid-State Electronics* **51**, 865 – 869 (2007).

[10] Bauza, D. Effect of deep traps on the capacitance-voltage plots of schottky barrier diodes: Application to the study of sputter-etched Ti-W/n-Si diodes. *Journal of Applied Physics* **73**, 1858–1865 (1993).

[11] Newman, N., Schilfgaarde, M., Kendelwicz, T. & Williams, F. Electrical study of schottky barriers on atomically clean gaas(110) surfaces. *Phys. Rev. B* **33**, 1146 (1985).

[12] Kikkawa, J. M. & Awschalom, D. D. Lateral drag of spin coherence in gallium arsenide. *Nature* **397**, 139–141 (1999).

[13] Hanbicki, A. T., Jonker, B. T., Itskos, G. & Kioseoglou, G. Efficient electrical spin injection from a magnetic metal/tunnel barrier contact into a semiconductor. *Applied Physics Letters* **80**, 1240–1242 (2002).

[14] Crooker, S. A., Furis, M., Lou, X. & Adelmann, C. Imaging spin transport in lateral ferromagnet/semiconductor structures. *Science* **309**, 2191–2195 (2005).

[15] Parish, M. M. & Littlewood, P. B. Magnetocapacitance in nonmagnetic composite media. *Phys. Rev. Lett.* **101**, 166602 (2008).

[16] Zutic, I., Fabian, J. & Sarma, S. D. Spintronics: Fundamentals and applications. *Reviews of Modern Physics* **76**, 323 (2004).

[17] Yafet, Y., Keyes, R. W. & Adams, E. N. Hydrogen atom in a strong magnetic field. *Journal of Physics and Chemistry of Solids* **1**, 137 – 142 (1956).

[18] Armistead, C. J., Makado, P. C., Najda, S. P. & Stradling, R. A. Far-infrared studies at intermediate magnetic fields with the neutral shallow donors in GaAs and InP of transitions not involving the ground state. *Journal of Physics C: Solid State Physics* **19**, 6023–6037 (1986).

[19] Klarenbosch, A. V., Klaassen, T. O., Wenckebach, W. T. & Foxon, C. T. Identification and ionization energies of the shallow donor metastable states in GaAs:Si. *J. Appl. Phys.* **67**, 6323 (1990).

[20] Poehler, T. O. Magnetic freezeout and impact ionization in gaas. *Physical Review B* **4**, 1223 LP (1971).

[21] Jouault, B., Raymond, A. & Zawadzki, W. Ionization energy of magnetodonors in pure bulk gaas. *Physical Review B* **65**, 245210 (2002).

[22] Herrero, A. M., Gerger, A. M., Gila, B. P. & Pearton, S. J. Interfacial differences in enhanced schottky barrier height Au/n-GaAs diodes deposited at 77k. *Applied Surface Science* **253**, 3298 – 3302 (2007).

[23] Kwak, J. S., Kim, H. N., Baik, H. K. & Lee, J. Microstructural and electrical investigations of Pd/Ge/Ti/Au ohmic contact to n-type GaAs. *Journal of Applied Physics* **80**, 3904–3909 (1996).

[24] Lai, J. T. & Lee, J. Y. Redistribution of constituent elements in Pd/Ge contacts to n-type GaAs using rapid thermal annealing. *Journal of Applied Physics* **76**, 1686–1690 (1994).

[25] Catalan, G. Magnetocapacitance without magnetoelectric coupling. *Applied Physics Letters* **88**, 102902 (2006).

[26] Hikita, Y., Kozuka, Y., Susaki, T. & Takagi, H. Characterization of the schottky barrier in SrRuO3/Nb:SrTiO3 junctions. *Applied Physics Letters* **90**, 143507 (2007).

[27] Shklovskii, B. I. & Efros, A. L. *Electronic Properties of Doped Semiconductors* (Springer-Verlag, Berlin, 1984).

[28] Cole, K. S. & Cole, R. H. Dispersion and absorption in dielectrics i. alternating current characteristics. *The Journal of Chemical Physics* **9**, 341–351 (1941).

[29] Stanton, C. J. & Bailey, D. W. Rate equations for the study of femtosecond intervalley scattering in compound semiconductors. *Phys. Rev. B* **45**, 8369–8377 (1991).

[30] Rhoderick, E. H. & Williams, R. H. *Metal-Semiconductor Contacts, 2nd ed.* (Oxford University Press, USA, 1988).

[31] Barbolla, J., Dueas, S. & Bailn, L. Admittance spectroscopy in junctions. *Solid-State Electronics* **35**, 285 – 297 (1992).

[32] Fonash, S. J. A reevaluation of the meaning of capacitance plots for schottky-barrier-type diodes. *Journal of Applied Physics* **54**, 1966–1975 (1983).

[33] Klarenbosch, A. V., Klaassen, T. O., Wenckebach, W. T. & Foxon, C. T. Identification and ionization energies of the shallow donor metastable states in GaAs:Si. *Journal of Applied Physics* **67**, 6323–6328 (1990).

[34] Zimmerman, J. D., Brown, E. R. & Gossard, A. C. Tunable all epitaxial semimetal-semiconductor schottky diode system: ErAs on InAlGaAs. *Journal of Vacuum Science & Technology B: Microelectronics and Nanometer Structures* **23**, 1929–1935 (2005).

[35] Neto, A. D. The electronic properties of graphene. *Reviews of Modern Physics* **81**, 109 (2009).

[36] Geim, A. K. Graphene: Status and prospects. *Science* **324**, 1530–1534 (2009).

[37] Zhou, S. Y., Gweon, G. H., Graf, J. & Fedorov, A. V. First direct observation of dirac fermions in graphite. *Nature Physics* **2**, 595–599 (2006).

[38] Gutman, D. B., Tongay, S., Pal, H. K. & Maslov, D. L. Graphite in the bilayer regime: In-plane transport. *Phys. Rev. B* **80**, 045418 (2009).

[39] Hao, P. H., Wang, L. C., Deng, F. & Lau, S. S. On the low resistance Au/Ge/Pd ohmic contact to n-GaAs. *Journal of Applied Physics* **79**, 4211–4215 (1996).

[40] Han, S. Y., Shin, J. Y., Lee, B. T. & Lee, J. L. Microstructural interpretation of ni ohmic contact on n-type 4h–sic. *Journal of Vacuum Science & Technology B: Microelectronics and Nanometer Structures* **20**, 1496–1500 (2002).

[41] Wang, H. T., Jang, S., Anderson, T. & Chen, J. J. Increased schottky barrier heights for Au on n- and p-type GaN using cryogenic metal deposition. *Applied Physics Letters* **89**, 122106 (2006).

[42] Novoselov, K. S., Geim, A. K., Morozov, S. V. & Jiang, D. Electric field effect in atomically thin carbon films. *Science* **306**, 666–669 (2004).

[43] Wagner, L., Young, R. & Sugerman, A. A note on the correlation between the schottky-diode barrier height and the ideality factor as determined from I-V measurements. *Electron Device Letters, IEEE* **4**, 320–322 (1983).

[44] Han, S. Y., Kim, K. H., Kim, J. K. & Jang, H. W. Ohmic contact formation mechanism of Ni on n-type 4H-SiC. *Applied Physics Letters* **79**, 1816–1818 (2001).

[45] Wang, H. T., Jang, S., Anderson, T. & Chen, J. J. Increased schottky barrier heights for Au on n- and p-type GaN using cryogenic metal deposition. *Applied Physics Letters* **89**, 122106 (2006).

[46] Olbrich, A., Vancea, J., Kreupl, F. & Hoffmann, H. Potential pinch-off effect in inhomogeneous Au/Co/GaAs(100)-schottky contacts. *Applied Physics Letters* **70**, 2559–2561 (1997).

[47] Suzuki, S., Bower, C., Kiyokura, T. & Nath, K. G. Photoemission spectroscopy of single-walled carbon nanotube bundles. *Journal of Electron Spectroscopy and Related Phenomena* **114-116**, 225 – 228 (2001).

[48] Sque, S. J., Jones, R. & Briddon, P. R. The transfer doping of graphite and graphene. *phys. stat. sol. (a)* **204**, 3078–3084 (2007).

[49] Taft, E. & Apker, L. Photoelectric emission from polycrystalline graphite. *Phys. Rev.* **99**, 1831–1832 (1955).

[50] Dandrea, R. G. & Duke, C. B. Interfacial atomic composition and schottky barrier heights at the Al/GaAs(001) interface. vol. 11, 1553–1558 (AVS, 1993).

[51] Fujitani, H. & Asano, S. Electronic structure of si/disilicide interfaces. *Applied Surface Science* **41-42**, 164 – 168 (1989).

[52] Berger, C., Song, Z., Li, T. & Li, X. Ultrathin epitaxial graphite: 2d electron gas properties and a route toward graphene-based nanoelectronics. *J. Phys. Chem. B* **108**, 19912–19916 (2004).

[53] Gworek, C., Phatak, P., Jonker, B. T. & Weber, E. R. Pressure dependence of Cu, Ag, and Fe/n-GaAs schottky barrier heights. *Phys. Rev. B* **64**, 045322 (2001).

[54] Dresselhaus, M. S. & Dresselhaus, G. Graphite intercalation compounds. *Advances in Physics* **30**, 189 (1981).

[55] Tongay, S., Schumann, T. & Hebard, A. F. Graphite based schottky diodes formed on Si, GaAs, and 4H-SiC substrates. *Applied Physics Letters* **95**, 222103 (2009).

[56] Han, S. Y., Shin, J. Y., Lee, B. T. & Lee, J. L. Microstructural interpretation of Ni ohmic contact on n-type 4H-SiC. *Journal of Vacuum Science & Technology B: Microelectronics and Nanometer Structures* **20**, 1496–1500 (2002).

[57] Karpan, V. M., Giovannetti, G., Khomyakov, P. A. & Talanana, M. Graphite and graphene as perfect spin filters. *Phys. Rev. Lett.* **99**, 176602 (2007).

[58] Tongay, S., Hwang, J., Tanner & Pal, D. B. Ultrasuper conductivity in bromine intercalated graphite. *arXiv:0907.1111v1* **1**, 1 (2010).

[59] Rousseau, B., Szwarckopf, H. E., Thomann, A. & Brault, P. Xrs studies of graphite and intercalated graphite. *Appl. Phys. A, Material Sci. and Proc.* **77**, 591–597 (2003).

[60] Wertheim, G. K., Van Attekum, P. T. T. M. & Basu, S. Electronic structure of lithium graphite. *Solid State Communications* **33**, 1127 – 1130 (1980).

[61] Zhang, Y., Zhang, Z., Li, T., Liu, X. & Xu, B. Xps and xrd study of FeCl3-graphite intercalation compounds prepared by arc discharge in aqueous solution. *Spectrochimica Acta Part A: Molecular and Biomolecular Spectroscopy* **70**, 1060 – 1064 (2008).

[62] Brandt, N. B., Chudinov, S. M. & Ponomarev, Y. G. *Semimetals I Graphite and Its Compounds* (North-Holland, Amsterdam, 1988).

[63] Hussey, N. E., Mackenzie, A. P., Cooper, J. R. & Maeno, Y. Normal-state magnetoresistance of Sr2RuO4. *Phys. Rev. B* **57**, 5505–5511 (1998).

[64] Annett, J. F., Goldenfeld, N. & Renn, S. R. *Physical Properties of High Temperature Superconductors II* (World Scientific, Singapore, 1990).

[65] Kroto, H. W., Heath, J. R., O'Brien, S. C. & Curl, R. F. C60: Buckminsterfullerene. *Nature* **318**, 162–163 (1985).

[66] Radushkevich, L. & Lukyanovich, V. Tubule carbons. *Zurn. Fisc. Chim (Journal of Physical Chemistry of Russia)* **26**, 88 (1952).

[67] Oberlin, A., Endo, M. & Koyama, T. Filamentous growth of carbon through benzene decomposition. *Journal of Crystal Growth* **32**, 335 – 349 (1976).

[68] Iijima, S. Helical microtubules of graphitic carbon. *Nature* **354**, 56–58 (1991).

[69] Cervenka, J., Katsnelson, M. I. & Flipse, C. F. J. Room-temperature ferromagnetism in graphite driven by two-dimensional networks of point defects. *Nat Phys* **5**, 840–844 (2009).

[70] Esquinazi, P., Setzer, A., Hohne, R. & Semmelhack, C. Ferromagnetism in oriented graphite samples. *Phys. Rev. B* **66**, 024429 (2002).

[71] Kempa, H., Esquinazi, P. & Kopelevich, Y. Integer quantum hall effect in graphite. *Solid State Communications* **138**, 118 – 122 (2006).

[72] Esquinazi, P., Garcia, N., Barzoil, J. & Rodiger, P. Indications for intrinsic superconductivity in highly oriented pyrolytic graphite. *Phys. Rev. B* **78**, 134516 (2008).

[73] Du, X., Tsai, S., Maslov, D. L. & Hebard, A. F. Metal-insulator-like behavior in semimetallic bismuth and graphite. *Phys. Rev. Lett.* **94**, 166601 (2005).

[74] Kopelevich, Y., Pantoja, J. C., da Silva, R. R. & Moehlecke, S. Universal magnetic-field-driven metal-insulator-metal transformations in graphite and bismuth. *Phys. Rev. B* **73**, 165128 (2006).

[75] Ebbesen, T. W. *Carbon nanotubes: preparation and properties* (CRC Press, INC, 1997).

[76] Slonczewski, J. C. & Weiss, P. R. Band structure of graphite. *Phys. Rev.* **109**, 272 (1958).

[77] McClure, J. W. Band structure of graphite and de Haas-van Alphen effect. *Phys. Rev.* **108**, 612 (1957).

[78] Sharma, M. P., Johnson, L. G. & McClure, J. W. Diamagnetism of graphite. *Physics Letters A* **44**, 445 – 446 (1973).

[79] Ushio, H., Uda, T. & Uemura, Y. Theory of cyclotron resonance of graphite. i. determination of the degree of band warping. *Journal of the Physical Society of Japan* **33 (6)**, 1551–1560 (1972).

[80] Wallace, P. R. The band theory of graphite. *Phys. Rev.* **71**, 622 (1947).

[81] McCann, E. & Falko, V. I. Landau-level degeneracy and quantum hall effect in a graphite bilayer. *Phys. Rev. Lett.* **96**, 086805 (2006).

[82] Nilsson, J., Neto, A. H. C., Peres, N. M. R. & Guinea, F. Electron-electron interactions and the phase diagram of a graphene bilayer. *Phys. Rev. B* **73**, 214418 (2006).

[83] Wirtz, L. & Rubio, A. The phonon dispersion of graphite revisited. *Solid State Comm.* **131**, 141 (2004).

[84] Gonzalez, J., Guinea, F. & Vozmediano, M. A. Marginal-fermi-liquid behavior from two-dimensional coulomb interaction. *Phys. Rev. B (Rapid Comm.)* **59**, 2474 (1999).

[85] Maultzsch, J., Reich, S., Thomsen, C. & Requardt, H. Phonon dispersion in graphite. *Phys. Rev. Lett.* **92**, 075501 (2004).

[86] Ono, S. C-axis resistivity of graphite in connection with stacking faults. *J. Phys. Soc. Jpn.* **40**, 498 (1976).

[87] Uher, C., Hockey, R. L. & Ben, E. J. Pressure dependence of the c-axis resistivity of graphite. *Phys. Rev. B* **35**, 44834488 (1986).

[88] Ioffe, L. B., Larkin, A. I., Varlamov, A. A. & Yu, L. Effect of superconducting fluctuations on the transverse resistance of high-tc superconductors. *Phys. Rev. B* **47**, 8936 (1993).

[89] Moses, P. & McKenzie, R. H. Comparison of coherent and weakly incoherent transport models for the interlayer magnetoresistance of layered fermi liquids. *Phys. Rev. B* **60**, 7998 (1999).

[90] Matsubara, K., Sugihara, K. & Tsuzuku, S. Electrical resistance in the c direction of graphite. *Phys. Rev. B* **41**, 969 (1989).

[91] Xu, Y., Ephron, D. & Beasley, M. R. Directed inelastic hopping of electrons through metal-insulator-metal tunnel junctions. *Phys. Rev. B* **52**, 2843 (1995).

[92] Simmons, J. G. Generalized thermal J-V characteristic for the electric tunnel effect. *J. Appl. Phys.* **35,**, 2655 (1964).

[93] Zhou, S. Y., Gweon, G. H., Graf, J. & Fedorov, A. V. First direct observation of dirac fermions in graphite. *Nature Physics* **595**, 2006 (2).

[94] Schedin, F., Geim, A. K., Morozov, S. V. & Hill, E. W. Detection of individual gas molecules adsorbed on graphene. *Nature Materials* **6**, 652 (2007).

[95] Foley, G. M. T., Zeller, C., Falardeau, E. R. & Vogel, F. L. Metallic reflectance of AsF5-graphite intercalation compounds. *Solid State Communications* **24**, 371 (1977).

[96] Yan, Z., Zhuxia, Z., Tianbao, L. & Xuguanga, L. Xps and xrd study of FeCl3graphite intercalation compounds prepared by arc discharge in aqueous solution. *Spectrochimica Acta Part A* **70**, 1060 (2008).

[97] Pal, H. K. & Maslov, D. L. (unpublished) (2010).

[98] Wooten, F. *Optical Properties of Solids* (Academic Press, San Diego, 1972).

[99] Leung, S. Y., Underhill, C., Dresselhaus, G. & Dresselhaus, M. S. Infrared active lattice modes in graphite alkali metal compounds. *Solid State Commun.* **33**, 285 (1980).

[100] Dresselhaus, M. S., Dresselhaus, D. & Fischer, J. E. Graphite intercalation compounds: Electronic properties in the dilute limit. *Phys. Rev. B* **15**, 3180 (1977).

[101] Gutman, D., Tongay, S., Pal, H. K. & Maslov, D. L. Graphite in the bilayer regime: In-plane transport. *Phys. Rev. B* **80**, 045418 (2009).

[102] Venghaus, H. Infrared reflectance and dielectric properties of pyrolytic graphite for e par c polarization. *Phys. Status Solidi* **81**, 221 (1977).

[103] Shklovskii, B. I. (private communication) .

[104] Chui, S. T. & Esfarjani, S. T. Finite-temperature two-dimensional wigner transition. *Phys. Rev. B* **44**, 11498 (1991).

[105] Du, X., Skachko, I., Barker, A. & Andrei, E. Y. Approaching ballistic transport in suspended graphene. *Nature Nanotechnology* **3**, 491 (2008).

[106] Yu, Q. Graphene segregated on Ni surfaces and transferred to insulators. *Appl. Phys. Lett.* **93**, 113103 (2008).

[107] Li, X., Cai, W., An, J. & Kim, S. Large-area synthesis of high-quality and uniform graphene films on copper foils. *Science* **324**, 1312 (2009).

BIOGRAPHICAL SKETCH

Sefaattin Tongay was born in Berlin, Germany in 1980. He has spent dreamy childhood years with his parents Suzan Tongay and Ergun Tongay and his 4 sisters and 1 brother. He started his education in Germany and went to secondary and high school in the most western point of Turkey, Izmir. He has started his college degree in Ege University, Department of Physics, theoretical physics division in 1998 and graduated in 2002 with Summa Cum Laude honors ranking first in class of 2002. During his undergraduate studies, he specialized on molecular dynamics and ab-initio calculations under Prof. Dr. Emine Cebe's supervision. After bachelor's degree, he decided to work in theoretical condensed matter physics at Bilkent University in Turkey with Prof. Dr. Salim Ciraci. During Master of Science studies, he has worked on carbon based systems using ab-initio, molecular dynamics, and first principle calculations as an approach. He has been awarded with Master of Science and he has written his Master of Science thesis on Carbon and Silicon based nanowires. His major finding in his master's degree includes prediction (and studying its physical properties) of carbon linear chains as stable carbon allotrope which has been experimentally synthesized for the first time by Japaneese physicist S. Iijima in 2009.

Starting from 2005, he has started working in University of Florida, Department of Physics as a research assistant in Prof. Dr. A. F. Hebard's laboratory. He has been deeply innovated and inspired by Prof. Dr. A. F. Hebard during his stay in Florida and he has focused on semiconductors, diluted magnetic semiconductors, carbon based systems (graphite, graphene, CNTs and C60s), and complex oxides. His work in Doctor of Philosophy studies includes the discovery of supermetallicity in bromine intercalated graphite, formation of diodes at the multi-layer-graphene (or graphene) / various semiconductor junctions and sensor, diode, high temperature and high frequency applications, magnetocapacitance effect in metal / semiconductor junctions and transition from graphite to bi-layer graphene at high temperatures. He has been

awarded the prestigious Tom Scott award in December 2009, and he is currently the author of 13 refereed journals with h-index of 8 and one provisional patent titled 'integration of carbon based structures in semiconductor technology'.